UNIVERSITY OF CALIFORNIA,
IRVINE

Metasurfaces and Zero-Index Photonics in Optical Fibers

DISSERTATION

submitted in partial satisfaction of the requirements
for the degree of

DOCTOR OF PHILOSOPHY

in Physics

by

Jingyi Yang

Dissertation Committee:
Associate Professor Howard Lee, Chair
Professor Christopher P.J. Barty
Associate Professor Franklin J. Dollar
Assistant Professor Luis A. Jauregui

2021

Dedication

To

my parents Li Zhou, Yongjie Yang

in recognition of their unconditional love and support.

...wherever they might be they always remember that the past was a lie,
that memory has no return,
that every spring gone by could never be recovered,
and that the wildest and most tenacious love was an ephemeral truth in the end.

Gabriel García Márquez
One Hundred Years of Solitude

and

What matters in life is not what happens to you
but what you remember and how you remember it.

Gabriel García Márquez
Living to Tell the Tale

Contents

Page

List of Figures

List of Tables

Acknowledgements

I would like to express my appreciation to my advisor Prof. Howard Lee for his continuous support and mentorship during my PhD study from Baylor University to University of California, Irvine. Without his guidance and patience, this dissertation would not have been possible. I remembered vividly when the first time I presented my work at 2018 OSA (now Optica) Frontier in Optics conference, Howard spent a huge amount of time with me on my practice for every statement and each transition between the slides. I wouldn't get my first best presentation award without his help. It has been a privilege to work for him and I will always be grateful for all that he taught me in the past six years. I would also like to thank my dissertation committee members, Prof. Chris Barty, Prof. Franklin Dollar and Prof. Luis Jauregui, and candidacy committee member Prof. Eric Potma for their invaluable suggestions.

A special "thank-you" goes to Prof. Zhenrong Zhang and Prof. Gregory Benesh at Baylor University. I started my transition journey from an engineering student to a PhD student in Physics at Baylor by taking Quantum Mechanics and E&M class with them. They kindly helped me fill in course gaps in office hours at the very first semester so that I made all the qualification exams on the first attempt in my second year.

I have had the fortune of working with many gifted colleagues and collaborators. I would like to thank Dr. Khant Minn, who used to work together with me in nanofabrication and measurement. Thanks also go to Dr. Aleksei Anopchenko, Sudip Gurung and many more colleagues and alumni in Howard's group. Alongside colleagues, a huge "thank you" goes to our fabulous collaborators, Prof. Pin Chieh Wu and Prof. Din Pin Tsai. I would like to acknowledge the support of Dr. Bernd Zechmann from the Center for Microscopy and Imaging as well as the High Performance and Research Computing Services at Baylor University.

Outside the lab and campus, I have benefited from the support of scholarships and travel grants from photonic communities, SPIE, Optica (formerly OSA), IEEE Photonic Society and APS. While traveling for research, I feel lucky to have conversations with so many fantastic individuals, Dr. Linhui Yu, Dr. Katie E. Chong, Dr. Dongyu Chen, Prof. Wen-Hui Cheng, Prof. Andrea Armani and many more others, who made me feel supported in the community.

Last but most important, this dissertation would not exist without the unwavering love of my parents. I hope there is a word more than "thank you" to my mom and dad, who sacrificed so much to support me unconditionally to pursue my personal dreams. I am also so grateful to my extended family members who take care of my parents when I am far away from home. This thesis is dedicated to my family.

Jingyi Yang
October 2021

Vita

Education

2021 **Doctor of Philosophy, Physics** GPA:4/4
University of California, Irvine, CA USA

2017 **Master of Arts, Physics** GPA: 3.78/4
Baylor University, TX USA

2015 **Master of Science, Optical Engineering** GPA: 3.82/4
China Jiliang University, China
Advisor: Prof. Xinyong Dong

2013 **Bachelor of Engineering, Optical and Electric Engineering** GPA: 3.93/4
China Jiliang University, China

Honors & Awards

2021 **IEEE Photonics Society graduate student scholarship**

2021 **Optica Corning Women in optical communications scholarship**

2020 Best Student Presentation Award (Symposium F. NM02) at 2020 MRS Spring/Fall Meeting

2020 Best student paper award at Photonics Global Student Conference

2019 **SPIE laser technology, engineering, and applications scholarship**

2018 **Optica Emil Wolf outstanding student paper award**

2018 Cy Lynch graduate physics scholarship at Baylor University

2017 Shim C. Park and Theresa Park memorial physics scholarship at Baylor University

Journal Publications

(1) **J. Yang**, I. Ghimire, P. C. Wu, S. Gurung, C. Arndt, A. D. P. Tsai, H. W. Lee, "Photonic crystal fiber metalens", ***Nanophotonics*** 8(3), pp. 443-449 (2019) [link].

(2) **J. Yang**, K. Minn, A. Anopchenko, S. Gurung, H. W. Lee, "Coupling to epsilon-near-zero mode on ultrathin atomic layer deposited conducting oxide film in optical fiber", Submitted (2021).

(3) **J. Yang**, S. Gurung, S. Bej, PN Ni, H. W. Lee, "Active Optical Metasurfaces," ***Reports on Progress in Physics***, In press (2021) (Invited review).

(4) Q. Huang, I. Ghimire, **J. Yang**, N. Fleer, K. S. Chiang, Y. Wang, S. Banerjee, H. W. Lee, "Optical modulation in hybrid anti-resonant hollow-core fiber infiltrated with vanadium dioxide phase change nanocrystals", ***Optics Letter***, 45 (15), pp. 4240-4230 (2020). [link]

(5) J. Zhang, **J. Yang**, M. Shell, A. Anopchenko, L. Tao, Z. Yu, H. W. Lee, "Gate-tunable optical filter based on conducting oxide metasurface heterostructure", ***Optics Letters*** 44 (15), pp. 3653-3656 (2019) [link].

(6) K. Minn, A. Anopchenko, **J. Yang**, H. W. Lee, "Excitation of epsilon-near-zero resonance in ultra-thin indium tin oxide shell embedded nanostructured optical fiber", ***Scientific Reports***, 8 (1) pp. 2342 (2018) [link].

(7) L. Lei, S. Xu, **J. Yang**, H. W. Lee, "Power-dependent optical property of Yb/Er: NaGdF4@Yb: NaGdF4@Yb: NaNdF4 nanocrystals", ***Nano*** 12 (7), pp. 1750086 (2017) [link].

Conference Presentations

(1) **J. Yang** *et al*, "Dynamic manipulation of hybridized epsilon-near-zero resonances in optical fiber", *Material Research Society Fall Meeting*, Boston, MA, USA (*Dec. 2020*) (Oral).
(2) **J. Yang** *et al*, "Epsilon-near-zero mode in optical fiber", *Photonics Global Student Conference with Optoelectronics Global Conference*, Shenzhen, China (*Sep. 2020*) (Oral) (Invited).
(3) **J. Yang** *et al*, "Excitation of epsilon-near-zero mode in optical fiber coated with ultrathin Aluminum-doped zinc oxide film", *Material Research Society Fall Meeting*, Boston, MA, USA (*Dec. 2019*) (Oral).
(4) **J. Yang**, *et al*, "Excitation of epsilon-near-zero mode in optical fiber", *The Annual Conference of the IEEE Photonics Society*, San Antonio, TX, USA (*Sep. 2019*) (Oral).
(5) **J. Yang**, *et al* "Epsilon-near-zero and metasurface optics in extreme optical fiber platforms", *International Conference on Metamaterials, Photonic Crystals and Plasmonics (META 2019)*, (*Jun. 2019*) (Oral) (Invited).
(6) **J. Yang**, *et al*, "Excitation of epsilon-near-zero resonance in aluminum-doped zinc oxide nano-coated D-shaped optical fiber", *Photonics West (OPTO)*, San Francisco, CA, USA (*Feb. 2019*) (Oral).
(7) **J. Yang**, *et al*, "Metasurface and Epsilon-near-zero optics in optical fiber platform", *the 49th Winter Colloquium on the Physics of Quantum Electronics (PQE 2019)*, Snowbird, UT, USA (*Jan. 2019*) (Oral) (Invited).
(8) **J. Yang**, *et al*, "Photonic crystal fiber metalens enabled by geometric phase optical metasurfaces", *Material Research Society Fall Meeting*, Boston, MA, USA (*Nov. 2018*) (Oral).
(9) **J. Yang**, *et al*," Epsilon-near-zero resonance excitation in AZO nano-coated optical fiber waveguide", *Joint Fall 2018 Meeting of the Texas Sections of APS, AAPT, and Zone 13 of the SPS*, *Bulletin of the American Physical Society,* Houston, TX, USA (*Oct. 2018*) (Oral).
(10) **J. Yang**, *et al*, "Photonic crystal fiber metalens enabled by geometric phase optical metasurfaces", *Frontiers in Optics*, Washington DC, USA (*Sep. 2018*) (Oral).
(11) **J. Yang**, *et al*, "Photonic crystal fiber metalens", *Gordon Research Conference, Harvesting, Generating and Manipulating Light at the Nanoscale*, ME, USA (*Jul. 2018*) (Poster).
(12) **J. Yang**, *et al*, "Traction force detection on aligned smooth muscle cell sheet with optical Sagnac fiber loop", *Joint Spring 2016 Meeting of the Texas Sections of APS, AAPT, and Zone 13 of the SPS*, Abstract: F3.00006 (*2016*) (Oral).

Contributed Conference Presentations

(1) S. Gurung, **J. Yang**, A. Anopchenko, S. Bej, K. Minn, H. W. Lee, "Epsilon-near-zero optics in planar and optical fiber platform", *50th Winter Colloquium on the Physics of Quantum Electronics (PQE 2020)*, UT, USA (*Jan. 2020*) (Invited).
(2) **J. Yang**, *et al*, "Plasmonic- and meta- photonic crystal fiber for advanced optical sensing", *Photonics West, (BIOS)*, San Francisco, CA, USA (*Feb. 2019*) (Invited).
(3) **J. Yang**, *et al*," Epsilon-near-zero and metasurface optics in extreme optical fiber platforms", *Photonics West (OPTO)*, San Francisco, CA, USA (*Feb. 2019*) (Invited).

(4) A. Anopchenko, S. Bej, S. Gurung, **J. Yang**, L. Tao, C. Arndt, H. W. Lee, "Tunable conducting oxide epsilon-near-zero meta-devices", *Photonics West (OPTO)*, San Francisco, CA, USA (*Feb. 2019*) (Invited).
(5) A. Anopchenko, L. Tao, S. Gurung, **J. Yang**, S. Bej, C. Arndt, and H. W. Lee, "Tunable conducting oxide epsilon-near-zero meta-devices", *13th Conference on Lasers and Electro-Optics Pacific Rim (CLEO-PR 2018)*, Hongkong, China (*Aug. 2018*) (Invited tutorial).
(6) A. Anopchenko, L. Tao, S. Gurung, **J. Yang**, S. Bej, C. Arndt, and H. W. Lee, "Electrically-tunable zero index nanophotonics", *11th International Conference on Nanophotonics (ICNP 2018)*, Wroclaw, Switzerland, (*Jul. 2018*) (Invited).
(7) A. Anopchenko, L. Tao, S. Gurung, **J. Yang**, S. Bej, C. Arndt, K. Minn, and H. W. Lee, "Gate-tunable epsilon-near-zero nanophotonics", *OSA Optics and Photonics Congresses: Advanced Photonics, Novel Optical Materials and Application Topical Meeting (NOMA)*, Zurich, Switzerland, (*Aug.2018*) (Invited).
(8) **J. Yang**, *et al*, "Tunable zero-index and metasurface optics in extreme optical platforms", *International Conference on Metamaterials, Photonic Crystals and Plasmonics (META 2018)*, Paris, France (*Jun. 2018*) (Invited).
(9) Ghimire, S. Gurung, S. K. Mishra, **J. Yang**, and H. W. Lee, "In-fiber polarization dependent meta-color filter," *Joint Fall 2017 Meeting of the Texas Section of the APS, Texas Section of the AAPT, and Zone 13 of the Society of Physics Students*, Dallas, TX, USA (*Oct. 2017*) (Oral).
(10) H. W. Lee, **J. Yang**, L. Lei, "Upconversion nanocrystals in nanostructured optical fibers," *Progress in Electro-magnetic Research Symposium (PERS 2016)*, Shanghai, China (*Aug. 2016*) (Invited).

Patents

(1) H. W. Lee, **J. Yang**, I. Ghimire, "Metasurface on optical fiber and related method" (US Patent App. 16/443, 941, 2019).
(2) H. W. Lee, K. Minn, **J. Yang**, A. Anopchenko "Epsilon-near-zero materials integrated optical fiber devices" (Patent, pending, 2018).

Synergistic Activities & Volunteering

Jan. 2021-presenst	**SPIE Early Career and Students Subcommittee Member** ○ Review and analyze students' and early career members' feedback regarding SPIE to ensure member engagement and satisfaction
Dec. 2020-presenst	**SPIE Career Lab Editorial Board Member** ○ Invite discussion host and lead discussions on exchanging professional advice, questions, and opportunities weekly in Facebook SPIE group
Sep. 2020-present	**Optica Fiber Modeling and Fabrication Technical Group Social Media Officer**
Feb. 2020	Organized and led educational activities focused on optics at STEM Night at South Bosque Elementary School in Waco for 400+ students
Feb. 2020	**Social Media Volunteer of SPIE Photonic West Conference**
Dec. 2019	**Session chair of Material Research Society Fall Meeting**
Dec. 2019	**Symposium assistant of Material Research Society 2019 Fall Meeting**
May. 2019	Organized and led educational activities for International Day of Light

celebrations at Mayborn Museum for 200+ kids and their parents

Nov. 2018 **Guest blogger of Material Research Society Fall Meeting**

Apr. 2018 **Volunteer training & optical demonstration at Mayborn Museum, TX**

Mar. 2018
- Performed optics demonstrations and presentations at Baylor Physics Bowl competition for 40+ high school students

Sep. 2017- Dec. 2018 **Founder and President of Baylor SPIE Student Chapter**
- Initiated student chapter at Baylor University and recruited founding members
- Initiated and developed a collaborative outreach program for student chapter
- Wrote annual activities proposals for student chapter funded by SPIE
- Organized outreach activities for K-12 to promote student development, optics engagement and effective presentation of science

Travel Grants & Funding

Feb. 2020 SPIE Social Media Volunteer Travel Grant

Dec. 2019 Student Travel Grant for Material Research Society 2019 Fall Meeting

Nov. 2018 Student Travel Award for Joint Fall Meeting of the Texas Sections of APS

Jul. 2018 Optica Frontiers in Optics Officer Travel Grant

Jan. 2018 SPIE Officer Travel Grant

Aug. 2017 Baylor University SPIE Student Chapter Outreach Activity Funding fund

Apr. 2016 Student Travel Award for Joint Spring 2016 Meeting of the Texas Sections of APS

Teaching/Mentoring Experience

- Mentored following undergraduate students in summer research and scholarly achievement program
  Garand Tyson, Baylor University, May 2018–Sep 2018
  Jack Causey, Baylor University, May 2017–Sep 2017
  Jesse Watters, Baylor University, Jun. 2016–Sep. 2016
  Leon Zhang, University of California, Irvine, Oct. 2020-present
- Teaching assistant for general physics experiments, Aug. 2016-May. 2017
  - Delivered weekly tutorial and led undergraduate lab sessions.
  - Reviewed and assessed weekly lab reports from 120 students in science and engineering majors

Abstract of the Dissertation

Metasurfaces and Zero-Index Photonics in Optical Fibers
by
Jingyi Yang
Doctor of Philosophy in Physics
University of California, Irvine, 2021
Associate Professor Howard Lee, Chair

Optical fibers play a significant role in various practical applications from long-distance optical communication to fiber lasers. However, the fundamental challenges of optical fiber are that the properties of light being guided in the fiber is largely limited by the glass materials of the core and cladding, as well as by the guiding mechanism. In addition, the optical properties of the optical fibers are fixed after the fabrication process. These fundamental limitations significantly restrict further advancement of optical fiber applications. On the other hand, novel nanophotonic concepts, such as metasurfaces and zero-index photonics, provide new pathways for advanced functionalities and tunability. Metasurfaces are arrays of light resonator at subwavelength scale with designed size, shape, and orientation that induce abrupt changes of light. Zero-index materials are materials with vanishing permittivity possessing properties of strong light confinement, which enable efficient light manipulation at nanoscale. In this dissertation, I intend to integrate optical metasurfaces and zero-index photonics with optical fibers to develop a unique optical meta-fiber platform that not only allows guiding light in the long distance, but also manipulating it in the nanoscale.

My dissertation demonstrates the feasibility of the meta-fiber platform in three sections, two of them on metasurface integration and one on zero-index-material integration. The first section demonstrates the focusing of the outgoing light from an

optical fiber without an external lens, where I develop an ultrathin optical metalens directly patterned on the facet of a large mode area photonic crystal optical fiber operating at 1500-1630 μm. We experimentally characterized the performance of the fabricated metalens such as focal length (28 μm and 40 μm), full width at half maximum (2.40 μm and 3.65 μm) and operating efficiency (~16%). The second section is a proof-of-concept demonstration of fiber-integrated active metasurfaces, where I investigate a gate-tunable plasmonic color filter incorporating a metasurface heterostructure. The tunable metasurface is embedded with thin and active transparent conducting oxide layer to form a double metal-oxide-semiconductor configuration. The last section is the first experimental demonstration of nano-scale light guiding by an epsilon-near-zero (ENZ) hybrid fiber. The highly confined ENZ mode is excited internally on a side-polished optical fiber with controllable propagation (light-matter interaction) length. We also show the proof-of-concept tunability of the hybrid resonance by the external refractive index or the large nonlinearity of the ENZ thin-film. Our results indicate the accessibility of novel in-fiber devices with extended functionalities and potential applications for optical imaging, sensing, and communication technologies.

Chapter 1 Introduction

Optical fiber is a cylindrical waveguide platform that guides and transmits light into the doped core glass with high refractive index which is also coated with a pure glass cladding using the principle of total internal reflection (Figure 1-1a). The benefits of optical fibers are high transmission, low attenuation, and flexibility so that it has been broadly utilized in long-distance communication for high-speed internet [*1*], fiber lasers [*2, 3*], remote and distributed optical fiber sensing [*4*], fiber imaging [*5*] and endoscope [*6*], and fiber laser surgery [*7, 8*]. *etc.* However, due to the geometric configuration and dielectric materials of the optical fiber, the intrinsic properties of the transmitted light, such as amplitude, phase, and mode profile of light, are fixed after fiber drawing fabrication. Conventional optical fiber components modify the diffraction, reflection and refraction of light and wavefront shaping is realized through the propagation of given refractive media. In this way, the realization of optical components, such as fiber lens, holograms, and waveplates, relies on the substantial changes of electromagnetic wave and the gradual accumulation of optical paths in the media; thus, they are relatively bulky compared to the size of fiber itself (typically with cladding diameter of 125 μm). Therefore, one of the major challenges for developing advanced and miniature optical fiber devices is to shirk down the volumetric size of functional components to submicron scale. The emergence of metasurfaces and zero-index material among the expanding field of nanophotonics shows the promise to control light properties in a unique way and provide a wide range of novel optical properties. The scope of this thesis is to study the enhanced light-matter interaction by integrating metasurfaces or zero-index photonics

with optical fibers and to realize novel miniature optical fiber components and active photonic devices.

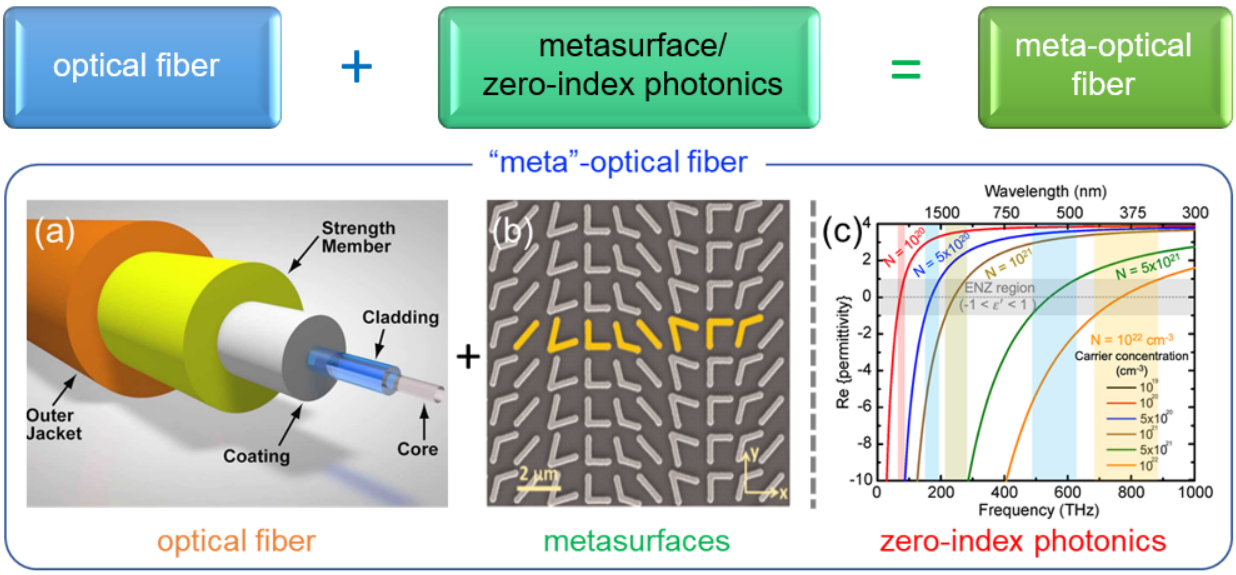

Figure 1-1 The objective of this thesis is to study the compact and enhanced light-matter interaction by integrating metasurfaces or zero-index photonics with optical fibers to realize novel miniature in-fiber components and active photonic devices.

1.1 Flat optics: metasurfaces

Metasurfaces are arrays of light scatterers (*i.e.,* resonator or antennas) at subwavelength scale with designed size, shape, and orientation that induce abrupt changes of light (Figure 1-1b) [*9*]. Each unit cell is deterministically configured to control the amplitude, phase, and polarization of the transmitted, reflected, and diffracted light [*10-12*]. These metasurfaces can be employed for various applications such as beam steering, focusing, optical switching, and for complex scattering formation (*e.g.,* holography) [*10*]. Due to the flat nature of metasurfaces (typical thickness less than 100 nm), they could enable ultrathin optical components on planar substrates such as flat lenses [*13-15*], wave plates [*16*], holographic

surfaces [*17-22*], and compact devices for the manipulation and detection of orbital angular momentum [*23-27*] over a broad range of the electromagnetic spectrum.

1.2 Zero-index photonics

Extreme light-matter interaction and light manipulation in subwavelength scales have also been observed recently in zero refractive index materials (Figure 1-1c) [*28, 29*]. Due to the unique electromagnetic properties in the zero-index medium with a vanishing real part of permittivity (epsilon-near-zero) (*e.g.,* large phase velocity and small group velocity, *etc*.), a variety of extreme optical phenomena have been exploited on planar zero-index substrates, including electromagnetic wave tunneling [*30*], strong light absorption [*31, 32*], magneto-optical isolation [*33*], enhanced quantum emission and directive emission [*34, 35*] and optical nonlinearity [*36-38*], *etc*. However, while zero-index photonics show promise for extreme light manipulation and have been extensively investigated in recent years, most of the studies of ENZ materials have been restricted to planar structures with a relatively short light-matter interaction length and complex excitation scheme. This limits the capabilities of the excitation platform and consequently the development of compact and novel optical devices with integrated advanced functionalities.

1.3 Scope of this thesis

The objective is to study the compact and enhanced light-matter interaction and manipulation of metasurfaces and zero-index materials on optical fiber platforms (Figure 1-1). By judicious integration of metasurfaces and zero-index materials with optical fibers, these designs can serve as a lens, filter, or modulator for miniature optical fiber devices and active photonic components. This thesis describes both the theoretical framework and the

proof-of-concept of such applications (Figure 1-2).

Chapter 2 outlines the relevant fundamental properties of optical fibers and theoretical description of metasurfaces and zero-index photonics. It includes the basic properties of optical fiber, the physics insight and design of metasurfaces and zero-index photonics on optical fibers.

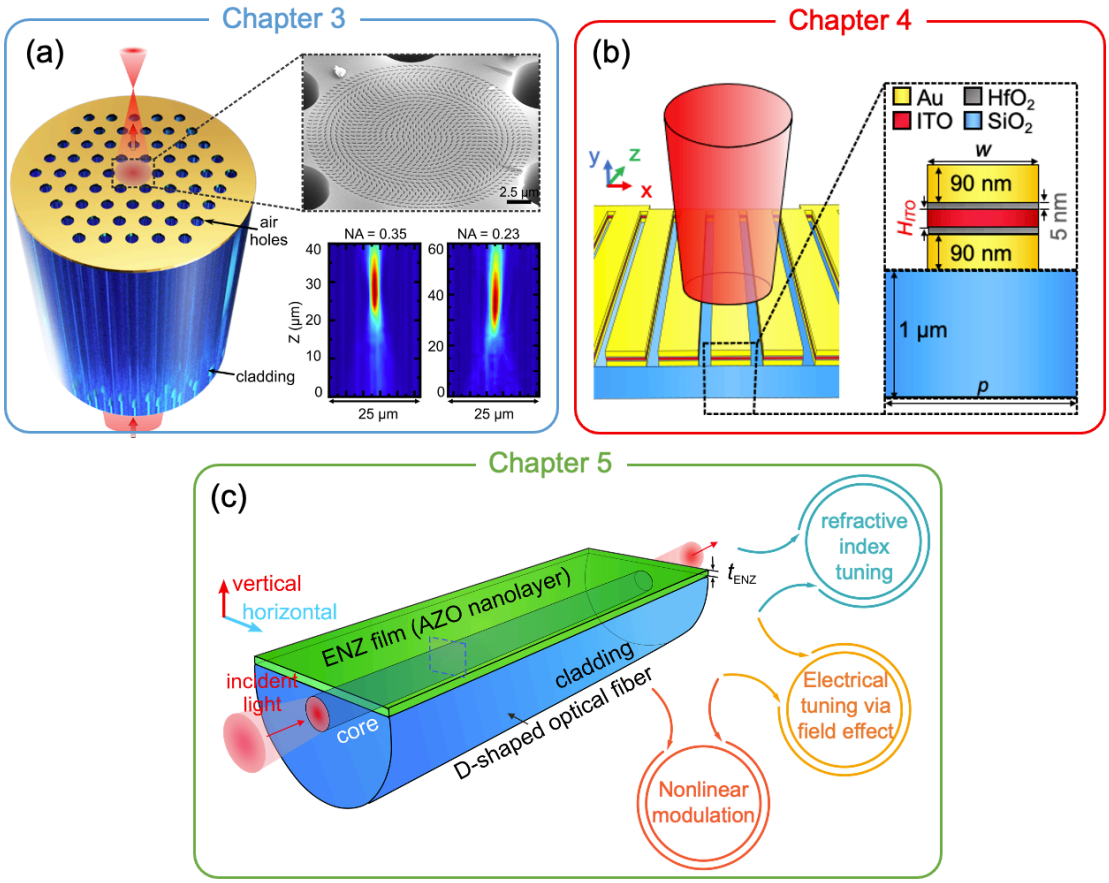

Figure 1-2 Overview of this thesis. Chapter 3 presents photonic crystal fiber metalens. Chapter 4 describes gate tunable plasmonic optical filter. Chapter 5 investigates the excitation of epsilon-near-zero mode in optical fiber.

Chapter 3 presents an experimental development of photonic crystal fiber metalens (Figure 1-2a). We investigate an ultrathin optical metalens directly patterned on the end facet of large mode area photonic crystal fiber (LMA-PCF) that can focus the outcoming light

in telecommunication wavelengths. The methodology of geometric phase, the nanofabrication, and the experimental demonstration of LMA-PCF metalens will be discussed in this chapter, as well as the performance and potential improvement of PCF metalens. The ultrathin optical fiber metalens may find novel applications in optical imaging, sensing, and fiber laser designs.

Chapter 4 discusses gate-tunable plasmonic optical filter incorporating a sub-wavelength patterned metal-insulator-metal metasurface heterostructure (Figure 1-2b). A thin transparent conducting oxide layer is embedded in the insulator layer to form a double metal-oxide-semiconductor configuration. The optical property of heavily n-doped indium tin oxide is electrically tuned by the formation of a thin active epsilon-near-zero (ENZ) layer at the interfaces. We numerically show that the amplitude modulation (~40%) and shift of transmission peak (~40 nm) at telecommunication wavelengths can be achieved with applied bias (0-5 V). This work is an essential step toward a realization of compact tunable photonic integrated devices and could potentially be applied in optical fiber platforms.

Chapter 5 presents the study on experimental excitation of a highly confined ENZ mode in a side-polished optical fiber coated with a deep subwavelength thick layer of aluminum-doped zinc oxide (AZO) (Figure 1-2c). The uniform AZO layer on the fiber was fabricated by the atomic layer deposition technique and optimized to exhibit close-to-zero permittivity at the near-infrared wavelength. Highly polarization- and wavelength-dependent transmission with strong strength of resonance is observed in the ENZ-coated fiber. In addition, the transmission resonance can be controlled through the dispersion engineering of the fundamental mode of the fiber and the ENZ mode supported by the AZO thin film. We further studied that the hybrid resonance in the ENZ fiber can be actively tuned

through the refractive index of the surrounding medium and the large nonlinearity of the ENZ film, as well as the design, nanofabrication, and characterization of the ENZ-optical fibers. These ENZ fibers serve as emerging optical platforms for developing next-generation in-fiber devices, such as advanced in-fiber ultrafast optical switches, modulators, optical filters, mode-locked fiber lasers, and in-fiber optical gas or biomolecule sensors.

Chapter 6 concludes the thesis followed by a brief outlook of tremendous opportunities for photonic devices such as in-fiber devices and active metadevices combining with flexible design of metasurfaces and zero-index photonics.

Chapter 2 Electromagnetic Wave Properties of Metasurface and Zero-Index Photonics on Optical Fibers

This chapter focuses on the interaction of light propagating in optical fiber with integrated metasurfaces and zero-index materials. It begins with an overview of the basic properties (*i.e.,* mode profiles and phase profile) of optical fibers in Section 2.1 followed by the fundamental electromagnetic properties of metasurfaces, different methods of phase control (*i.e.,* Huygens metasurfaces, waveguide-based metasurfaces, and geometric phase), and conventional flow of metasurfaces design in Section 2.2. We also present the analysis of gate-tunable metasurfaces by combining the Drude-like dielectric function of transparent conducting oxides (TCO) and field-effect dynamics of the metal-insulator-semiconductor (i.e., TCO) heterostructure for the manipulation of optical properties in Section 2.3. Section 2.4 discusses the optical properties of epsilon-near-zero (ENZ) material, the properties of ENZ mode on doped transparent conducting oxide thin film, and the phase matching method of ENZ mode in optical fiber. The simulation on the excitation of epsilon-near-zero resonance in ultra-thin indium oxide shell embedded nanostructured optical fiber was published in K. Minn, A. Anopchenko, J. Yang *et al.,* Scientific Reports 8, 2342 (2018) [*39*].

2.1 Basic properties of optical fibers

The conventional standard optical fiber (*i.e.,* step-index fiber) is comprised of a GeO_2-doped silica with weight of 4% as a core with a higher refractive index than the surrounding pure silica glass cladding. The material refractive index dispersions of glasses for the doped-core and the cladding can be described by the standard Sellmeier expansion [*40*]

$$n(\lambda) = \sqrt{1 + \sum_{i=1}^{3} \frac{A_i + f(C_i - A_i)\lambda^2}{\lambda^2 - (B_i + f(D_i - B_i))^2}} \quad (2\text{-}1)$$

where n is the refractive index of material, f is the doped weight ratio, λ is wavelength and A_i, B_i, C_i, D_i are Sellmeier coefficients listed in Table 2-1.

Table 2-1 Coefficients for standard Sellmeier expansion

i	1	2	3
A_i	0.6961663	0.4079426	0.8974794
B_i	0.0684043	0.1162414	9.896161
C_i	0.80686642	0.71815848	0.85416831
D_i	0.068972606	0.15396605	11.841931

With proper design according to geometry and material dispersion, optical fiber can guide light in the core regime by the principle of total internal reflection. Step index fibers are cylindrically symmetric and dielectric waveguides. They can be modeled and solved for the electromagnetic fields that propagate in the fiber. The number of optical modes that exists in the fiber can be calculated by the normalized frequency (V-number)

$$V = \frac{2\pi a}{\lambda}\sqrt{n_1^2 - n_2^2} \quad (2\text{-}2)$$

where a is the radius of fiber core, λ is operation wavelength at vacuum, n_1 and n_2 are the refractive indices of the core and cladding, respectively. For any value of V larger than 2.405, more than one mode can propagate in the fiber. Therefore, with chosen refractive indices of the core and cladding materials, the case of single mode fiber has limited core radius. Here, we take a multimode step index fiber (a = 20 μm, λ = 1.55 μm, n_1 = 1.47 and n_2 = 1.45, the V-number = 24.5) as an example to discuss the first six linearly polarized (LP) modes. Figure 2-1 depicts the electric field of LP_{01} (*i.e.,* HE_{11} or fundamental mode), LP_{02}, LP_{11} and LP_{21} modes [*41*]. The phase distribution of each mode is depicted as an inset at the top right. Note that the fundamental mode, LP_{01} (HE_{11}) has a uniform phase front within the Gaussian field

distribution. The other higher order modes have different phase distributions than each other. The phase distribution of guided mode and mode diameters in the fiber are critical parameters in the consideration of metasurfaces integration.

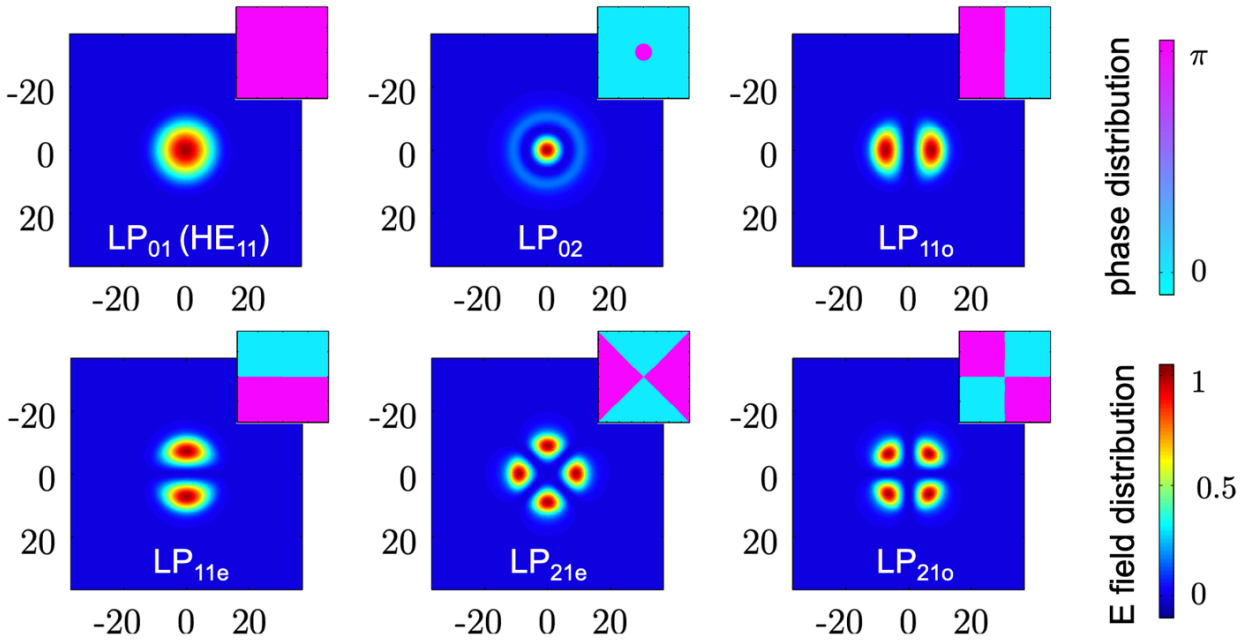

Figure 2-1 Electric field and (inset) phase distributions of six guided linearly polarized (LP) modes propagated in a multimode optical fiber (dimension in unit of μm) [*41*].

2.2 Basic analysis of metasurfaces

The essence of metasurfaces is to utilize arrays of antennas in the interaction in distance of subwavelength, separation, and geometric parameters to form a spatial modulation of optical wavefront design. The wavefront shaping in subwavelength resolution achieved through metasurfaces can funnel all incidence to a single beam instead of multiple diffraction orders. Moreover, metasurfaces enable us to engineer the interaction of nanostructure not only with the electric field, but also the magnetic field of light. The electric permittivity (ε) and magnetic permeability (μ) determine the propagation of light in matters. The

propagation of electromagnetic wave can be described by Maxwell equations as

$$\begin{aligned} \nabla \cdot \boldsymbol{D} &= \boldsymbol{\rho} \quad \text{(Coulomb's law)} \\ \nabla \times \boldsymbol{E} &= -\frac{\partial \boldsymbol{B}}{\partial t} \quad \text{(Faraday's law)} \\ \nabla \cdot \boldsymbol{B} &= 0 \quad \text{(Absence of free magnetic poles)} \\ \nabla \times \boldsymbol{H} &= -\frac{\partial \boldsymbol{D}}{\partial t} + \boldsymbol{J} \quad \text{(Ampere's law)} \end{aligned} \tag{2-3}$$

where $\boldsymbol{D}$ and $\boldsymbol{E}$ are electric displacement and electric field, $\boldsymbol{B}$ and $\boldsymbol{H}$ are magnetic induction and magnetic field, $\boldsymbol{\rho}$ is the charge density and $\boldsymbol{J}$ is the current density. The constitutive relation of $\boldsymbol{D}$, $\boldsymbol{E}$, $\boldsymbol{B}$ and $\boldsymbol{H}$ can be described as

$$\begin{aligned} \boldsymbol{D} &= \varepsilon \boldsymbol{E} \\ \boldsymbol{B} &= \mu \boldsymbol{H} \end{aligned} \tag{2-4}$$

By rationally designing the composition and geometry of the unit elements in the metasurfaces, the response of the electromagnetic wave can be modified through the permittivity or permeability of metasurfaces. A general solution of the electromagnetic wave interacted with metasurfaces from Maxwell equations can be described as

$$\boldsymbol{E_x} = A \exp\big(i(\boldsymbol{k} \cdot \boldsymbol{z} + \varphi)\big)\, \hat{\boldsymbol{x}} \tag{2-5}$$

Therefore, the design of metasurfaces can control the amplitude (A), phase (φ), wavefront ($\boldsymbol{k}$) and polarization ($\hat{\boldsymbol{x}}$) of electromagnetic wave. There are extensive studies on novel optical properties by manipulating light using the nanostructures in metasurfaces, such as negative refraction, invisible cloaking, artificial chirality, super resolution. Here we focus on the propagating phase of light induced by the metasurfaces. Conventional optical components, such as lens and waveplates, rely on the gradual phase accumulation in the propagation along optical paths, which are relatively large in dimension compared to the operating wavelength. In contrast, metasurfaces can produce abrupt phase change in

subwavelength thickness so that it is able to introduce the arbitrarily spatial variations via the designed light scatter according to Huygens' Principle.

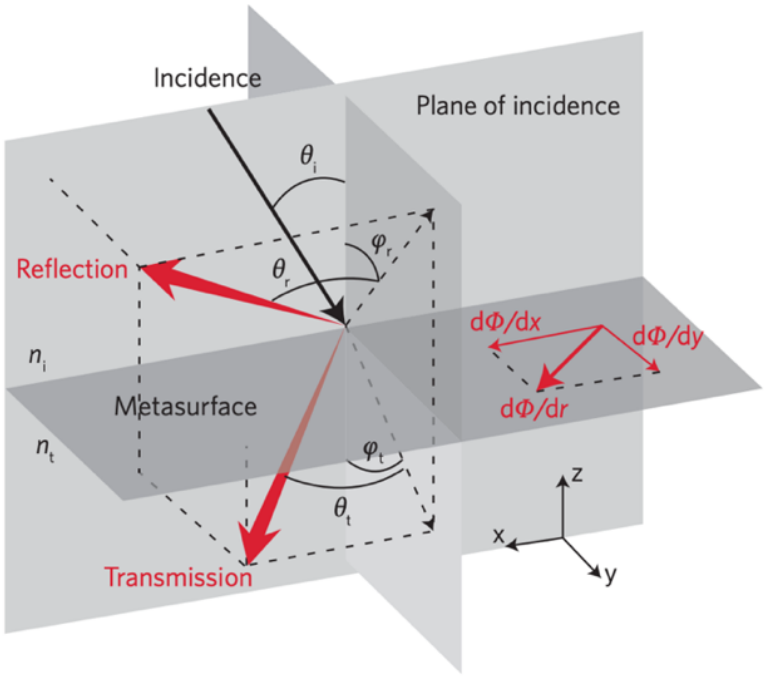

Figure 2-2 Generalized form of Snell's law for refraction and reflection. A gradient of phase jump at the interface $d\phi/dx$ along x direction reflect and transmit light arbitrarily to θ_r, and θ_t. The phase jump $d\phi/dy$ along y direction leads to out-of-plane refraction and reflection with φ_r and φ_t [*10*].

Assume a constant gradient of phase change introduced by a certain unit element at the interfaces, the conventional Snell's law of refraction is amended to the generalized form as

$$\begin{aligned} n_t \sin(\theta_t) - n_i \sin(\theta_i) &= \frac{1}{k_o}\frac{d\phi}{dx} \\ \cos(\theta_t)\sin(\varphi_t) &= \frac{1}{n_t k_o}\frac{d\phi}{dy} \end{aligned} \tag{2-6}$$

and the generalized form of reflection can be derived as

$$\begin{aligned} \sin(\theta_r) - \sin(\theta_i) &= \frac{1}{n_i k_o}\frac{d\phi}{dx} \\ \cos(\theta_r)\sin(\varphi_r) &= \frac{1}{n_r k_o}\frac{d\phi}{dy} \end{aligned} \tag{2-7}$$

where the angles in above equations are depicted in Figure 2-2, n_i, n_t, and n_r are the refractive indices of media on the incident, transmission, and reflection sides, k_o is the magnitude of wavevector at free space, $d\phi/dx$ and $d\phi/dy$ are the components of the phase gradient parallel and perpendicular to the plane of incidence. This interfacial phase gradient allows the transmitted and reflected light to bend into arbitrary directions in their own half space. To realize full control of the wavefront, the phase changes need to cover from 0 to 2π. Recently, there are extensive studies on various kinds of metasurfaces for the purpose of controlling 2π phase changes. These include (1) V-shaped metasurfaces, (2) gap-plasmon metasurfaces, (3) all-dielectric Huygens' metasurfaces, (4) high contrast metasurfaces and (5) geometric phase metasurfaces.

(1) V-shaped metasurfaces

The unit element of V-shaped metasurfaces has two nanorods with same length joint together at a designed angle Δ, which has been first demonstrated for 2π phase control [*9, 11*]. The proposed plasmonic resonator supports two modes, symmetric and antisymmetric modes due to the distributions of current (Figure 2-3a). The symmetric/antisymmetric mode can be excited with the incident polarization parallel/perpendicular to the symmetry axis of the resonator. With an arbitrarily polarized incidence, the two eigenmodes has cross polarizations: one maintains the same polarization angle as incidence carrying phase of α; the other attributed to anomalous components has cross polarization angle carrying phase of Δ-α, where Δ is the angle between two joint nanorods [*42*]. The large variation of scattered amplitudes and phases can be realized by changing the antenna geometry and joint angle (Figure 2-3b and 3c).

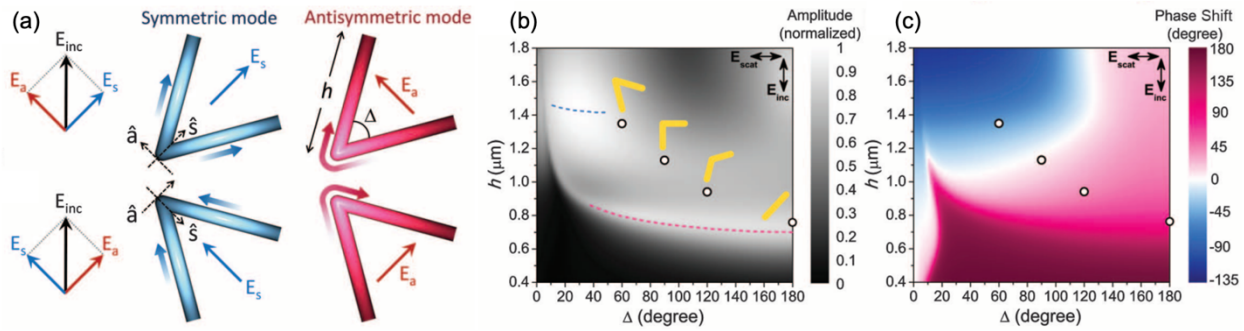

Figure 2-3 V-shaped metasurfaces [*9*]. (a) V-shaped resonant supports symmetric and antisymmetric modes. **(b)** Amplitude and phase shift of the cross-polarized scattered light for gold V-shaped resonant with various length *h* and angle between the rods *Δ*.

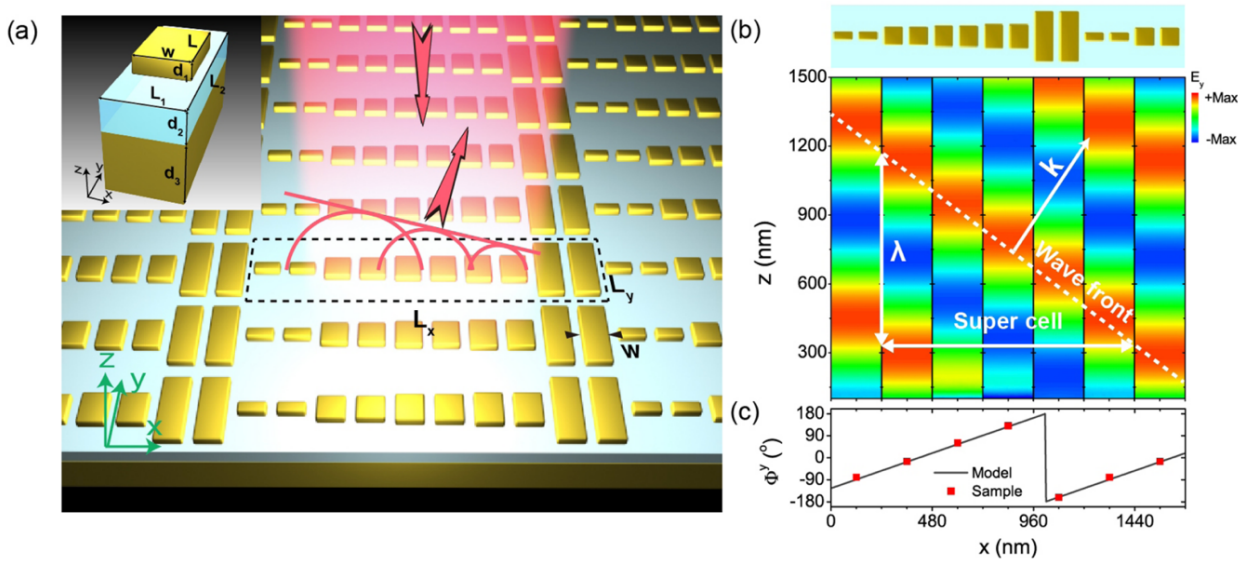

Figure 2-4 Gap-plasmon metasurfaces [*43*]**. (a)** Schematics of the designed metasurfaces with a unit cell (inset) consisting of a gold nanorod and a gold mirror ground layer separated by the MgF_2 spacer. **(b)** Simulated scattered electric field and **(c)** reflection phase of each unit elements.

(2) Gap-plasmon metasurfaces

The metal-insulator-metal structure (*i.e.,* gap-plasmon metasurface) comprises of a dielectric spacer sandwiched between a metallic resonator and a metallic ground sheet (Figure 2-4a) [*43*]. The strong magnetic field in the dielectric spacer (*i.e.,* gap-plasmon mode)

is due to the antiparallel induced currents on the top resonator and the ground sheet. In reflection, the subwavelength dielectric spacer supports the strong near-field coupling of top arrays and its mirror dipoles in the ground sheet. By controlling the dimension of the top resonator, 2π phase control in reflection could be achieved and the properties of beam deflection has been realized by constructing a linear phase gradient grating (Figure 2-4). This mechanism of gap-plasmon metasurfaces will be employed in our gate-tunable metasurfaces (Section 2.3) and gate-tunable optical filters (Chapter 4).

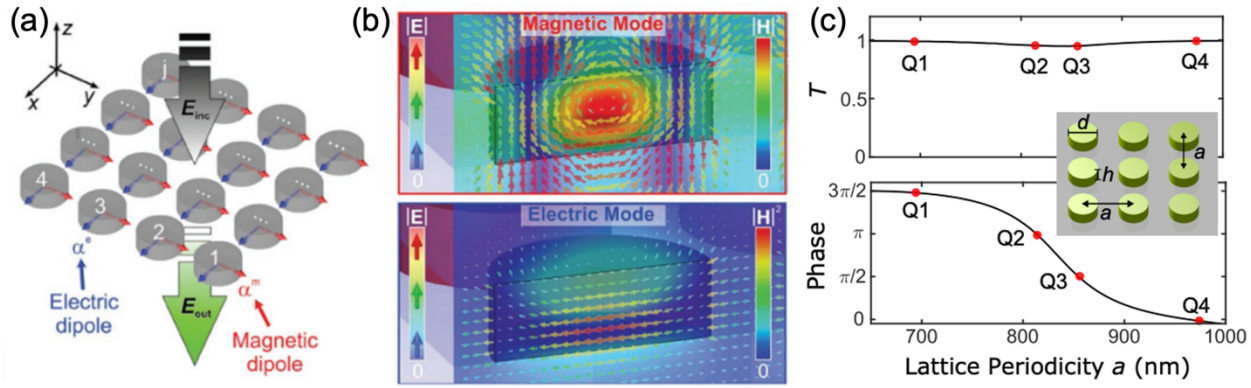

Figure 2-5 All-dielectric Huygens' metasurfaces. (a) Schematic of dielectric metasurfaces using nanodisks array [*44*]. **(b)** Electric (colored arrows) and magnetic (plain color) field distributions of magnetic and electric mode of Si nanodisk [*44*]. **(c)** Transmittance intensity and phase values of Huygens' metasurfaces at the operation wavelength [*45*].

(3) All-dielectric Huygens' metasurfaces

The high-refractive-index dielectric nanodisk can be designed to overlap spectrally comparable electric and magnetic resonances to achieve the condition of Huygens' metasurfaces with an optimal transmission (Figure 2-5a) [*44*]. The designed dielectric nanodisks, with low intrinsic losses, can support the coupling of incident light to generate circular displacement currents inside the structures, which is necessary for a strong

magnetic dipole resonance (Figure 2-5b). For instance, near-unity transmission and full 0-2π phase coverage can be realized by the localized electric and magnetic Mie-type resonances of low-loss silicon nanostructures (*i.e.,* Huygens' metasurfaces). The proposed metasurface can behave as electromagnetically dual-symmetric scatters (Figure 2-5c) [*45*].

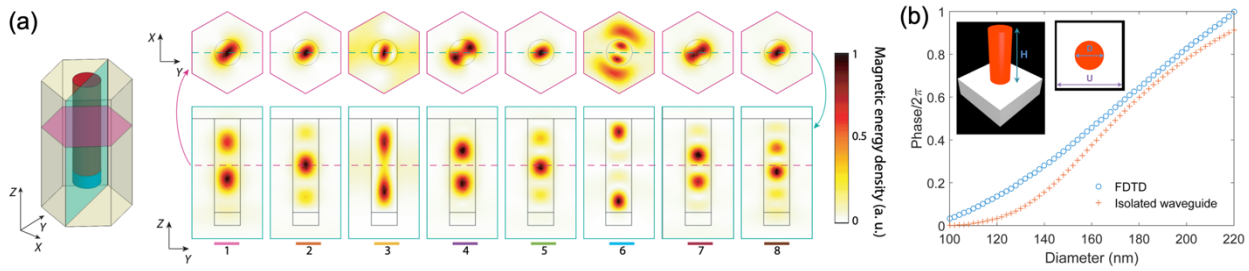

Figure 2-6 High contrast metasurfaces. **(a)** Magnetic field distributions of eight dominant resonant modes of a nanopillar array [*46*]. **(b)** Phase calculated by finite difference time domain simulation of the building block with diameter *D*, and the phase due to propagation in an isolated cylindrical waveguide, considering its fundamental mode HE_{11} [*47*].

(4) High contrast metasurfaces

Another type of dielectric nanostructures, high contrast metasurfaces composed of disconnected dielectric scatters in a periodic lattice, also can achieve simultaneous control of phase and polarization with high transmission. Each scatter can be considered as a waveguide, which supports Fabry-Perot resonances with low quality factors. In contrast to all-dielectric Huygens' metasurfaces with electric and magnetic dipole resonances, high contrast metasurfaces contain electric and magnetic dipoles, quadrupoles, and multiples. The optical energy of high contrast metasurfaces is concentrated inside each scatter so that the phase and amplitude are primarily determined by the geometry of the unit element (Figure 2-6a) [*46*]. For instance, full phase control can be realized by the means of the waveguiding effect via adjusting the diameter (100-220 nm) of TiO_2 nanopillar with material

refractive index of 2.5-2.8 at visible wavelength. The nanopillars should be tall enough (600 nm) to provide 2π phase coverage. The phase of the waveguide is given by $\phi_{WG} = 2\pi n_{eff} H/\lambda$, where n_{eff} is the effective index of the fundamental mode (HE_{11}), H is the nanopillar height as well as the propagation length, and λ is the operation wavelength. The effective index, n_{eff} can be computed using a single step-index circular waveguide model (Figure 2-6b) [*47*].

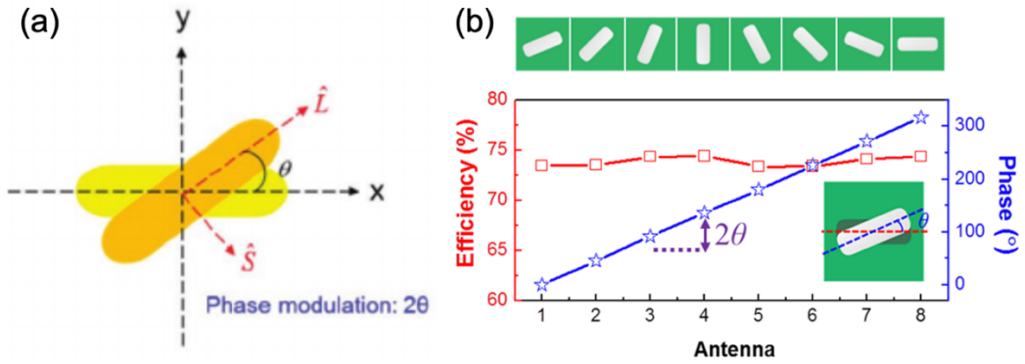

Figure 2-7 Geometric (Pancharatnam-Berry) phase metasurfaces. **(a)** Schematic of a unit element with rotation angle θ [*44*]. **(b)** Conversion efficiency and phase modulation for nanoantennas of equal dimensions oriented at various angles [*48*].

(5) Geometric (Pancharatnam-Berry) phase metasurfaces

Besides the phase accumulation introduced in the previous methods, a completely different approach to introduce abrupt phase changes is to utilize geometric phase (*i.e.*, Pancharatnam-Berry phase) (Figure 2-7a) [*10*]. It is associated with circular polarization and created by using anisotropic scatter at subwavelength scale with spatially varying orientations as part of the same geometric parameters.

The relation of polarization and phase can be revealed by using the Jones calculus. Generally, an anisotropic scatterer can be described in the Jones matrix as

$$\boldsymbol{M}_{ani} = \boldsymbol{R}(-\theta)\begin{pmatrix} t_o & 0 \\ 0 & t_e \end{pmatrix}\boldsymbol{R}(\theta) \tag{2-8}$$

where t_o and t_e are the complex scattering coefficients for incident light linearly polarized along the ordinary and extraordinary axes of the anisotropic scatterer respectively, and θ is the orientation angle of the slit aperture. The rotation matrix can be depicted as

$$\boldsymbol{R}(\theta) = \begin{pmatrix} \cos(\theta) & \sin(\theta) \\ -\sin(\theta) & \cos(\theta) \end{pmatrix} \tag{2-9}$$

The scattered light from the anisotropic scatterer in the forward direction can be described as

$$\begin{aligned} \boldsymbol{E}_T^R &= \boldsymbol{M}_{ani} \cdot \boldsymbol{E}_I^R = \frac{t_o + t_e}{2} \boldsymbol{E}_I^R + \frac{t_o - t_e}{2} \boldsymbol{E}_I^L \exp(\mp i2\theta) \\ \boldsymbol{E}_T^L &= \boldsymbol{M}_{ani} \cdot \boldsymbol{E}_I^L = \frac{t_o + t_e}{2} \boldsymbol{E}_I^L + \frac{t_o - t_e}{2} \boldsymbol{E}_I^R \exp(\mp i2\theta) \end{aligned} \tag{2-10}$$

where E_T and E_I are the transmitted and incident wave, and the superscripts of L and R indicate left and right circular polarization [*10, 48*]. The first terms in Equation (2-10) represent circularly polarized scattered waves with the same handedness as the incident light. The second terms represent opposite circularly polarized scattered waves carrying an additional $\mp 2\theta$, which can cover from 0 to 2π by rotating the anisotropic scatterer from 0 to 180° (Figure 2-7b). In Chapter 3, we elaborate the design of photonic crystal fiber metalens using this geometric phase method.

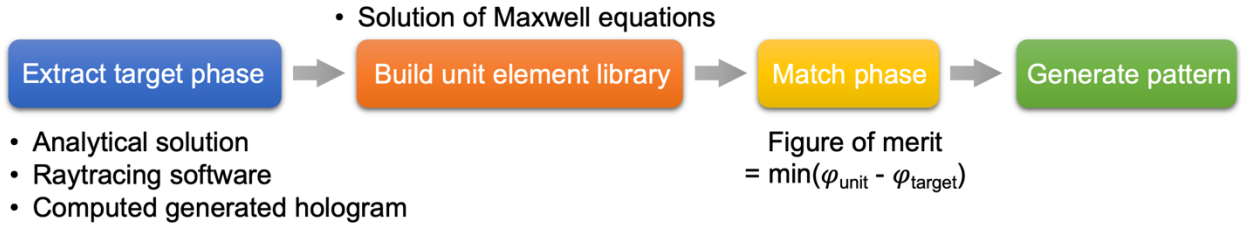

Figure 2-8 Flow chart of conventional metasurface design.

There is a general process of conventional metasurface design as shown in Figure 2-8. First, we can extract target optical phase profiles from analytical solutions or raytracing software (Zemax, Code V or ASAP). For instance, we can calculate the optical phase of a beam deflector, $\varphi(x) = 2\pi\, x\, sin(\theta)/\lambda$, where x is the location of unit element, θ is deflection angle and λ is operation wavelength. Second, the unit element library in parameter sweep can be built by calculating the phase and amplitude of transmission or reflection via photonic simulation software such as COMSOL Multiphysics, Computer Simulation Technology (CST Studio Suite) or Lumerical Solution. Lastly, the candidate unit element can be chosen from the library by minimizing the phase difference with the target phase to generate the whole metasurface pattern. The design of metalens followed the flow chat of Figure 2-8 will be elaborated in Chapter 3.

2.3 Principle of gate-tunable conducting oxide metasurfaces

The electromagnetic responses of the metasurfaces discussed above are fixed after fabrication due to the static electron density of the noble metals or semiconductors, the optical constants of the dielectric materials, and the fixed structural geometries. These limit the practical and more advanced applications of the metasurfaces such as dynamic manipulation of the wavefront of the incident electromagnetic wave. Therefore, there is a significant need to develop tunable metasurface components for post-fabrication tunability and novel functionalities. Electrical modulation is one of the physical mechanisms for the modulation of the complex refractive index of semiconductor. Typically, the electronic modulation requires contact layers such as a metal or semiconductor; thus, they can be easily integrated with metallic- or semiconductor-based metasurfaces operating in transmission

or reflection. Several electrically active materials have been utilized to control the metasurface properties. One of active materials, TCOs are semiconductors with high transmittance at visible and near-infrared wavelengths. They can be heavily n-type doped with typical free charge carrier concentrations, N of 10^{19} to 10^{21} per cm^3. Thus, they exhibit metallic characteristics (*e.g.,* negative permittivity) in the visible or near infrared wavelength (Figure 2-9) [*49-51*].

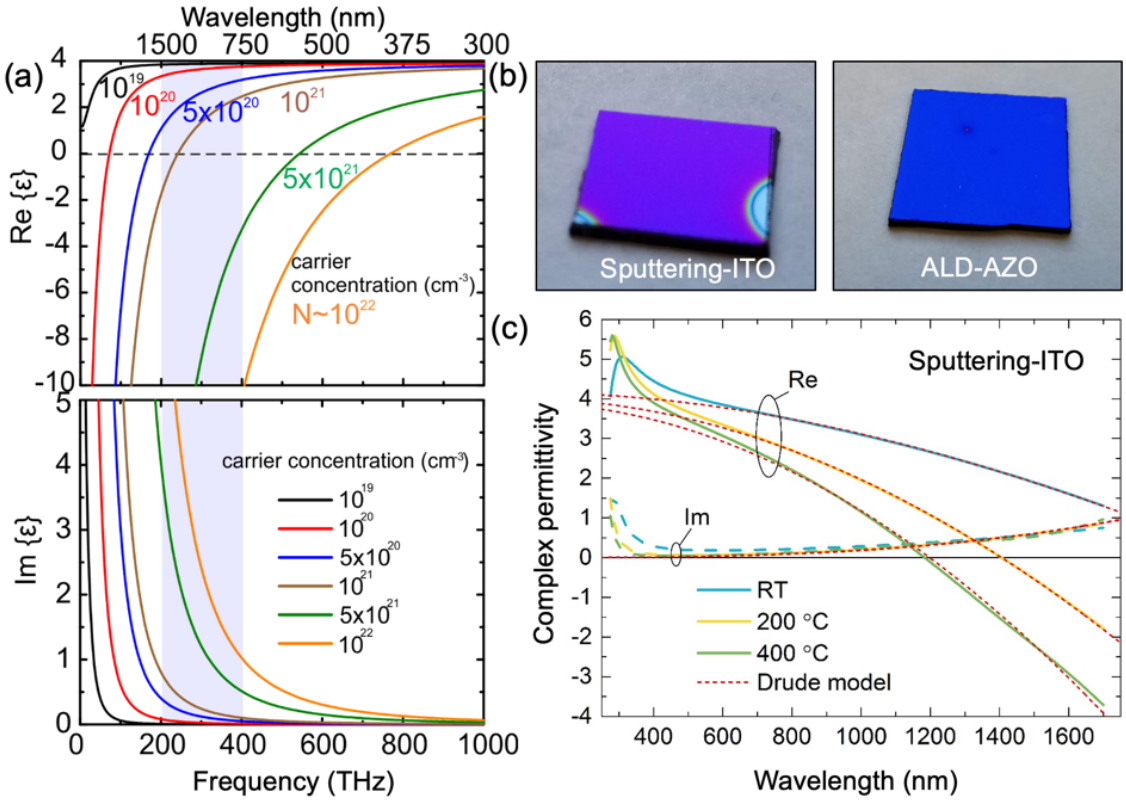

Figure 2-9 (a) Complex permittivity of indium tin oxide (ITO) with different carrier concentrations N, calculated by the Drude-Lorentz model [*52*]. **(b)** TCO can be fabricated by various fabrication techniques. The examples shown here are ITO films fabricated by magnetron sputtering and AZO films fabricated by atomic layer deposition [*53*]. **(c)** The measured permittivity of ITO thin films fabricated in different sputtering temperatures. Carrier concentration and thus ENZ wavelengths can be tuned routinely. The Drude model precisely described the permittivity in the wavelength range of most interest.

While the conducting oxides exhibit metallic properties, their material loss is significantly lower than noble metals (*e.g.,* gold and silver) due to the carrier concentration of the materials, making them attractive as alternative plasmonic materials for metasurfaces. Several research groups have studied the plasmonic properties of the conducting oxides in different plasmonic or metamaterial structures, which shows opportunities for visible or near infrared plasmonic applications with lower loss [*49, 51, 54-68*]. The complex permittivity (ε) of a conducting oxide is strongly related to its intrinsic carrier concentration (N). Hence, the complex refractive index can be derived by using the conventional free-electron Drude model. The dispersive permittivity of a conducting oxide can be expressed as

$$\varepsilon(\omega) = \varepsilon_{\infty} - \frac{q^2 N}{\varepsilon_0 m_e^*}\left(\frac{1}{\omega^2 + i\omega\gamma}\right) \tag{2-11}$$

where ω is the angular frequency of the incident wave, m_e^* is the effective electron mass in TCO films, N is the carrier concentration of TCO, and γ is the collision frequency of TCO [*52*]. The complex permittivity of TCO can be evaluated in Equation 2-11 according to the carrier concentration. Figure 2-9a shows the calculated complex permittivity of indium tin oxide (ITO), one of the most common TCO materials [*52*]. Note that the material dispersion shifts significantly to a shorter wavelength with a higher carrier concentration. The plasma frequencies shift all the way from near-infrared ($N \sim 10^{19}$ cm^{-3}) to ultraviolet range ($N \sim 10^{21}$ cm^{-3}) with different carrier concentrations of the material. For example, an operation wavelength at 1550 nm, the real part of the permittivity can be tuned from positive (dielectric property) to negative value (metallic property) by changing the carrier concentration, hence exhibiting the tunable potential of TCO for active metasurfaces. Note

that the carrier concentration of TCO can be varied by different fabrication methods, such as atomic layer deposition (ALD), chemical vapor deposition, magnetron sputtering, and pulsed laser deposition (sputtered ITO and ALD-fabricated aluminum-doped zinc oxide (AZO) in Figure 2-9b), by post-processing techniques (*e.g.,* annealing), and by deposition conditions [*49, 51, 52, 60, 68*]. In addition, the standard free electron Drude model (red dashed curves in Figure 2-9c) describes the permittivity accurately in the visible and near-infrared regime.

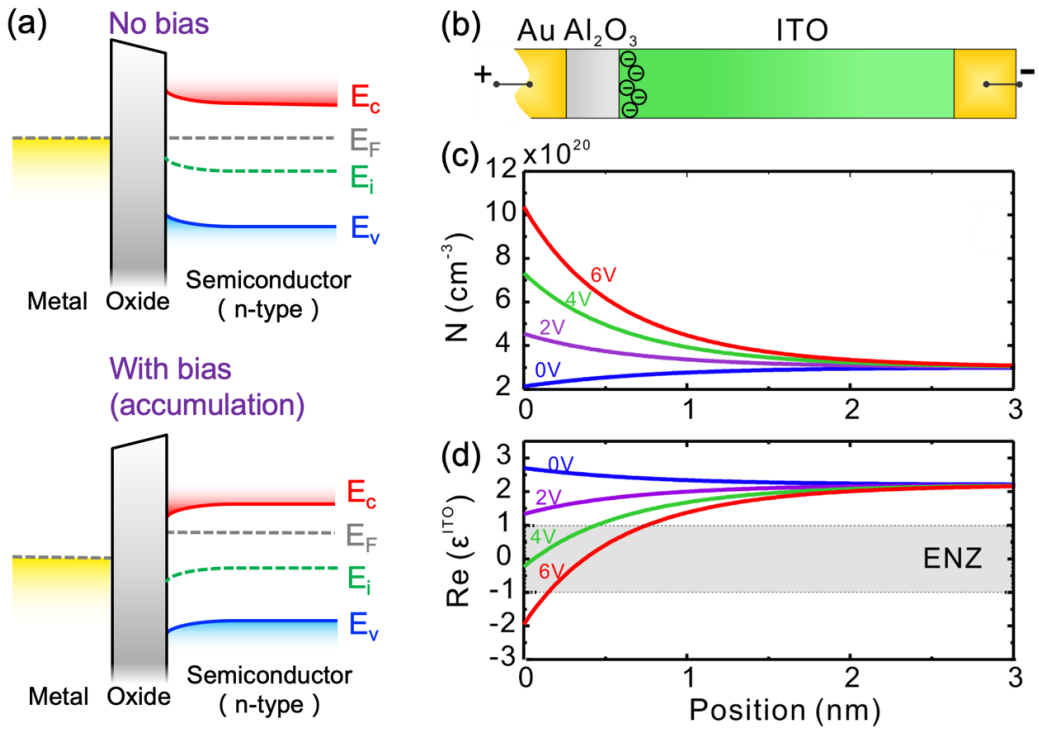

Figure 2-10 Conducting oxide field-effect dynamic for the manipulation of optical properties. **(a)** Schematic of the field-effect structure and **(b)** their corresponding band diagram under bias. **(c)** Spatial distribution of the carrier concentration *N* under different applied voltages. **(d)** The corresponding real part of ITO permittivity at a wavelength of 1550 nm [*69*].

Notably, a metal-oxide-semiconductor (MOS)-field effect structure can be formed by combining the TCO film with a dielectric insulator and the metal layer to create a gate. By applying external bias, the Fermi level of TCO and band alignment can be modulated in the

following way in Figure 2-10a. Thus, the carrier distribution and the permittivity of the material can be modulated accordingly. Figure 2-10b shows the accumulation layer revealed by the field-effect electrostatic calculations. The carrier concentration of the ITO film at the Al_2O_3-ITO interface increases three times as compared to the bulk value when applying an electric bias of 4 V in Figure 2-10c, leading to the change of permittivity (ε') for different applied biases at an operation wavelength of 1550 nm [*69*].

In addition, the permittivity of the ITO can reach the epsilon-near-zero (ENZ) region ($-1 < \varepsilon' < 1$) at an applied bias of 2 to 4 V (highlighted by the grey area in the inset of Figure 2-10d). When satisfying the ENZ condition, a considerable enhancement of the electric field can be realized in the accumulation layer of the ITO; this field enhancement provides promising opportunities for light manipulation in advanced devices [*70-74*]. Since the drift velocity of electrons that form the accumulation layer can exceed terahertz, with the small footprint and low capacitance of nano-devices, the modulation frequency could potentially exceed tens of gigahertz (up to terahertz depending on the resistor-capacitor circuit). For instance, GHz modulation was demonstrated in a TCO-Si photonic modulator [*52, 75*], which can be applied to electrical TCO meta-devices. Note that the field-effect dynamics also depend strongly on the material properties such as the Fermi level, effective electron mass, electron mobility, material bandgap, and the work function of the materials. Designing the structure with the proper metal-dielectric-semiconductor combination can increase the carrier concentration modulation of depletion or accumulation layer (*i.e.,* Debye length). In Chapter 4, we design an optical filter based on the mechanism of gate-tunable metasurface and optimize its performance in simulation.

2.4 Epsilon-near-zero mode in optical fiber

In electromagnetism, the electric permittivity denoted by epsilon (ε) is a complex number relate to optical properties of materials, which can be described as

$$\varepsilon(\omega) = \varepsilon'(\omega) + i\varepsilon''(\omega) \tag{2-12}$$

where ω is frequency, ε' and ε'' are the real and imaginary part of permittivity, respectively. In nature, dielectric has positive ε' and metal has negative ε'.

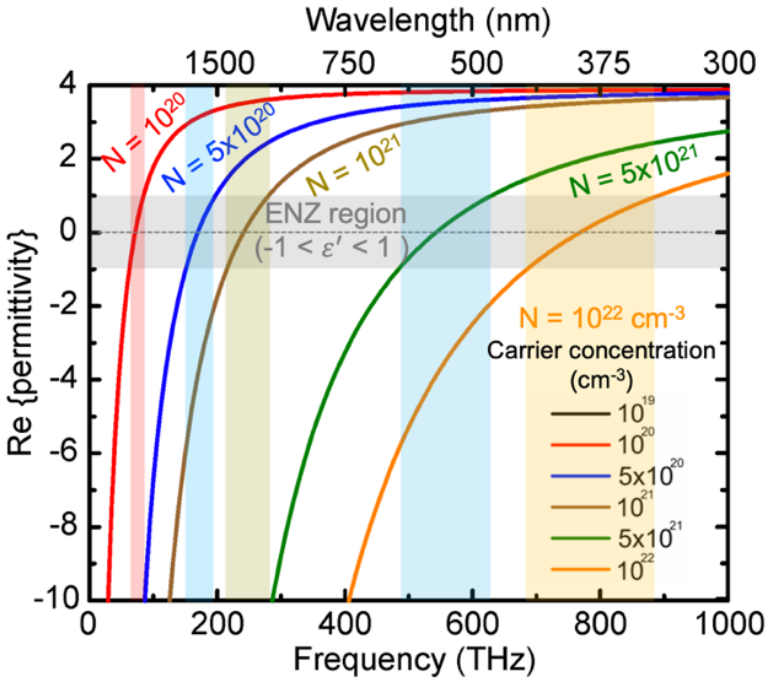

Figure 2-11 The electric permittivity of dielectric and metal and permittivity dispersion of transparent conducting oxide (indium tin oxide, ITO) with different carrier concentrations [*52*].

Recent studies suggest that highly doped transparent conducting oxide can possess the real part of permittivity vanishing at certain wavelength (Figure 2-11, right) [*52*]. The wavelength range with the real part of permittivity between ±1 is so-called epsilon-near-zero regime. The permittivity dispersion of transparent conducting oxide in different doped ratios can be depicted by Drude model in Equation 2-11. For instance, the epsilon-near-zero

regime of the ITO can be tuned to different wavelength ranges by varying the carrier concentration.

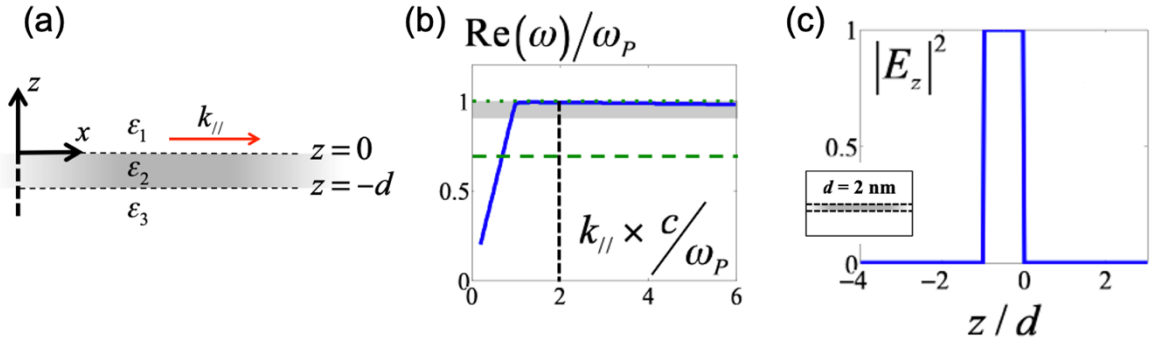

Figure 2-12 Theory of epsilon-near-zero modes in ultrathin film [*76*]. (a) A three-layer structure containing a layer with thickness d and two-infinite regions. **(b)** ENZ mode dispersion supported by a layer with thickness of 2 nm. **(c)** Profile of the intensity of the *z* component of the electric field versus the spatial variable z normalized the thickness *d*.

The thin layer of ENZ material can support the plasmon polariton mode with a highly confined and enhanced optical field (*i.e.,* ENZ mode) (Figure 2-12a) [*76-79*]. Different than the radiative mode (short range mode) excited on thin plasmonic film with dispersion lying above the light line, ENZ mode (long range mode) has dispersion lie below the light line. It is classified as an extreme case of surface plasmon polariton mode (Figure 2-12b) [*76*]. Another characteristic of ENZ mode is the strong light enhancement and confinement in ENZ layer (Figure 2-12c). The electric field boundary conditions require the displacement field at the interface of air and ENZ thin film to be continuous and can be described as

$$\boldsymbol{D_2} \cdot \boldsymbol{n_{12}} = \boldsymbol{D_1} \cdot \boldsymbol{n_{12}} = \varepsilon'_{\perp 1} E_1 = \varepsilon'_{\perp 2} E_2 \qquad (2\text{-}13)$$

when $\varepsilon'_{\perp 2}$ close to zero, the electric field, E_2 inside the ENZ medium is strongly enhanced. In the case of vacuum permeability, near-zero permittivity leads to near-zero refractive index. This causes the group velocity inside the medium to zero the phase velocity to diverge and

wavelength to expand, which leads to the enhancement of light-matter interaction. These ENZ properties are unique for the compact device-level applications, such as emission control [*34*], vortex generation [*80*], high harmonic generation [*38*] and ultrafast optical switching [*81*], *etc*. The excitation of ENZ mode in the semi-infinite three-layer (insulator-metal-insulator) geometry can be realized by prism coupling with Kretschmann geometry or formation of grating. These ENZ modes excite on planar substrates have relatively short light-matter interaction length (*i.e.,* propagation length). In our work, we utilize optical fiber to provide a simplified version of ENZ mode excitation via phase matching condition between the fiber mode and the ENZ mode with longer light-matter interaction distance. To illustrate the coupling mechanism, we investigate the excitation of ENZ resonance on a modified version of single mode fiber with an ENZ thin film embedded in the nano-hollow channel. The ENZ fiber waveguide design consists of three concentric cylindrical shells. The two outermost shells act as cladding and core respectively. The innermost thin shell is made of ENZ material that surrounds the hollow central channel. The subwavelength thickness of the ITO shell ensures that the guided fundamental fiber mode can be coupled to the thin film ENZ mode. The domain of the ENZ mode existence is limited to a thickness much less than the plasma wavelength of the material with vanishing permittivity.

A schematic of the proposed ENZ optical fiber design is shown in Figure 2-13a. Section (I) of the structure is the hollow nanobore fiber which consists of the outer silica cladding, GeO_2-(weight ratio 9%) doped silica core of 4-μm diameter and a hollow central channel of 200 nm diameter. Section (II) depicts the ENZ fiber where the inner surface of the central hollow channel is coated with 10 nm layer of ITO. Figure 2-13b shows the glass-ITO-air structure that is considered in calculating the ENZ mode. The ENZ mode can be

excited from the glass half space using Kretschmann configuration [*82*]. The structure is comprised of a thin ITO layer having the same thickness as the ITO shell inside the ENZ fiber sandwiched between the air and glass half-spaces. For the designed ENZ material, ITO carrier concentration of 10^{21} per cm^3, with the large frequency limit ε_∞ = 3.9, plasma frequency ω_p = 3.3722×10^{15} s^{-1}, and damping coefficient γ = 2.0263×10^{14} s^{-1}, the dielectric function of ITO can be calculated from the Drude model in Equation 2-11. The real part of permittivity of the ITO crosses zero at wavelength of 1068 nm and with small imaginary part of permittivity (ε'' = 0.41) (Figure 2-14).

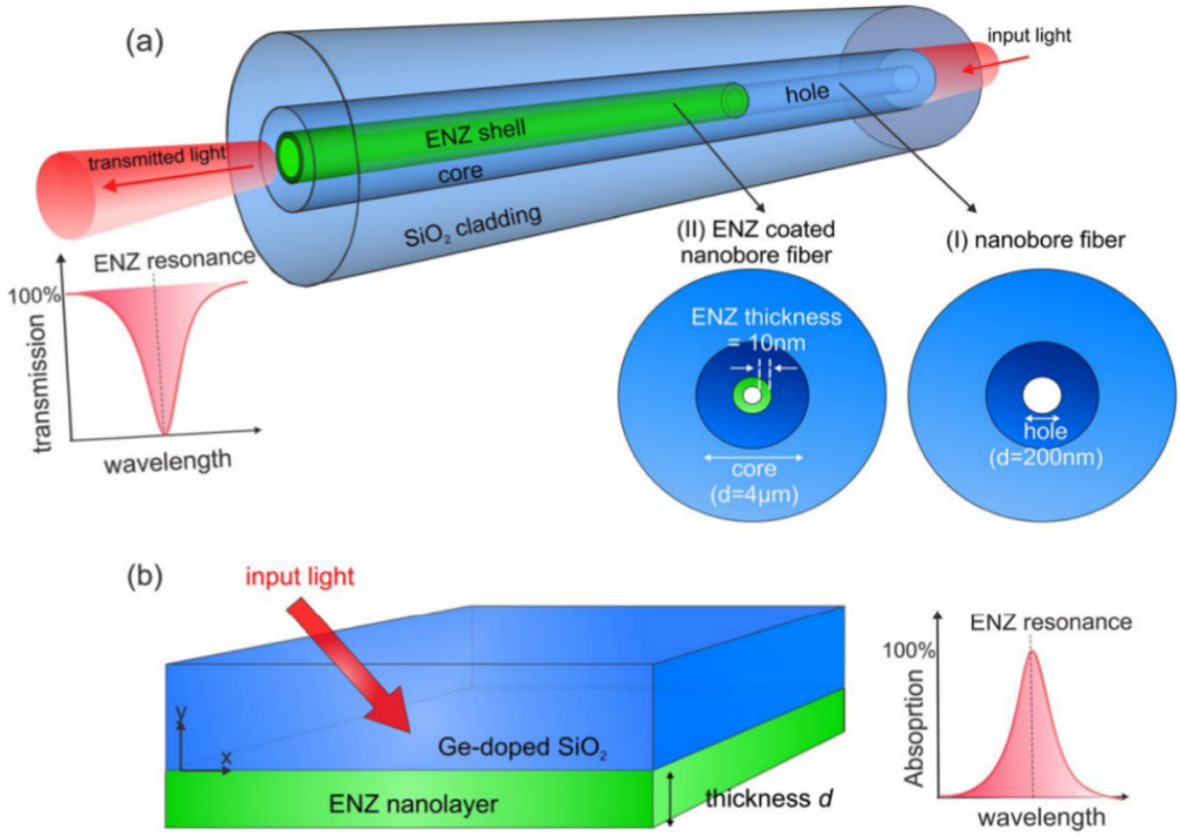

Figure 2-13 (a) Schematic of the proposed ENZ fiber waveguide design. The inserts are cross-sections of the ENZ fiber (coated with ITO ENZ nano-shell) and hollow nanobore fiber (without ITO ENZ nano-shell). **(b)** Geometry of glass (GeO_2 doped silica)-ITO-air structure with ITO layer thickness *d* for excitation of ENZ mode.

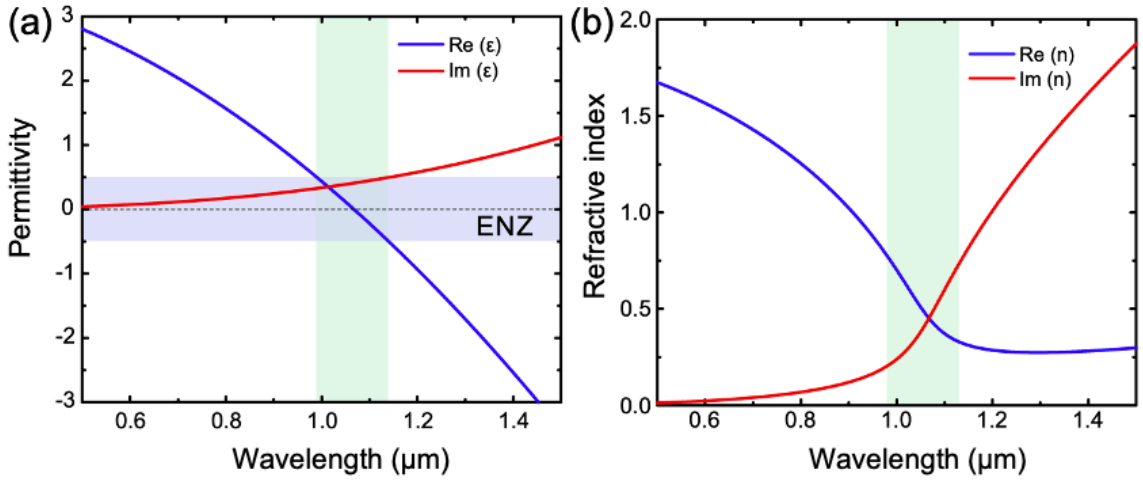

Figure 2-14 (a) Complex permittivity and **(b)** complex refractive index dispersions of ITO for case of the ENZ resonance in the nanobore fiber.

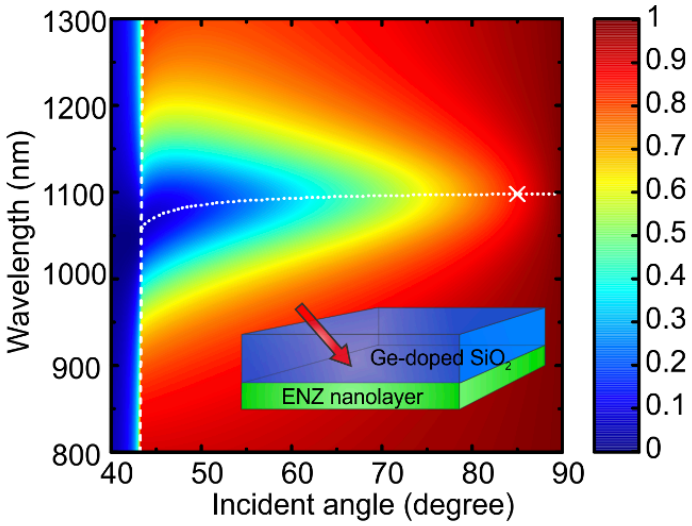

Figure 2-15 Thin-film ENZ modes in three-layer structure. Contour plot of reflectance as a function of wavelength and incident angle for glass-ITO-air structures. ITO layer thickness is 20 nm; the white dashed lines are the light lines and critical angles; the white dotted lines are the ENZ dispersion curves; and the white crosses are the phase-matching angles and wavelengths.

To examine the coupling mechanism between the guided mode in the nanobore fiber and the thin film ENZ mode, we investigate their dispersion characteristics. The effective index of the fundamental guided core mode of the nanobore fiber as a function of excitation

wavelength was modelled using the finite difference numerical waveguide analysis method. The effective index of non-radiative ENZ mode supported by the glass-ITO-air structure was modelled using the transfer matrix method and traced from the minimum reflectivity. The coupling between the fundamental mode of the nanobore fiber and the thin film ENZ mode occurs at the phase matching wavelength, at which point the effective index functions of the two modes intersect and their momenta are equal.

The dispersion of fundamental mode of the hollow nanobore fiber was obtained from the simulation of the cross-section as depicted in the right insert of Figure 2-13a. A frequency dependent real part of the effective index of the mode n_{eff} was calculated ($n_{eff} = c\beta/\omega$, where β is the propagation constant in the fiber for a given wavelength). We can obtain the dispersion curve of the ENZ mode from the glass-ITO-air geometry as shown in Figure 2-13b. The reflectance was calculated for varying incident angles and wavelengths in the air. Contour plots of the reflectance as a function of incident angle and excitation wavelength is presented in Figure 2-15. The dashed white lines show the so-called light lines or the critical angle dispersion. The dotted white lines show the locus of the minimum reflectivity at a fixed incident angle or the ENZ mode dispersion. For small enough thickness of ITO layer ($d < \lambda/50$), incident light from glass onto ITO nanolayer is perfectly absorbed at large angles and at resonant wavelength which corresponds to the ENZ polariton mode [*83*]. Thus, for each incident angle, the wavelength that corresponds to minimum reflectance is traced to calculate the effective index of the thin film ENZ mode (Figure 2-15). The thin film ENZ mode dispersion curves for 5 nm, 10 nm, 15 nm, and 20 nm ITO layer thicknesses were calculated to phase match with fiber fundamental mode. The effective index of the thin film ENZ modes for four different ITO layer thicknesses (dash curves) and the fundamental mode of hollow

nanobore fiber (blue dotted curve) were depicted in Figure 2-16. Thin film dispersion curves intersect the fiber fundamental mode dispersion at 1070 nm, 1079 nm, 1088 nm and 1098 nm wavelengths for four different thicknesses of ITO layer respectively. As the ITO thickness increases, the thin film ENZ dispersion curve shifts toward longer wavelengths and thus the phase matching wavelength with the fiber core mode increases.

Next, we verified the excitation of ENZ modes in the fiber at the above resonant wavelengths. Finite difference method was used to solve the Maxwell's equations on a cross-section of the ENZ fiber waveguide. The resulted fundamental mode has highest spatial field distribution within the ITO shell compared to other higher order modes. This ENZ mode was tracked over a wavelength range to calculate the modal loss as follows:

$$loss = -20log_{10}e^{-2\pi k/\lambda} \tag{2-14}$$

The k in Equation 2-15 is the imaginary part of the effective index and λ is operation wavelength. The modal loss curves were calculated in the same way for four different ITO shell thicknesses: 5 nm, 10 nm, 15 nm, and 20 nm.

Figure 2-16 shows the modal losses of the fundamental mode of the ENZ fiber for four ITO shell thicknesses (color shaded areas). Peak losses are observed at wavelengths 1071 nm, 1080 nm, 1092 nm and 1102 nm for four different ITO shell thickness. These resonances are in good agreement with the phase matching wavelengths of the fundamental mode propagating in the nanobore fiber and the ENZ modes supported by ITO thin film calculated above. The peak in the loss spectra is resulted from the excitation of ENZ mode and the strong confinement in the thin film. In Chapter 5, we can confirm the experimental excitation of the ENZ mode in aluminum zinc oxide coated D-shaped fiber via the phase matching

method elaborated here.

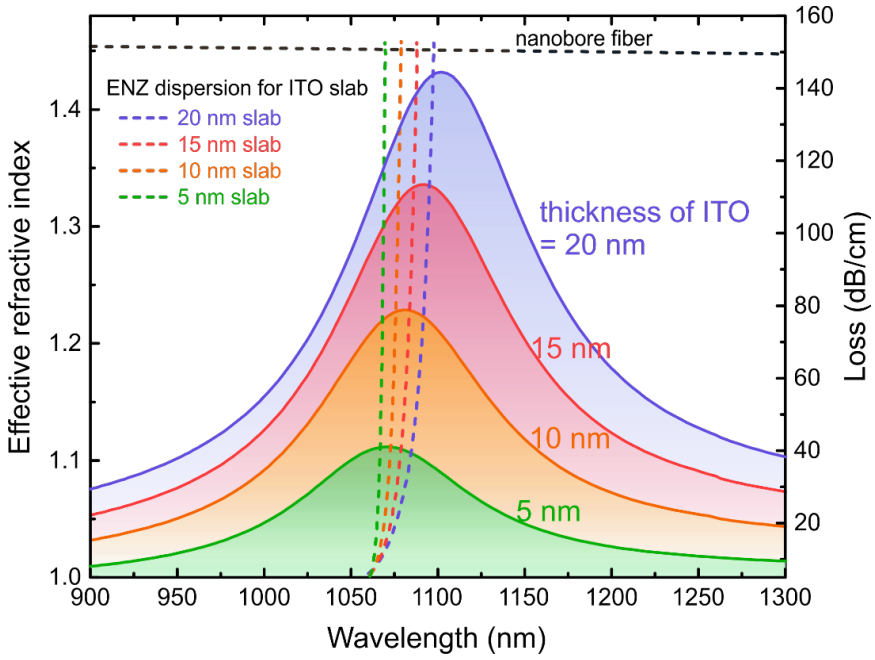

Figure 2-16 Phase matching conditions between fundamental waveguide mode in the hollow nanobore fiber and the ENZ mode of glass-ITO-air geometry for 5 nm, 10 nm, 15 nm, and 20 nm ITO layer thicknesses. The dotted curves are effective refractive index of waveguide and thin-film modes with wavelength. The solid curves and color shaded areas are modal loss spectra of fundamental mode excited in the ENZ fiber for four ITO shell thicknesses described above.

Chapter 3 Photonic Crystal Fiber Metalens

In this chapter, we investigate the optical fiber metalens with engineerable focal length by directly patterning a plasmonic metasurface at the end facet of the large mode area photonic crystal fiber via focus ion beam milling. The phase profiles of metalens are implemented by geometric (Pancharatnam-Berry) phase in design. We experimentally characterized the performance of the fabricated metalens such as focal length (28 μm and 40 μm), full width at half maximum (2.40 μm and 3.65 μm) and operating efficiency (~16%). Main results in this chapter were published in Nanophotonics 8(3), pp. 443-449 (2019) by the author of this dissertation [*84*].

3.1 Background

As mentioned in Chapter 1, the optical properties of the fiber waveguide cannot be altered after the fiber drawing fabrication. In addition, the spot size of the transmitted light is divergent and restricted by the diffraction limit of the dielectric core. Attempts have been made to fabricate periodical plasmonic nanostructures (*i.e.,* slits, holes, bars, *etc.*) on the optical fiber facets to alter the optical properties and to extend the functionalities of the fibers, as elements of these plasmonic nanostructures can interact directly with well-guided optical modes of the optical fiber. Compact optical fiber components such as diffraction grating [*85, 86*], amplifier [*87*], nanotrimmer [*88*], optical tweezer [*89*] and plasmonic sensors [*90-92*] have been realized with periodical nanostructures on facets of the optical fibers. A method to apply a metallic structure to a polymeric membrane on the facet of a hollow core optical fiber has been functionalized as a nano plasmonic filter [*93*]. Realization of an in-fiber focusing lens via plasmonic nanostructures has also been studied in recent

years [*94-96*]. However, these in-fiber plasmonic lenses with concentric annular slits suffer from relatively short focal length (< 10 μm), narrow operation bandwidth, and sideband caused by high order diffraction, thus limiting their potential practical applications.

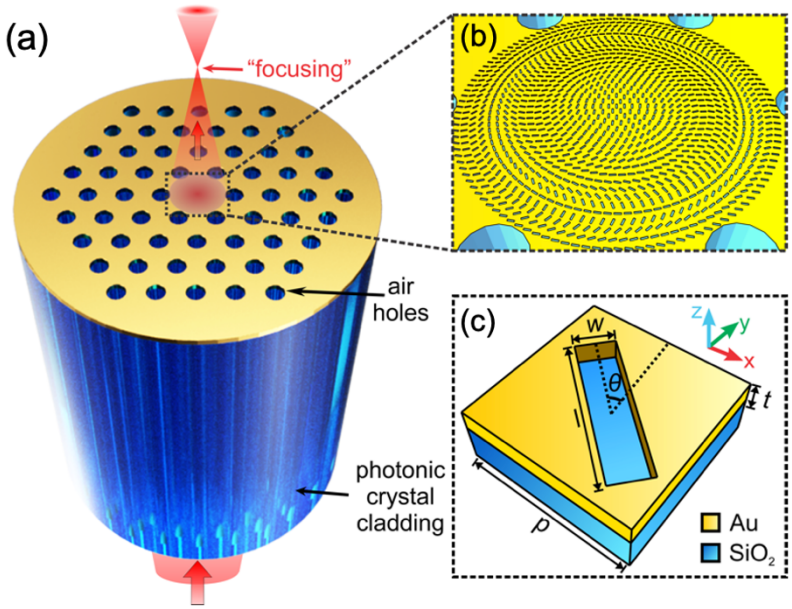

Figure 3-1 Photonic crystal fiber metalens. (a, b) Schematics of in-fiber metalens on large mode area photonic crystal fiber (LMA-PCF) and **(c)** unit element of PCF metalens.

The emergence of metasurfaces provides the opportunity to tailor light properties for advanced light manipulation and to develop novel ultrathin optical devices [*9, 10, 97*]. By producing a specific phase profile using spatially varied nano-antenna elements, metasurfaces can control the wavefront of the transmitted, reflected, scattered light, and enable novel ultrathin optical components such as metalens [*98-101*]. With the ability to control the optical phase via metasurfaces, several in-fiber metasurface optical components [*102*] have been demonstrated, for instance, an in-fiber modulator [*9, 10, 97*], linear polarizer [*9, 10, 97*] and an in-fiber beam element [*103*]. However, to date, no direct integration of metasurface-based lens onto the optical fiber has been demonstrated without relying on a

prism or flat substrates.

In this work, we developed the first optical fiber metalens with engineerable focal length by directly patterning a geometric phase (*i.e.,* Berry phase) altering metasurface onto the end facet of the large mode area photonic crystal fiber (LMA-PCF). To integrate the sufficient area and phase profile of the metalens, instead of using conventional single-mode step index fiber, an LMA-PCF was employed as the platform to guide the light in large core diameter while maintaining the single mode property (endlessly single mode) via the modified total internal reflection mechanism. We experimentally demonstrated that the circularly polarized incident beam can be focused after exiting the fiber in the telecommunication wavelength regime with considerable focusing efficiency. Our work shows a first proof-of-principle demonstration for developing an efficient in-fiber metalens.

3.2 Design and fabrication

The required distribution of phase retardation for a metalens typically follows

$$\varphi(r,\lambda) = -\frac{2\pi}{\lambda}\left(\sqrt{r^2+f^2}-f\right) \tag{3-1}$$

where r is the distance from current location on the metalens to the center, f is the focal length, and λ is the operation wavelength. With such a phase profile, the incident plane wavefronts are transformed into spherical ones, which converge at the focal length. At a fixed focal length f and an operation wavelength λ, the phase modulation $\varphi\ (r, \lambda)$ can be achieved by geometric phase method of the resonant elements in the metasurfaces (Figure 3-1). The circularly-polarized light transmitted through a unit element with the rotational angle θ acquires an additional phase $\mp 2\theta$, *i.e.,* geometric phase, where the sign indicates the

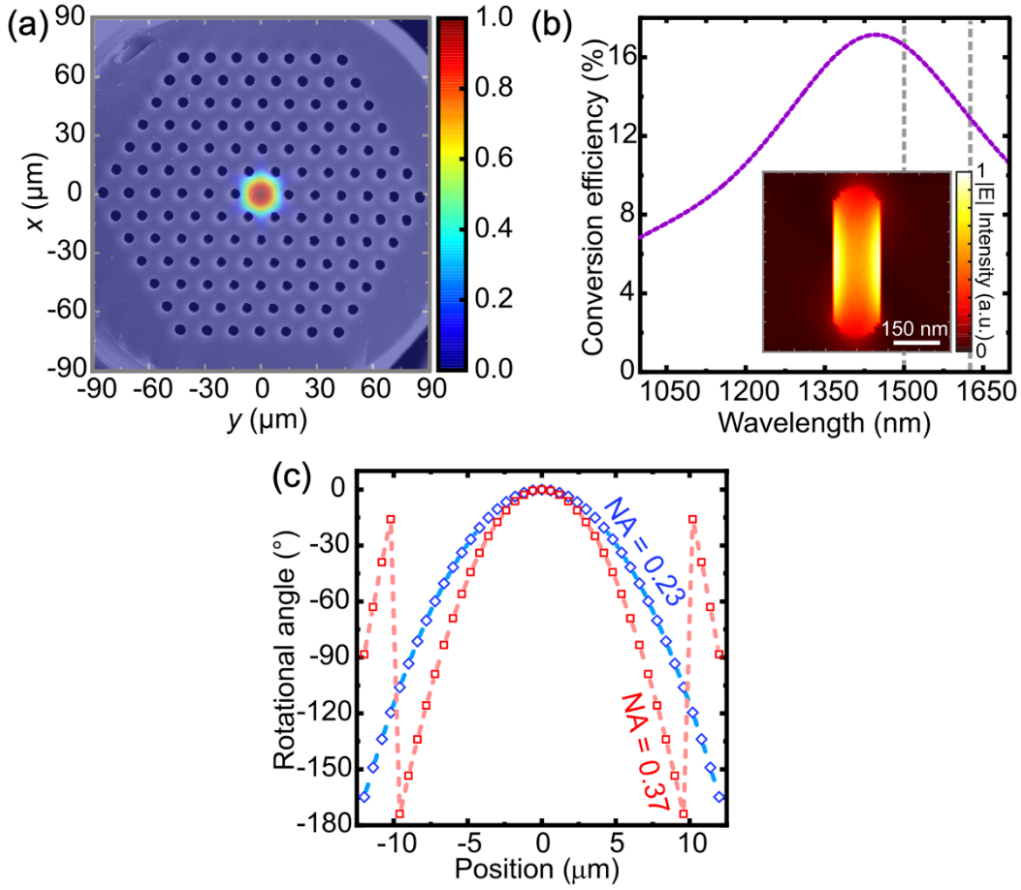

Figure 3-2 Characterization of optical fiber and designed metasurfaces. **(a)** Simulated fundamental mode profile (*i.e.,* electric field intensity distribution) superimposed with a scanning electron microscope image of the LMA-PCF. **(b)** Right-hand circular polarization (RCP) to left-hand circular polarization (LCP) efficiency of optimized unit element (l = 500 nm, w = 150 nm, p = 600 nm, t = 40 nm) in the PCF metalens in simulation. The wavelength region highlighted between grey dash lines marks the experimental bandwidth. Inset: electric field intensity distribution of the PCF metalens' optimized unit elements at corresponding resonance wavelength of 1482.6 nm. **(c)** Required rotational angles θ of unit element along the fiber core for PCF metalens for NA of 0.37 (designed focal length of 30 μm) and 0.23 (designed focal length of 50 μm) at the wavelength of 1550 nm.

handedness of circularly-polarized incidence [*104*]. Our metalens is designed on large mode area photonic crystal fiber (LMA-25), which is made of pure silica with core diameter of 25±1 μm (Figure 3-1a and 1b). Compared to conventional single mode fiber (SMF-28) with core diameter of 8.2 μm, the larger core area of PCF allows more unit elements (total 1261) to be

fabricated on the core thus providing the essential phase profile for achieving focusing functionality than conventional single mode fiber. Simulations of the large mode area photonic crystal fiber were carried out using the MODE Solutions software from Lumerical, Inc. The pitch and hole diameters of large mode area photonic crystal fiber (LMA-25, NKT Photonics, Inc.) are 16.4 μm and 4 μm, respectively. The material of the photonic crystal fiber used is pure silica glass. The simulated fundamental mode profile (*i.e.,* electric field distribution) of the LMA-PCF is shown in Figure 3-2a. Endlessly single mode guiding is maintained in the LMA-PCF with broad wavelength range, and the light is confined mostly within the core region [*105, 106*]. The designed metalens is the same size as the core to ensure that the guided core mode interacts with the entire metasurface. With the dimension of the LMA-PCF, we performed theoretical simulations to determine the required rotational angle of each individual resonant element with respect to the center to achieve the convergent effect for certain circularly polarized incident light. A single etched gold nanorod was considered as a unit element. Simulated intensity distributions of the metalens were calculated using Computer Simulation Technology (CST Microwave Studio). For the design of unit elements, a unit cell boundary condition is employed for the simulation of transmission spectra in an array configuration (see Table 3-1 for details of the structural parameters of the unit elements for two PCF metalenses). The permittivity function of silica is modeled with the standard Sellmeier expansion (Equation 2-1) as mentioned in Section 2.1 [*40*]. The complex frequency-dependent dielectric function of gold in the near-infrared regime is described by the Lorentz-Drude model with a damping constant 0.07 eV and a plasma frequency 8.997 eV. The simulated conversion efficiency of the optimized unit element (with length of 500 nm, width of 150 nm, periodicity of 600 nm, thickness of 40 nm)

for constructing the metalenses is shown in Figure 3-2b. Its resonant wavelength is located at 1482.6 nm with maximum efficiency of 17%. The electric field intensity distribution at resonant wavelength is shown in the inset of Figure 3-2b. The rotational angles θ of the unit elements as a function of their radial positions that are required for constructing the metalenses are shown in Figure 3-2c. The designed focal lengths are 30 μm and 50 μm with numerical apertures (NAs) of 0.37 and 0.23, respectively, at an operating wavelength of 1550 nm (see Table 3-2 for the required rotational angles for two PCF metalenses).

Table 3-1 Parameters of the metallic unit element for PCF metalenses

		Design	Fabricated metalens	
			NA = 0.23	NA = 0.37
Parameter (nm)	Length (l)	500	506*	489*
	Width (w)	150	149*	134*
	Thickness (t)	40	40*	40*
	Periodicity (p)	600	603*	602*

*Parameters measured from SEM images of the fabricated samples.

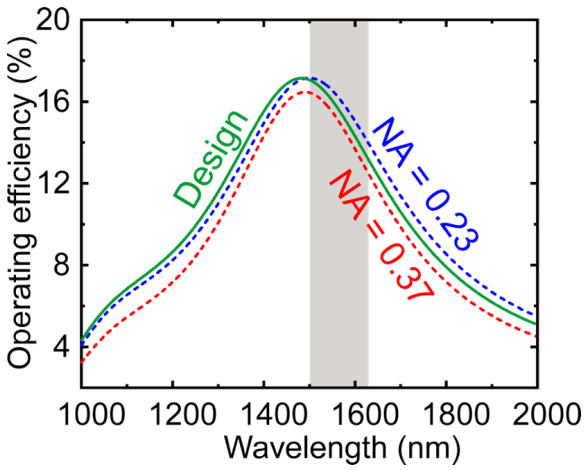

Figure 3-3 Right-hand circular polarization (RCP) to left-hand circular polarization (LCP) simulated conversion efficiency of unit elements with designed parameters (green solid curve), and actual parameters of the two fabricated PCF metalenses with NA = 0.23 (blue dashed curve) and 0.37 (red dashed curve) obtained from SEM images, respectively. The grey wavelength region highlighted the experimental bandwidth (see Table 3-1 for the structural parameters of the unit elements).

Table 3-2 Rotational angles of unit element along the radius of PCF metalenses.

Numerical aperture (NA)		0.23	0.37
Location r (μm)	Quantity	Rotational angle θ (°)	Rotational angle θ (°)
-12.0	60	-164.9	-88.4
-11.4	57	-149.0	-63.1
-10.8	54	-133.9	-38.9
-10.2	51	-119.6	-15.9
-9.6	48	-106.1	-174.0
-9.0	45	-93.3	-153.4
-8.4	42	-81.4	-134.0
-7.8	39	-70.2	-115.8
-7.2	36	-59.9	-98.9
-6.6	33	-50.4	-83.3
-6.0	30	-41.7	-69.0
-5.4	27	-33.8	-56.0
-4.8	24	-26.7	-44.3
-4.2	21	-20.4	-34.0
-3.6	18	-15.0	-25.0
-3.0	15	-10.4	-17.4
-2.4	12	-6.7	-11.1
-1.8	9	-3.8	-6.3
-1.2	6	-1.7	-2.8
-0.6	3	-0.4	-0.7
0.0	1	0.0	0.0
0.6	3	-0.4	-0.7
1.2	6	-1.7	-2.8
1.8	9	-3.8	-6.3
2.4	12	-6.7	-11.1
3.0	15	-10.4	-17.4
3.6	18	-15.0	-25.0
4.2	21	-20.4	-34.0
4.8	24	-26.7	-44.3
5.4	27	-33.8	-56.0
6.0	30	-41.7	-69.0
6.6	33	-50.4	-83.3
7.2	36	-59.9	-98.9
7.8	39	-70.2	-115.8
8.4	42	-81.4	-134.0
9.0	45	-93.3	-153.4
9.6	48	-106.1	-174.0
10.2	51	-119.6	-15.9
10.8	54	-133.9	-38.9
11.4	57	-149.0	-63.1
12.0	60	-164.9	-88.4

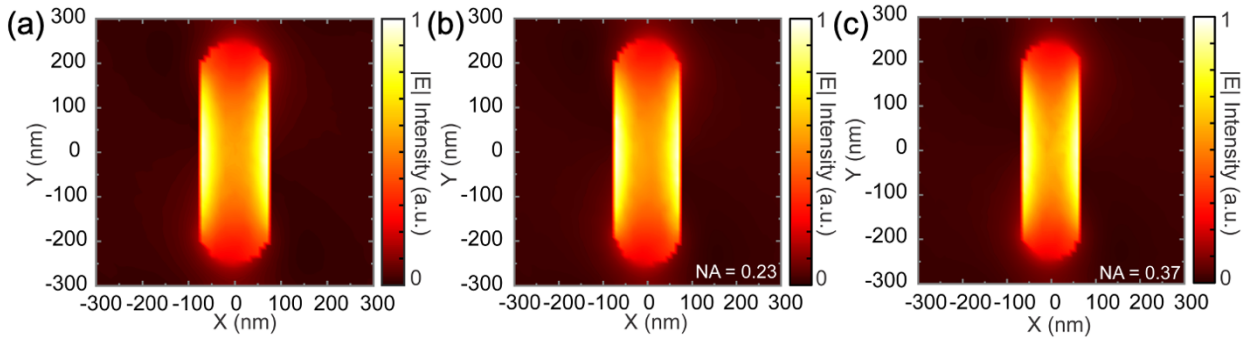

Figure 3-4 Electric field intensity distribution of the PCF metalens' unit elements for **(a)** optimized parameters and structural parameters obtained from SEM images of the fabricated samples for NAs of **(b)** 0.23 and **(c)** 0.37 at corresponding resonance wavelengths of 1482.6 nm, 1499.3 nm and 1490.3 nm, respectively (see Table 3-1 for the structural parameters of the unit elements).

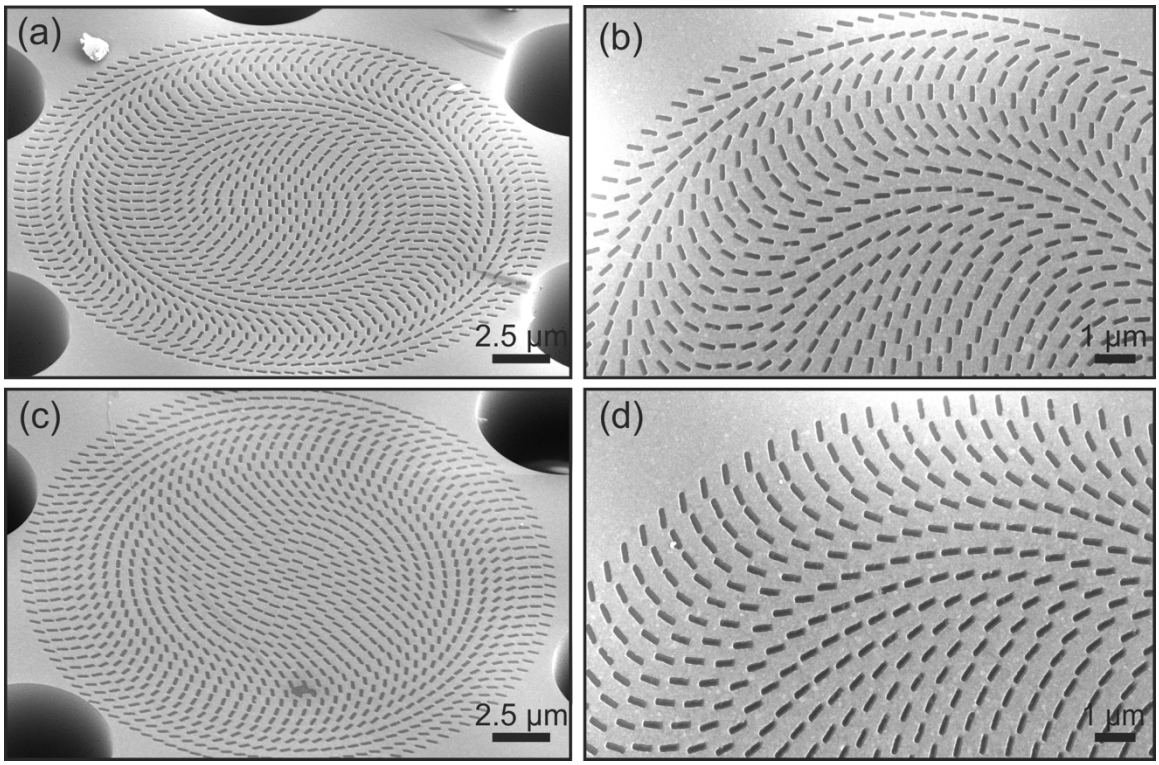

Figure 3-5 Scanning electron microscope images of fabricated PCF metalens for numerical aperture (NA) of **(a, b)** 0.37 and **(c, d)** 0.23. The core diameter of the LMA-PCF is 25±1 μm, providing the area for sufficient metasurface unit elements to ensure smooth phase distribution (see Table 3-1 for parameters of the structural parameters of the unit elements for the two LMA-PCF metalenses).

To experimentally realize the PCF metalens, we first deposited a gold layer with a thickness of 40 nm on the end facet of the LMA-PCF by magneton sputtering. The metalens pattern was fabricated by focused ion beam (FIB) milling with acceleration voltage of 30 kV and current of 1.5 pA. Special care was taken to align the center of the fiber such that the metasurface pattern completely covered the core of the fiber. The scanning electron microscope (SEM) images of the fabricated PCF metalens are depicted in Figure 3-5 (Figure 3-5a and 5b: NA = 0.37, Figure 3-5c and 5d: NA = 0.23). The simulated transmissions of the fabricated samples using the dimensions obtained in SEM show that the resonant wavelengths are located at 1499.3 nm and 1490.3 nm with maximum efficiencies of 17% and 16.5% for metalens with NA of 0.37 and 0.23 respectively (see Table 3-1 for the experimental structural parameters, Figure 3-3 for the simulated transmission of unit cells, and Figure 3-4 for the electric field intensity distributions of the corresponding elements).

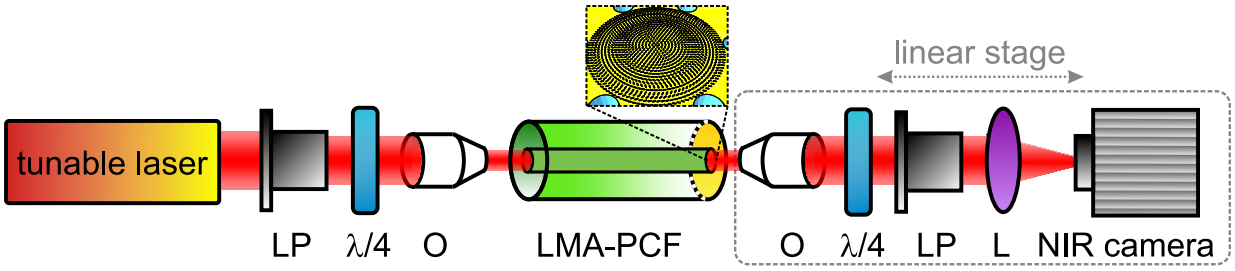

Figure 3-6 Schematics for the experimental setup for characterizing PCF metalens performance (LP: linear polarizer, $\lambda/4$: quarter-wave plate, O: objective, L: lens, NIR camera: near-infrared camera).

3.3 Results and discussion

To verify the focusing effect of the in-fiber metalens, we captured the light intensity distributions by imaging the field intensity along the light propagation direction with a *z*-scan setup. Light from a tunable laser (wavelength range: 1500-1630 nm, Santac TSL-550) is launched through a linear polarizer and a quarter-wave plate to generate a circularly

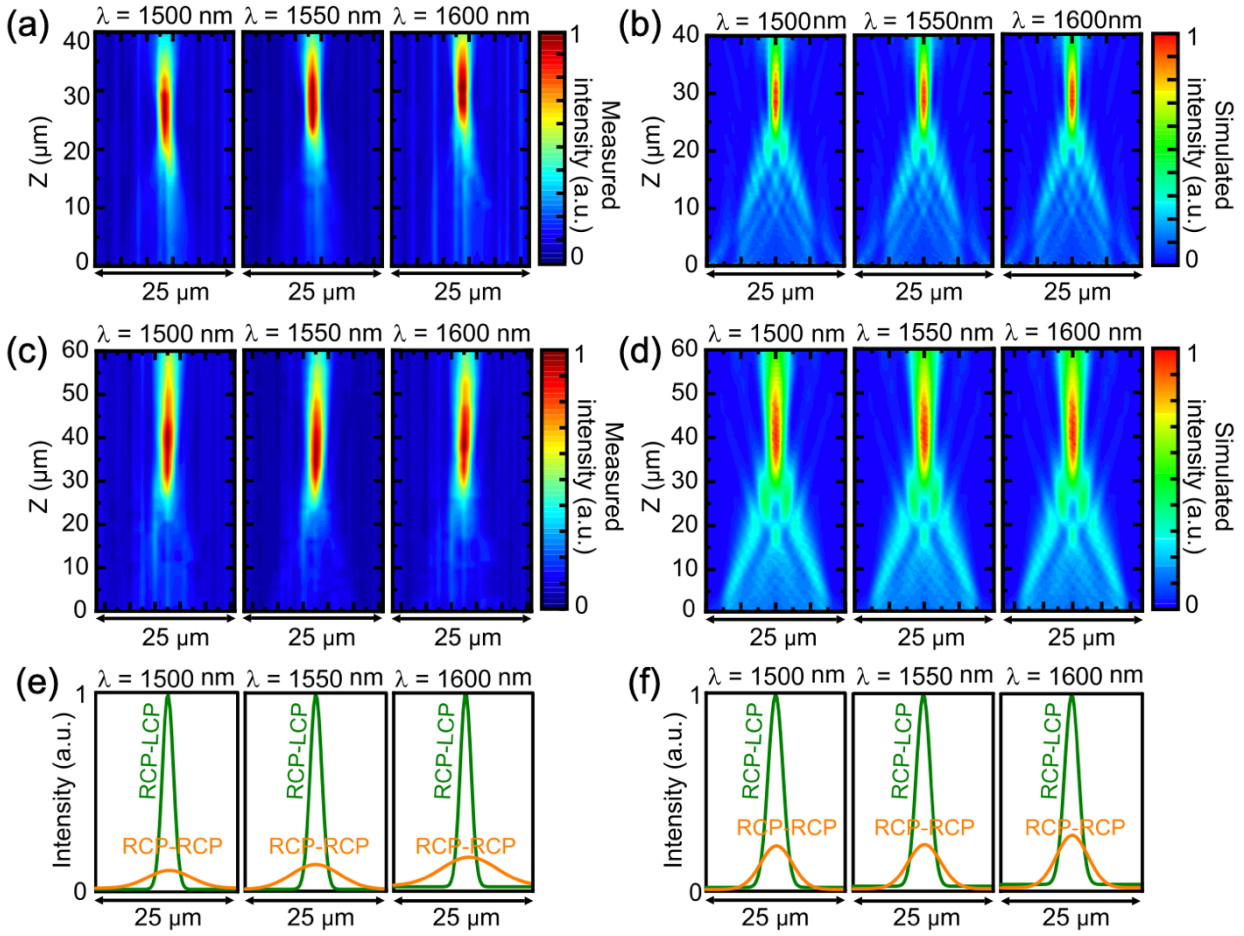

Figure 3-7 Intensity distributions of PCF metalenses. Measured intensity and simulated intensity profiles of PCF metalenses with **(a, b)** NA = 0.37 and **(c, d)** NA = 0.23 along the light propagation direction at various incident wavelengths. Experimental intensity distributions of each mode at corresponding focal planes for RCP-LCP and RCP-RCP (input-output) combinations of the PCF metalens with NA of **(e)** 0.37 and **(f)** 0.23 at different wavelengths.

polarized beam as shown in Figure 3-6. The beam is then focused by an objective lens (40× magnification, NA = 0.65) into the LMA-PCF with the metalens fabricated on the output end facet of the fiber. At the output end, an objective (40× magnification, NA = 0.65), quarter-wave plate, linear polarizer, tube lens and near-infrared (NIR) camera (Xenics, XEVA 6816) are assembled on a linear translation stage to image the right-hand or left-hand circular polarized output component of the light transmitted through the PCF metalens. To obtain

the axial light intensity distribution in Figure 3-7 of the main text, the collecting objective initially focuses on the end-face of the PCF metalens (z = 0 μm position in Figure 3-7) and then the focal plane of the objective scans along the converging beam from the metalens to determine its focal length. Images are taken with a step size of 1.33 μm with typical total moving distance of 50 μm to 60 μm. Using the designed geometric phase based metalenses, the incident right-hand circular polarized (RCP) light was launched into the PCF metalens, and the left-hand circular polarization (LCP) component was collected as output light. The stitching field intensity profiles on the x-z plane for these two PCF metalenses at wavelengths from 1500 nm to 1600 nm with a step of 50 nm are shown in Figure 3-7a and 7c. The light density increases as the distance increases from the end facet of the PCF metalens to the focal plane, thus demonstrating the focusing effect. The observed focal lengths are 30 μm and 40 μm, respectively. The measured light distributions show good agreement with the output intensities of the LCP components obtained from the simulation (Figure 3-7b and 7d). For simplicity, cylindrical lenses are simulated to numerically-predicate the focal length of the designed metalens, where perfect matched layer (PML) and periodic boundary conditions were employed in the x and y directions, respectively. The simulated dimension of the metalens in the x direction is set to 25 μm which is the actual core diameter of the LMA-PCF. The actual size parameters of the unit elements obtained from SEM images of two PCF metalenses are utilized in the simulation (see Figure 3-8 and Figure 3-9 for more experimental and simulated light intensity distributions of PCF metalenses with NA of 0.37 and 0.23 from operation wavelength of 1500 nm to 1630 nm with a step of 10 nm).

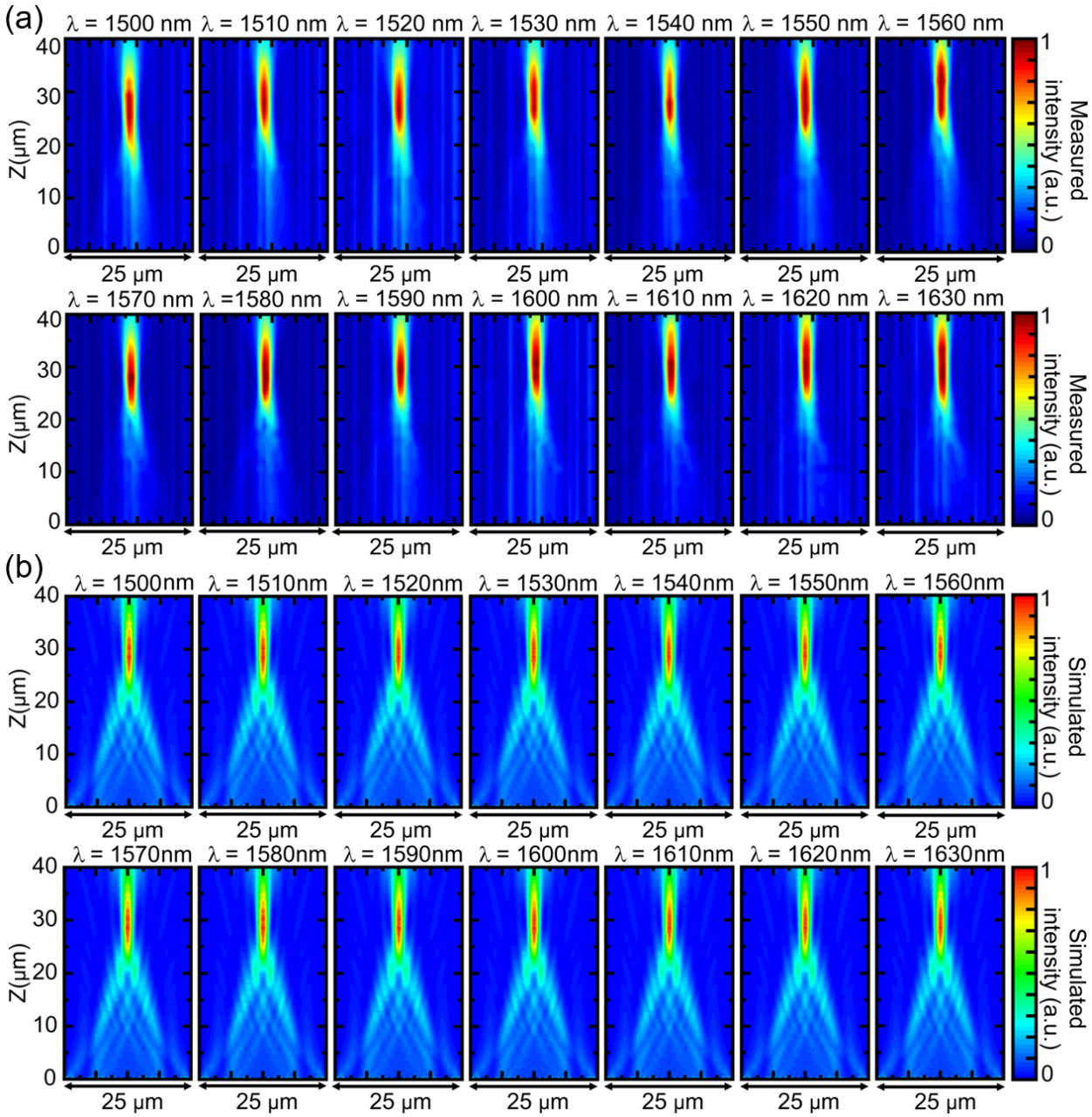

Figure 3-8 Experimental **(a)** and simulated **(b)** intensity distribution profiles of PCF metalens with numerical aperture of 0.37 (measured focal length of ~30 μm) along the light propagation direction at different wavelengths.

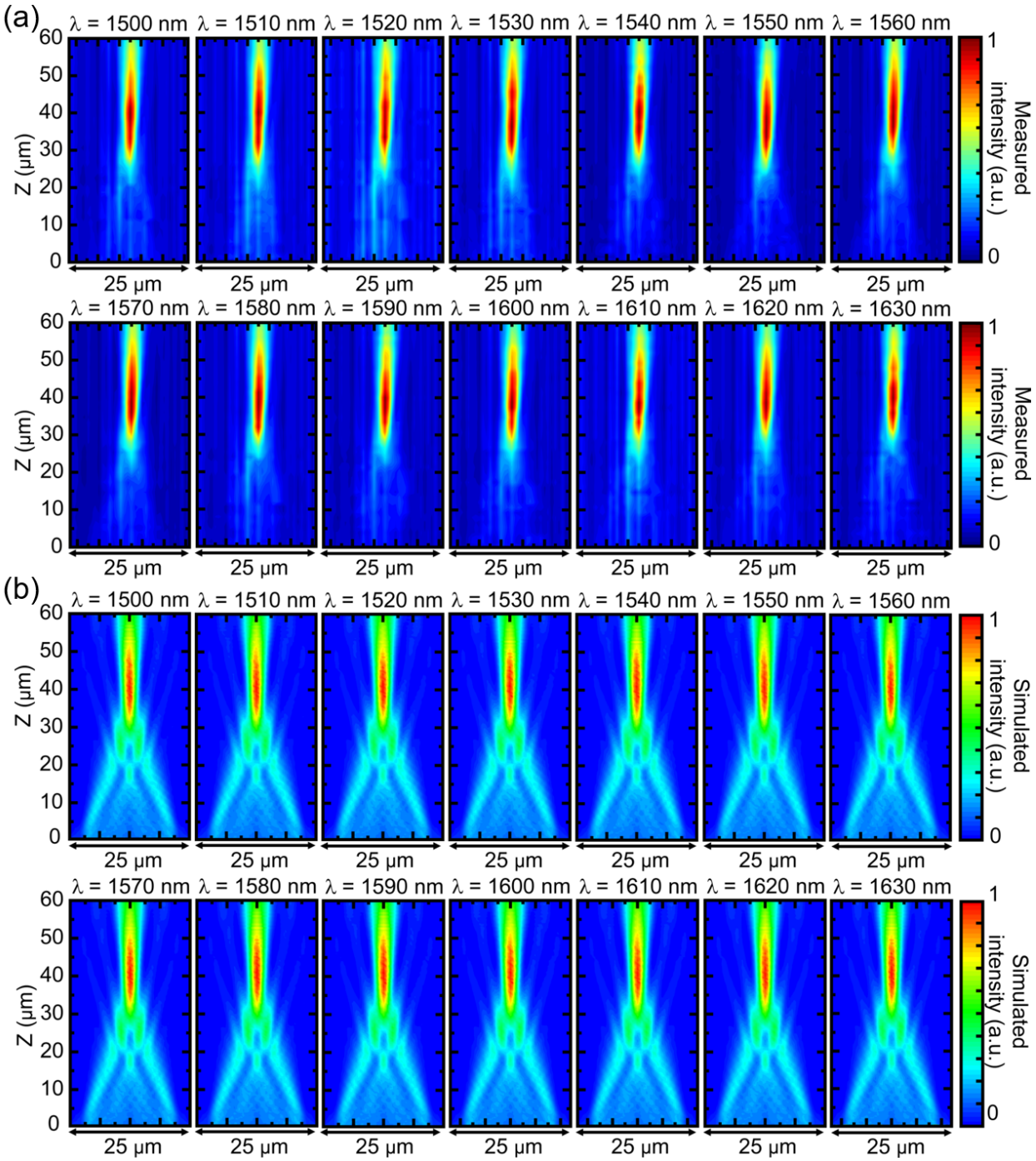

Figure 3-9 Experimental **(a)** and simulated **(b)** intensity distribution profiles of PCF metalens with numerical aperture of 0.23 (measured focal length of ~40 μm) along light propagation direction at different wavelengths.

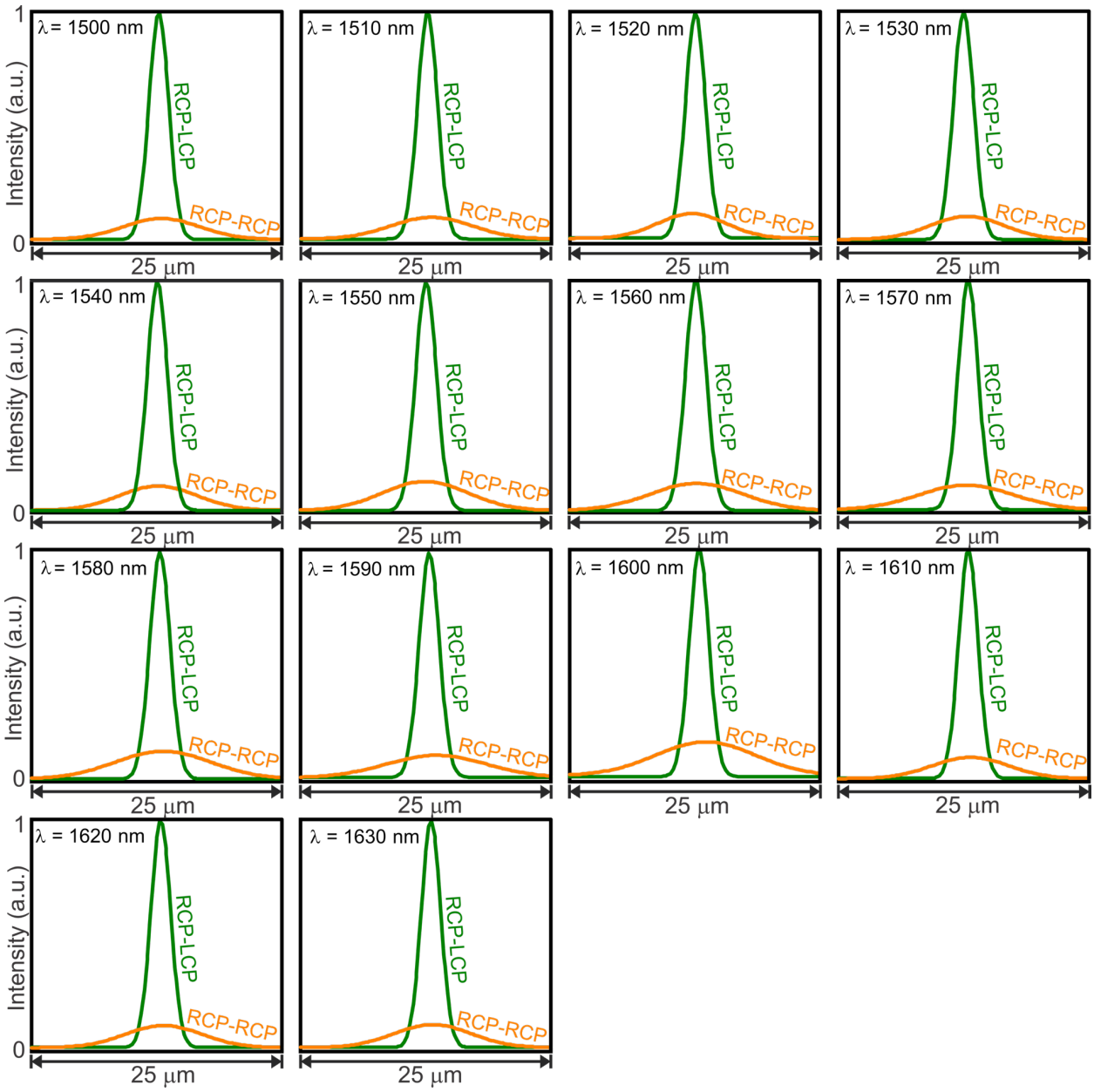

Figure 3-10 Experimental intensity distributions at corresponding focal plane for RCP-LCP and RCP-RCP input/output combination of the PCF metalens with numerical aperture of 0.37 at different wavelengths.

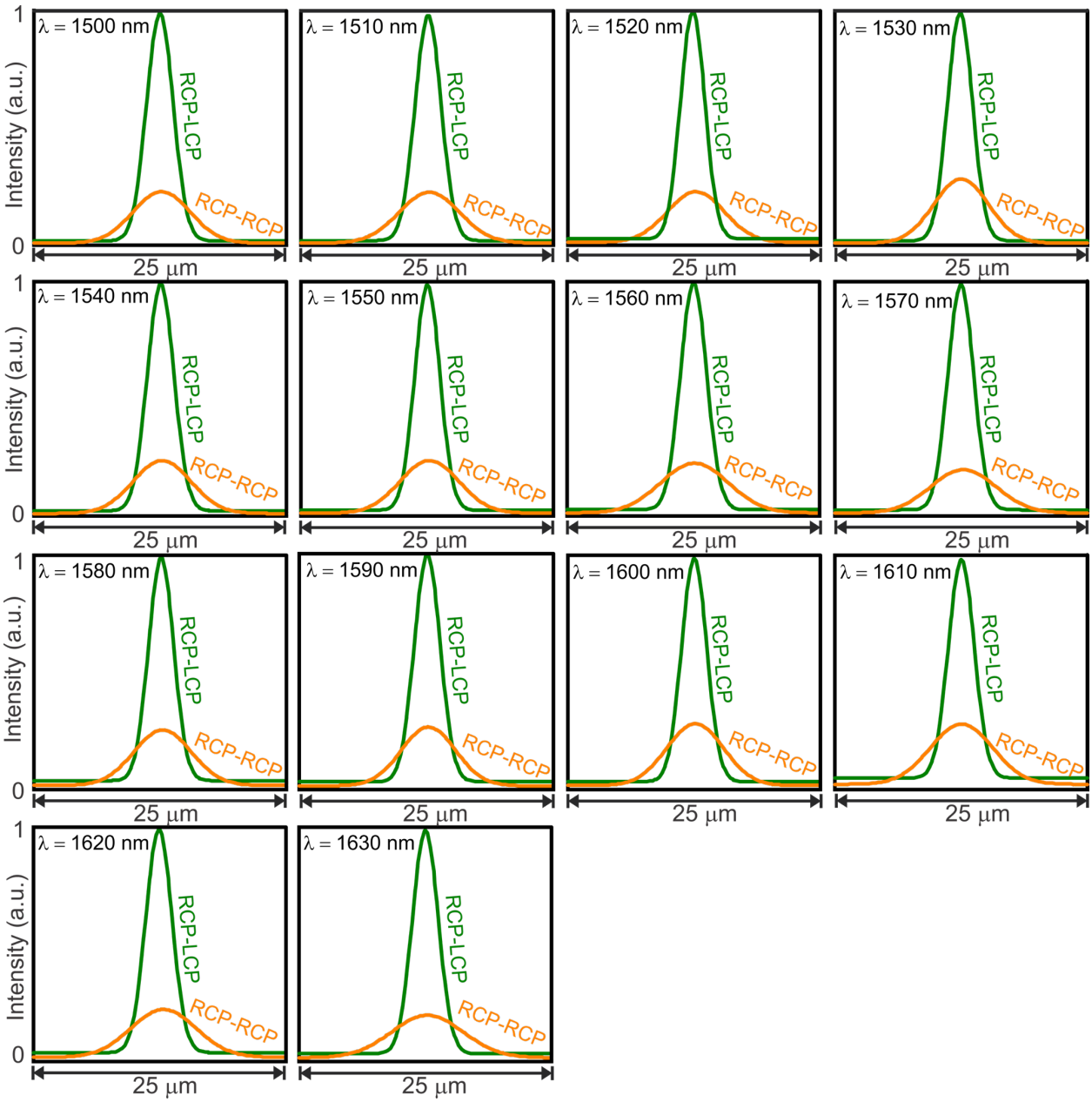

Figure 3-11 Experimental intensity distributions of each mode at corresponding focal planes for RCP-LCP and RCP-RCP input/output combinations of the PCF metalens with numerical aperture of 0.23 at different wavelengths.

To confirm the focusing effect from the metasurfaces, the RCP components from the output were collected in the same way as LCP components. We extracted mode intensity distributions along the core diameter from NIR camera images for two PCF metalenses correspondingly. The mode intensities were fitted by Gaussian function and normalized to the maximum mode intensity of RCP-LCP at corresponding operation wavelengths. The mode intensity distributions of both the RCP-LCP and RCP-RCP input-output combinations at corresponding focal planes for two metalenses at 1500 nm, 1550 nm and 1600 nm were recorded and depicted in Figure 3-7e and 7f, respectively. It is clear from the figure that focusing effect of the metalens is observed only for the input-output combination of RCP-LCP. The slight amount of light measured in the RCP-RCP combination is attributed to the imperfect fabrication of the input and output polarizers and the unmaintained RCP light within the PCF (see Figure 3-10 and Figure 3-11 for more experimental mode intensity distributions of PCF metalenses with NA of 0.37 and 0.23 for operation wavelength from 1500 nm to 1630 nm with a step of 10 nm). No focusing was observed from the RCP output component, which is consistent with the theoretical design of the Berry phase based metalens [*15, 99, 107, 108*]. The measured intensity distributions along the diameter of the beam at the focal planes of two PCF metalenses for the RCP input to LCP output combination at the wavelength of 1550 nm are depicted in Figure 3-12. The mode intensity distribution of LMA-PCF without the fabricated metalens is collected (focused on the end facet) for RCP input to RCP output at wavelength of 1550 nm as reference. The experimental mode intensities were fitted by Gaussian function and then normalized to the corresponding maximum of each mode intensity distributions.

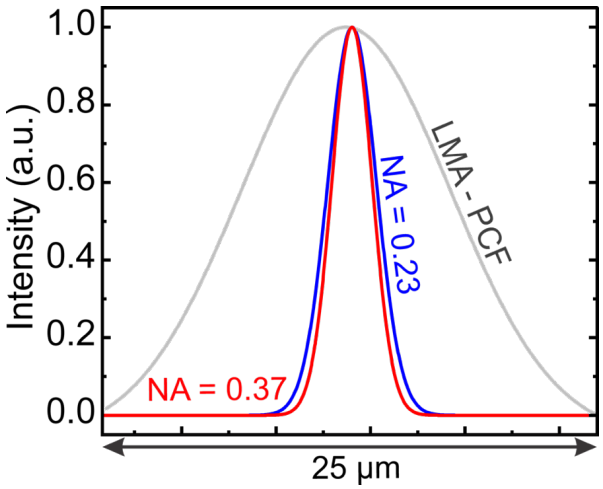

Figure 3-12 Mode profiles at the focal planes of PCF metalenses with numerical apertures of 0.37 and 0.23 in comparison with the mode profile of LMA-PCF without metalens at the operation wavelength of 1550 nm.

We further analyzed the optical performance of metalenses. Figure 3-13a shows the analysis of the dependence of focal lengths on the wavelength and full width at half-maximum (FWHM) of the focal spot. For the PCF metalens with NA of 0.37, the measured focal lengths varied from 26.7 μm to 28.0 μm between wavelengths of 1500-1630 nm, which are in good agreement with the simulated results (*i.e.,* focal length of 28.5 μm within the same wavelength range). For the metalens with NA of 0.23, the experimental focal lengths are varied from 40.0 μm to 41.3 μm between operation wavelengths of 1500-1630 nm, closely resembling the simulated results of 40.0 μm to 41.0 μm. However, this focal length shows larger offset from the theoretical calculation (*i.e.,* the designed focal length of 50 μm), which is mainly from the implemented phase distribution only divided in the first Fresnel zone. This can be effectively addressed by either increasing the core size or the numerical aperture of metalens. The measured and simulated focal lengths at wavelength of 1550 nm are 28.0 μm and 40.0 μm for the two PCF metalenses, which are close to our design. The FWHM is defined as the beam waist of half maximum light intensity, which is obtained by fitting the

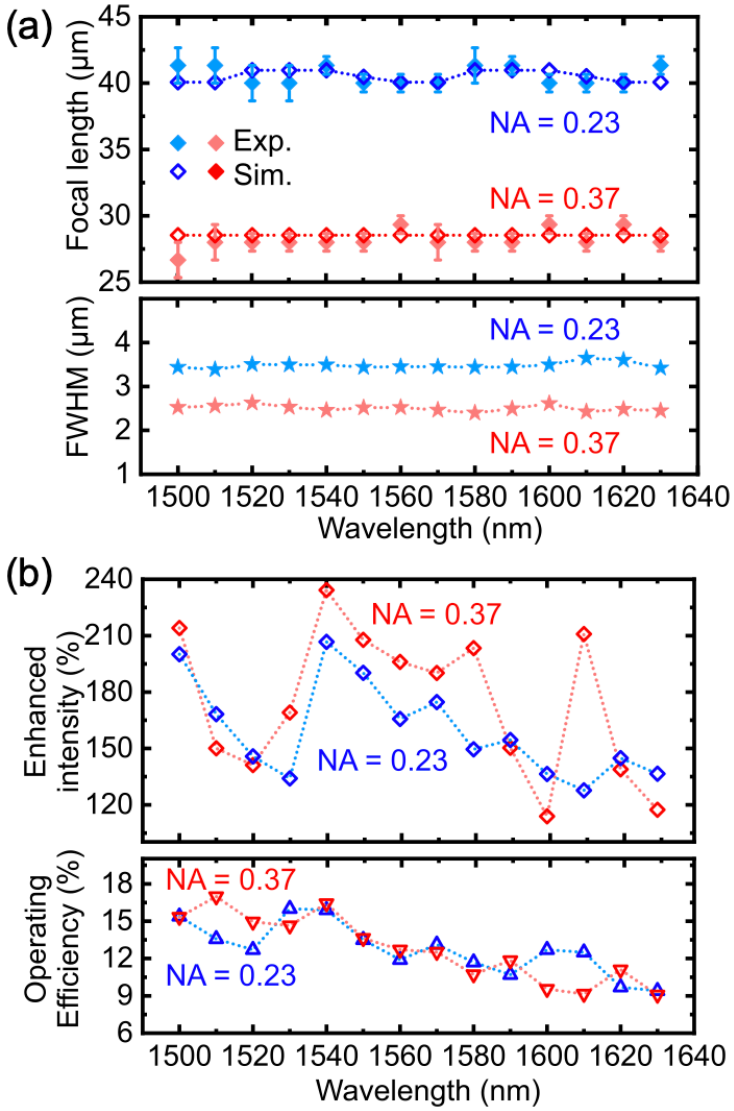

Figure 3-13 Characteristics of PCF metalenses. **(a)** Measured, simulated focal lengths and full width at half maximum (FWHM), **(b)** operating efficiency and enhanced optical intensity of PCF metalenses with NA = 0.23 and NA = 0.37 at corresponding focal plane versus wavelength.

measured cross section of light intensity at the focal spot with the Gaussian function. The FWHM are 2.40-2.63 μm and 3.44-3.65 μm in the measured wavelength range for the PCF metalens with NA of 0.37 and 0.23, respectively (see Figure 3-12 for comparison of spot sizes between two PCF metalenses and LMA-PCF without gold metalens).

The operating efficiency and enhanced optical intensity of the PCF metalenses are

shown in Figure 3-13b. The operating efficiency (*i.e.,* the focusing efficiency from incident RCP to output LCP) is defined as the ratio of the light intensity of the mode profile at the focal spot to the light intensity right in front of the end face of a reference PCF without a gold coating. The maximum efficiencies of 16.1% and 16.4% were measured for these two PCF metalenses at wavelengths of 1530 nm and 1540 nm, respectively. The decrease of the operation efficiency with wavelength is in accordance with simulated RCP to LCP conversion efficiency from the unit element (Figure 3-2b). It should be noted that the operation efficiency can be further enhanced by optimizing the configuration or employing dielectric metasurfaces [*97, 109*]. Operation efficiency as high as 91% could be obtained with optimized parameters of silicon nano-antennas. Silicon nano-antennae are proposed as unit elements of the PCF metalens to improve the operation efficiency of PCF metalens. To demonstrate the enhanced efficiency, we consider a silicon positive nano-antenna as a unit element on SiO_2 substrate (Figure 3-14a). The dimensions of the unit cell optimized for 1550 nm operation wavelength are shown in the figure (in unit of nanometer). The conversion efficiency of the optimized unit element is then calculated and depicted in Figure 3-14b. The operation efficiency of 91% is obtained at operation wavelength of 1550 nm. The magnetic field distribution of the optimized unit element at wavelength of 1550 nm is shown in Figure 3-14c, where the waveguide-like resonance is observed. Those silicon nano-antennas could be implemented onto the fiber with similar nanofabrication techniques such as electron beam lithography, and photolithography [*88*].

We also defined the enhanced optical intensity of the PCF metalenses as the ratio of light intensity integrated over the whole beam profile at focal plane to the one right after the end-facet of the LMA-PCF without metalens (Figure 3-13b). The enhanced optical intensity

is 234% larger at the wavelength of 1540 nm. Even though the focusing performance is limited by operation efficiency, the light intensity of the PCF metalens is more intense than that of the reference fiber. The demonstrated efficient in-fiber metalens provides an engineerable NA and FWHM with enhanced optical intensity. It could enhance the development of novel and ultracompact in-fiber optical imaging, sensing and communication device applications such as in-fiber lenses [*110, 111*] for laser surgery and optical fiber endoscopes [*101*], a focusing element for optical fiber laser and spectroscopy, and an efficient fiber coupling for optical interconnects. The optical metalens could further be extended to hollow core optical fibers by integrating with a flexible membrane on the hollow core [*93*], providing a unique focusing element for a fiber gas laser. Further integration of electrically tunable materials such as transparent conducting oxide materials into the in-fiber metalens [*69, 112*] could potentially enable tuning of the focusing effect or focal length which would be significant for novel fiber optical trapping and active sensing.

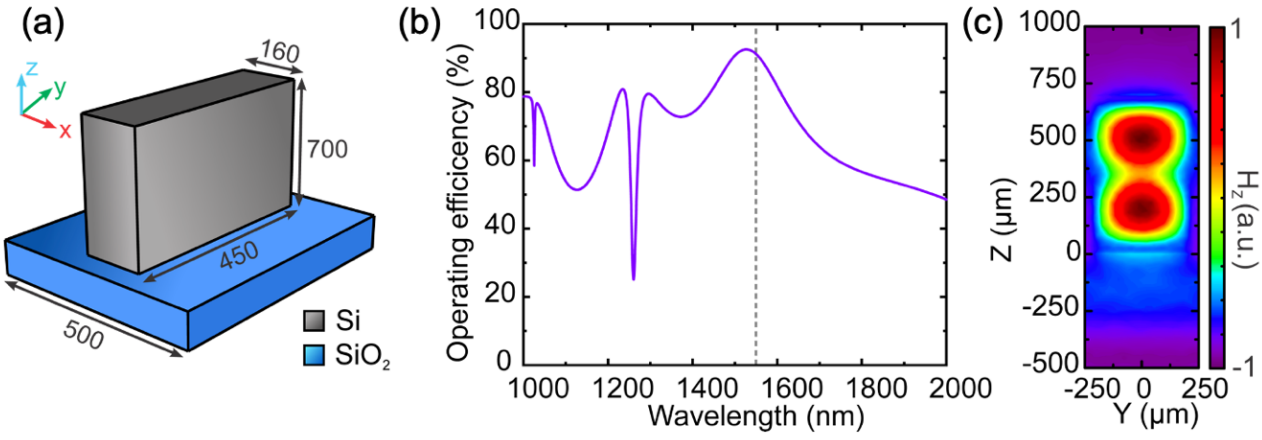

Figure 3-14 (a) Schematics (the dimensions are in nanometer) and **(b)** RCP-LCP conversion efficiency of unit element. The grey dash line indicates the wavelength of 1550 nm. **(c)** Magnetic field distribution of the optimized dielectric unit element for PCF metalens at wavelength of 1550 nm.

3.4 Summary

We experimentally demonstrated an in-fiber metalens enabled by ultrathin geometric phase metasurfaces with a thickness of 40 nm fabricated on the end-facet of a photonic crystal fiber. The ultrathin metalens provides a phase gradient and focuses light from the fiber as a refractive converging lens at telecommunication wavelengths. The focal lengths of 28 μm and 40 μm at the operating wavelength of 1550 nm were measured, providing light focusing with NA of 0.37 and 0.23, respectively. The maximum operating efficiency is 16.4%, which approaches the theoretically predicted level for flat metallic metasurfaces. The maximum enhanced optical intensity is as large as 234%. This integration of metalens and optical fiber will find applications for in-fiber optical imaging and sensing and be significant in the miniaturizing of optical fiber devices with advanced multi-functionalities. Moreover, the proposed fiber metalens has the potential to be functionalized as an active optical component with a tunable focal length and switchable convergent effect by introducing the tunable mechanisms into metasurfaces.

Chapter 4 Gate-Tunable Metasurface Optical Filter

The electromagnetic responses of the metasurfaces discussed above are fixed after fabrication. This limits dynamic manipulation of the wavefront of the incident electromagnetic wave. Therefore, it is significant to develop efficiently tunable metasurface components. In this chapter, we investigate gate-tunable optical filter based on active metasurfaces. The gate-tunable plasmonic optical filter is formed by a subwavelength patterned metasurface heterostructure. An additional thin transparent conducting oxide (TCO) layer is embedded in the insulator layer to form a double metal–oxide-semiconductor configuration. Full-wave electromagnetic simulations show that amplitude modulation and the shift of transmission peak are achievable. This chapter was published in J. Zhang, J. Yang, *et al.,* Optics Letters 44 (15), pp. 3653-3656 (2019) [*113*]. The author of this dissertation was involved in the optimization of the active metasurface heterostructures and analysis with the coworkers in the group.

4.1 Background

As discussed in Chapters 2 and 3, metasurfaces (the flat surface equivalent of metamaterials) can control light with flat optical structures less than a wavelength thick [*10, 11*]. Plasmonic metasurfaces are metallic nanostructures composed of periodic holes, slits, or resonator arrays in subwavelength scale which show distinct optical behaviors at plasmonic resonance. To date, the applications of plasmonic metasurfaces include flat lenses [*114, 115*], sensors [*116, 117*], wave plates [*118, 119*], polarizers [*120*], and color filters [*121-126*], *etc*. Among these applications, color filters have been a long-lasting focus of interest for ultracompact integrated photonic systems. However, for a given material with fixed intrinsic optical

properties, the response of the filter could not be altered once it is fabricated. Several attempts have been carried out to dynamically modulate the phase or amplitude of the transmitted/reflected light of the metasurfaces, which includes using a mechanical altering mechanism [*127*], thermal [*128, 129*], optical [*130*], and electrical stimuli [*131-134*]. However, these tunable metasurfaces require high operating power and exhibit slow response and weak modulation in amplitude.

Transparent conducting oxides provide advantages for designing various tunable plasmonic and nanophotonic devices *[52, 112, 135-140].* We discussed in Chapter 2 that by applying a relatively low electric field across the insulator-TCO-metal interface, an accumulation layer of charge carriers is formed near the interface, thus leading to a large refractive index change in the accumulation layer of the TCO for efficient optical modulation (Figure 2-10) [*141-146*]. Since the drift velocity of electrons to form the accumulation layer is fast (exceeds terahertz), with the small footprint and low capacitance of metasurfaces, the modulation speed of field-effect tunable device could exceed tens of gigahertz [*52, 75, 142, 147*]. Note that the tuning regime of accumulation layer in ITO (*i.e.,* Debye length) is typically 1-3 nm, which is difficult to provide large enough refractive index change for tunable metasurfaces. However, by judiciously designing the confined optical mode (*e.g.,* metasurface and plasmonic nanostructures) and utilizing the tunability of TCO materials, electrically tunable nanophotonic devices could be possibly realized.

In this work, we propose a novel, compact, and flat color filter based on conducting oxide metasurface heterostructure in which the light transmission can be electrically controlled. This proposed structure overcomes some of the drawbacks of tunable metasurfaces by employing TCO materials, such as low operation voltage less than 5 V and

quick response in the GHz range. The numerical simulation shows that 7.7 dB modulation of transmission can be achieved with applied 5 V bias. The modulation is near the ENZ region, where the permittivity of the ITO approaches zero. Moreover, the structure exhibits the maximum resonance shift of 35 nm under 3 V bias. This allows for the device to function as either a tunable color filter or a modulator depending on the applied bias. The scheme opens the opportunity of designing next-generation tunable, ultra-compact, and efficient wavelength selective filters.

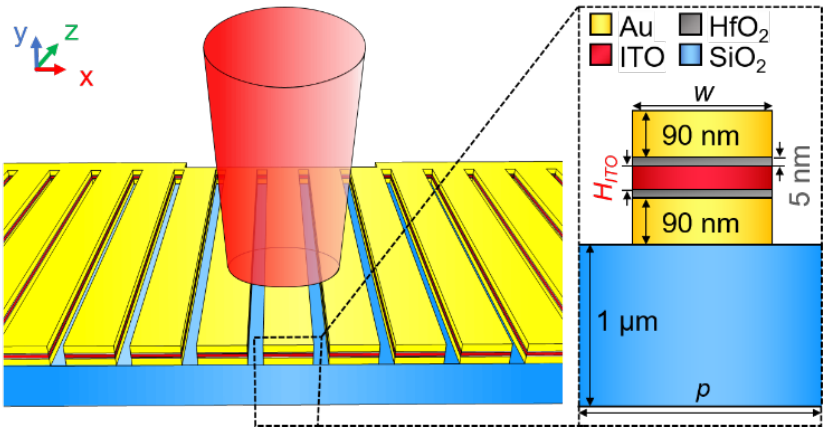

Figure 4-1 Schematic of the proposed tunable color filter. Inset: Cross-section of the unit element of the designed structure.

4.2 Principle and design

The schematic of the proposed color filter is depicted in Figure 4-1. A subwavelength nano-slit array is patterned on the top of the SiO_2 substrate with period p. The proposed structure is a modified periodic metal-insulator-metal configuration with ultrathin layers of indium tin oxide (ITO) and hafnium dioxide (HfO_2) sandwiched between two gold nanostrips. The thicknesses of Au and HfO_2 layers are 90 nm and 5 nm, respectively. The thickness of the ITO (H_{ITO}) is designed from 20 nm to 100 nm. This structure could be potentially fabricated

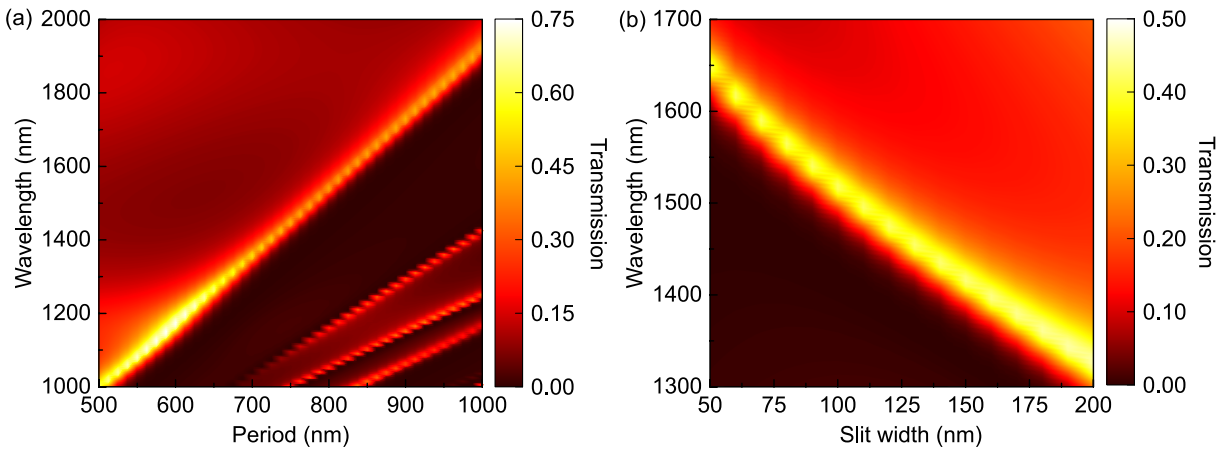

Figure 4-2 Transmission properties of the optical filters with varying geometric factors. **(a)** Map of transmission spectra with varying period *p*. The slit width is kept constant as 90 nm. **(b)** Map of transmission spectra for varying slit width *s*. The period is kept constant as 800 nm.

using standard electron beam lithography and lift-off or etching processes or advanced helium focused ion beam milling technique with features of < 100 nm with good sidewall properties and fabrication uncertainty of ~5 nm. In this design, the insulting HfO_2 layer allows a voltage bias up to 5 V without electrical breakdown [*148*]. When applied biased, the ITO layer changes its optical property due to the formation of an electron accumulation layer at the ITO-HfO_2 interface and hence changing the resonant properties of the structure. Here, the refractive index of SiO_2 is modeled with the standard Sellmeier expansion in Equation 2-1 (Section 2.1) [*40*] whereas that of Au and HfO_2 are taken from experimental data [*149*].

4.3 Simulation and discussion

We numerically studied the optical response of the color filter using the finite element method (COMSOL Multiphysics). To study the dependence of the transmission peak on the structural parameters, we performed parametric sweeps on the period and width of the nanostrip. The ITO layer thickness HITO was fixed at 30 nm, and the slit width was defined

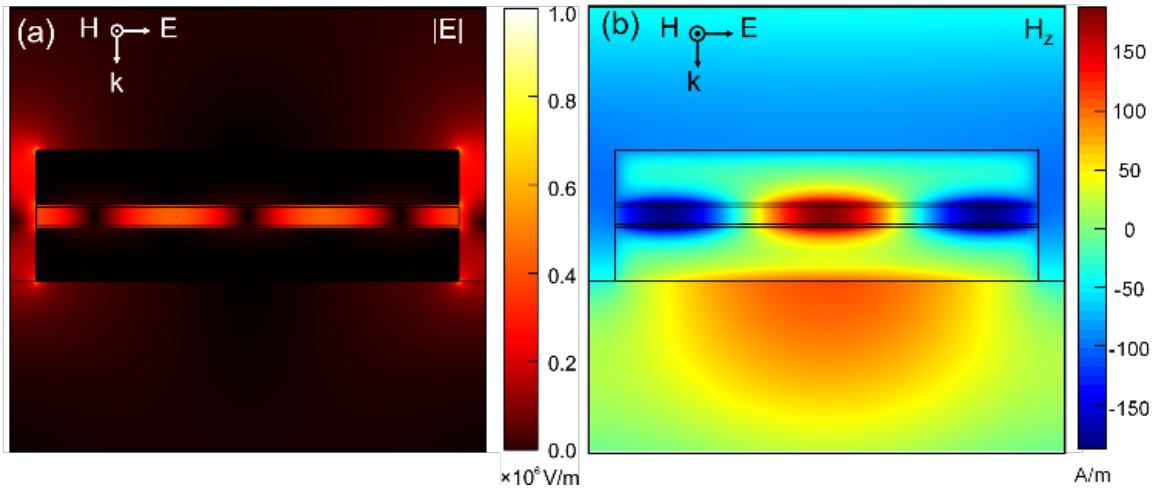

Figure 4-3 (a) Electric field distribution and **(b)** Real part of z-component magnetic field distribution for a filter structure with p = 800 nm, s = 90 nm, and TM polarization incidence light at the wavelength of 1540 nm.

as $s = p - w$. The incident light is transverse magnetic (TM) polarization with the electric field polarized parallel to the x-axis in Figure 4-1. The wavelength-dependent transmission properties of the color filter varied with the period (p: 500 nm-1000 nm) and fixed slit width (s = 90 nm) as shown in Figure 4-2a. There is a decrease in the cavity width increases transmission efficiency. In Figure 4-2b, the scanning is conducted by increasing the slit width from 50 nm to 200 nm but keeping period as 800 nm. We can see that the transmission peak redshifts linearly as the period increases or slit width decreases. Also, the bandwidth of the resonant peak slightly narrows down as the slit width decreases. Since the plasmonic resonance condition is directly related to the period and the slit width of the nanostrip array, by carefully selecting the geometric factors of the nanostrip array (period and slit width), a desired transmission peak position and efficiency can be achieved [*150*]. A tradeoff between transmission efficiency and transmission peak bandwidth should be considered in the practical structure design. Since operating wavelength we are interested in is

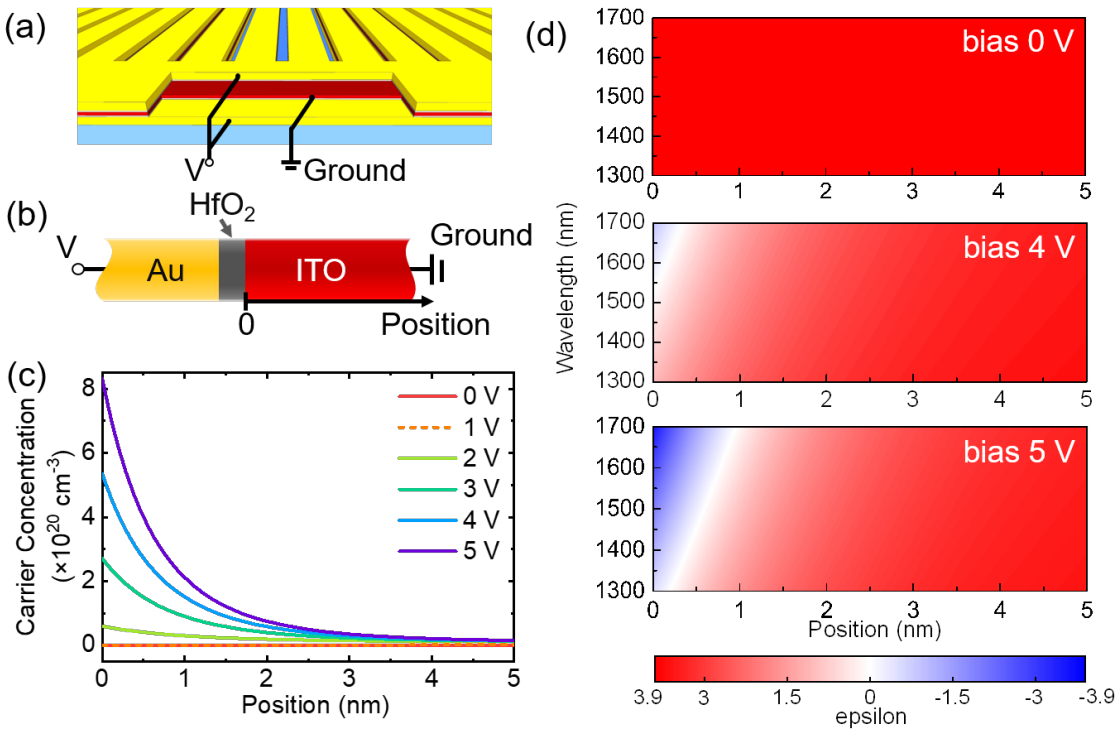

Figure 4-4 (a) Configuration for field-effect modulation for the proposed structure. **(b)** Metal-oxide-TCO structure used to simulate the electric and optical properties of the ITO accumulation layer. **(c)** Simulated carrier concentration distribution of the ITO layer at the first 5 nm from the ITO-HfO_2 interface. **(d)** Real part permittivity distribution of the ITO as a function of wavelength for 0 V **(top)**, 4 V **(middle)**, and 5 V **(bottom)**. The permittivity is calculated with a standard Drude model for the ITO.

telecommunication band, the period and silt of the nanostrip arrays will be kept as 800 nm and 710 nm, respectively. So, the configured filter provides a transmission peak at the wavelength of 1540 nm. Figure 4-3 depicts the electric field profile and the real part of the *z*-component magnetic field profile of the color filter at a peak wavelength of 1540 nm. The electric field distribution |E| shows a superposition of E_x and E_y, forming a current loop inside the metal-insulator-metal layer (Figure 4-3a) and thereby denotes the character of the magnetic resonance, which is reconfirmed in Figure 4-3b by the strong confinement of the magnetic field in the gap region between the two gold strips. Due to the high confinement of

the plasmonic resonance, modifying the material in the gap region could result in a strong change of the transmission properties.

Integration of TCO material (ITO) into the metal-insulator-metal filter provides such tunability via field-effect. To determine the characteristics of these tunable properties, we first simulate the carrier concentrations and charge profiles of the ITO with different gating voltages (Figure 4-4a and 4b). Identical biases were applied to the top and bottom gold strips, and the ITO layer was grounded. Numerical simulations of the electron concentration distributions were carried out using electronic solver (DEVICE Suite, Lumerical Inc.) [*40*]. The device simulator uses finite element method to solve the Poisson and drift-diffusion equations. In our electronic simulations, we used a self-adaptive mesh generation algorithm with a maximum of 20,000 refinement steps and a minimum mesh size of 5×10^{-4} nm. The frequency-dependent ITO permittivity $\varepsilon_{ITO}(\omega)$ can be described with the Drude model in Equations 2-11. The plasma frequency relates to the carrier concentration N, effective electron mass m^*, and electron charge e. The values of the parameters are $\varepsilon_\infty = 3.9$, $\Gamma = 2\times10^{14}$ rad/s, and $m^* = 0.28 \times m_0$ where m_0 is electron rest mass [*151*]. The initial carrier concentration for the ITO layer used in simulations is 1×10^{19} cm^{-3} which is dielectric without ENZ properties at the wavelength of 1540 nm.

By applying a positive bias to the gold layers and ground to the ITO layer, an accumulation layer of electrons is formed at both of HfO_2-ITO interfaces, thus changing the carrier distributions. Figure 4-4c shows the corresponding carrier concentration N versus the position from the HfO_2-ITO interfaces under various biases. The spatial distribution of the real part of ITO permittivity versus wavelength for different applied voltages is shown in Figure 4-4d. Without the applied voltage, the permittivity near the HfO_2-ITO interface is

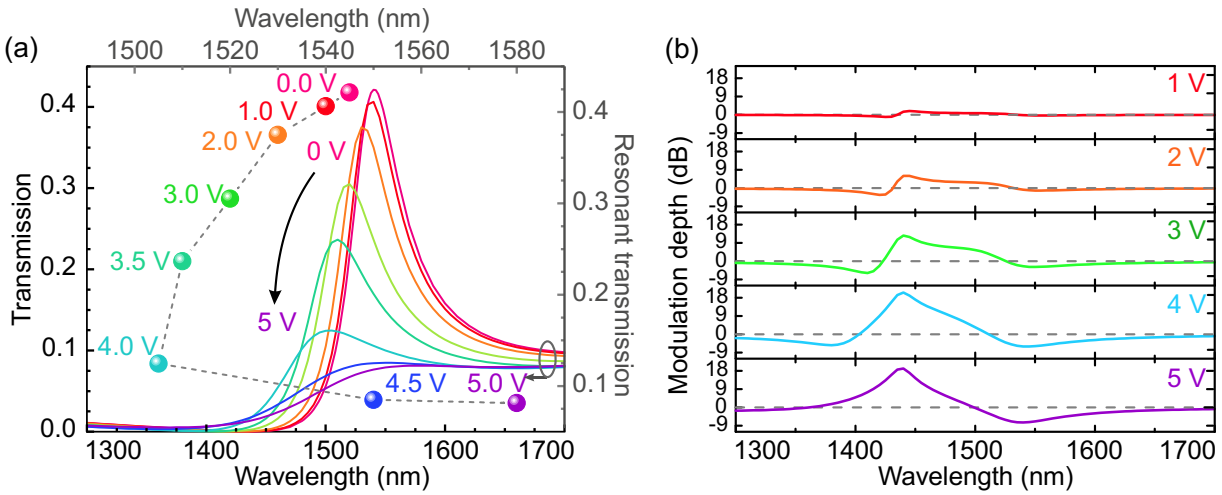

Figure 4-5 (a) Transmission spectrum, resonant transmission, and **(b)** modulation depth of the proposed structure with applied bias.

close to 3.9. It indicates that the ITO acts as a lossy dielectric material ($\varepsilon_{ITO} > 0$) due to the depletion of ITO. As applied voltage increases to 5 V, the real part of permittivity decreases to a negative value and hence exhibits metallic properties ($\varepsilon_{ITO} < 0$). And the ENZ region where the permittivity of the ITO approaches zero can be observed in Figure 4-4d (the white region for $\varepsilon_{ITO} = 0$). Therefore, by applying the bias and coupling to the ENZ region, the electric field distribution, as well as the transmission properties, in the proposed filter will be altered.

Next, we simulated the transmission of the color filter with introducing field effect modulation of the ITO. Figure 4-5a shows the transmission spectra for various voltage biases from 0 V to 5 V. Under low bias, there is an obvious resonant peak shift indicating the change of resonant properties of the structure due to the formation of the accumulation layer. As the bias increases, electrons concentrate increases and the permittivity decreases in these two accumulation layers. Once the ENZ wavelength range (a white region in Figure 4-4d) approaches to the resonant wavelength of the structure through applying voltage, the

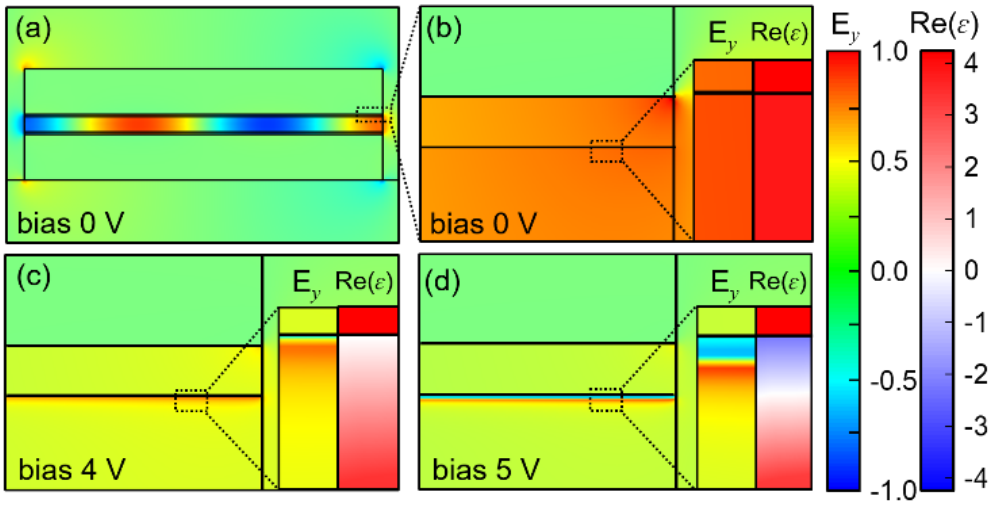

Figure 4-6 (a) Real part of *Y*-component electric field distribution of nanostrip area at 0 V. The zoom-in field and real part of permittivity distributions in the inset near HfO_2-ITO interface region under **(b)** 0 V, **(c)** 4 V and **(d)** 5 V.

resonant mode will couple to the ENZ mode [*52, 142*]. The coupling of the plasmonic resonance and the ENZ resonance can result in damping and hence leading to lower transmission (4 V and 5 V in Figure 4-5a). The substantial reduction of simulated transmission efficiency above 4 V is consistent with the formation of the ENZ layer in Figure 4-5d. Note that the resonance peak shifts under bias in Figure 4-5a. Two different regimes can be observed relating to the modification of the resonance. For a positive bias less than 4 V, the transmission peak shows a blueshift due to the decrease of permittivity with applied bias. In contrast, the peak redshifts under the bias higher than 4 V. This is because negative permittivity of the ITO is formed near the interface, making the region metallic. Consequently, the thickness of the dielectric ITO in the resonant cavity is shrunk which leads to a shift of transmission peak to longer wavelength.

To get insight into the modulation effect, modulation depth, MD (dB) = 10 × log (T_v/T_0), was calculated as shown in Figure 4-5b for bias from 1 V to 5 V. T_v and T_0 refer to

the transmission with and without the applied bias, respectively. The maximum modulation strength reaches 20.5 dB and 20.3 dB for 4 V and 5 V bias, respectively, representing a strong modulation. The insertion loss at maximum modulation is more than 17 dB. The modulation depth at 0 V is 7.41 dB with a much smaller insertion loss of 3.75 dB giving a larger net modulation with much lower losses. The real part of the *y*-component electric field inside the nanostrip at 1540 nm is shown in Figure 4-6 for illustration of the modulation performance. Without bias, the electric field at two cavity edges is antiparallel to each other in Figure 4-6a. Because the ITO layer and the HfO_2 layer behave as the dielectric cavity. Enlarged electric field distributions near the top HfO_2-ITO interface under 0 V, 4 V, and 5 V are shown in Figure 4-6b to 6d, respectively. The inset shows the magnified field and the corresponding permittivity distributions of the ITO within 2 nm area from the interface. Under 4 V and 5 V bias, as the permittivity of ITO decreases to zero, the electric field is enhanced in the accumulation layer due to the continuity of the normal component of electric displacement through the interface, which is caused by the coupling of ENZ resonance. Furthermore, the permittivity of the ITO at 5 V is negative at the interface leading to the sign-change of the electric field. This can be seen from Figure 4-6d, the field distribution agrees well with the permittivity distribution in the accumulation layer. Therefore, the significant change of the transmission is due to the ENZ coupling, which modifies the resonance properties of the structure.

To further analyze the role of the ITO accumulation layer in modifying the resonance, we investigated the transmission spectra with ITO layer thicknesses varying from 20 nm to 100 nm under the bias of 0 V, 3V, 4V, and 5 V. Taking the non-bias condition as an example,

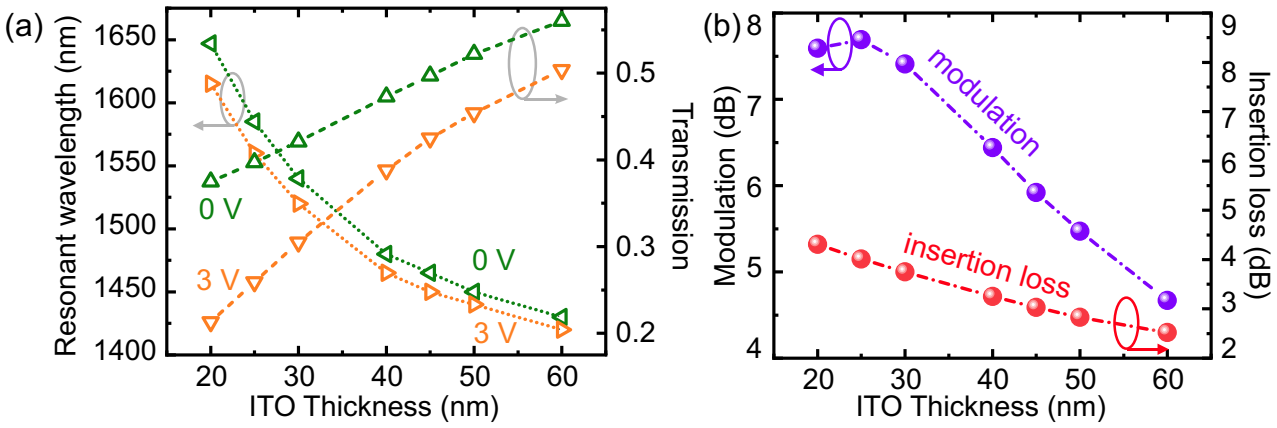

Figure 4-7 (a) Resonant wavelengths and transmission at resonances under 0 V and 3 V for different thicknesses of ITO layer. **(b)** The insertion loss at 0 V transmission peak and the modulation between 0 V and 5 V.

the resonance first shifts to a shorter wavelength and then remains a constant value as the ITO thickness increases (Figure 4-7a). The shifting regime for the thin ITO layer (< 60 nm) can be attributed to the resonance condition of the propagating plasmonic mode since the plasmonic resonance is sensitive to the cavity length. For the thick ITO layers, a larger cavity length leads to a lower quality factor and wider transmission bandwidth. As shown in Figure 4-5a the transmissions with the bias of 4 V and 5 V are much lower compared to 0 V and 3 V. The transmission decreases as the ITO layer gets thinner. The transmission for 4 V and 5 V is less than 10% with 20-nm thick ITO. Therefore, the transmission of 4 V and 5 V were excluded from Figure 4-7a. The small transmission of 4 V and 5 V occur because the accumulation layers in ITO introduces ENZ and metal-like material near the interfaces. The low transmission and transmission peak shift for the 5 V bias as ITO gets thinner is not suitable for a color filter application but is good for a modulator application. However, there is a good transmission value more than 20% for 3 V with a peak shift of ~35 nm. As the ITO layer gets thinner, we can see a larger peak shift for 3 V because of the accumulation layers making up a larger partition of the total ITO thickness. Figure 4-7b shows an increase of both

insertion loss and modulation depth of 0 V and 5 V as the ITO layer gets thinner because the plasmonic confinement is comparable with the thickness of the formed accumulation layer. The slight decrease in modulation for 20nm thick ITO is a result of the larger wavelength transmission tails along with the blue shifted transmission peaks at the bias of 5 V, which can be seen in Figure 4-5, resulting in the 5 V transmission not getting suppressed as fast as the 0 V transmission when the ITO layer gets thinner. This could potentially be improved by optimizing the design parameters to counteract the blue shift from shrinking ITO.

4.4 Summary

We have proposed an electrically tunable metasurface color filter with metal-insulator-metal heterostructure nanostrip arrays. The desired resonant peak has been realized through designed geometrical parameters. The ITO layer inside gold grating enables the modulation of transmission properties which manifests in altering the transmission efficiency and shifting the transmission peak position with external bias. The structure leads to stronger modulation strength and larger peak shifting with thinner ITO. An electrically-modulated nanoscale color filter could find applications in imaging, display, and optical or bio-sensing devices.

Chapter 5 Excitation of Epsilon-Near-Zero Mode in Optical Fiber

In this chapter, we present the experimental demonstration of epsilon-near-zero (ENZ) mode in a side-polished optical fiber (*i.e.,* D-shaped fiber) uniformly coated with aluminum-doped zinc oxide (AZO) nanolayer. We observed a transmission resonance dip in the ENZ regime in an ENZ-optical fiber with a 30 nm-thick AZO layer, which is attributed to the phase matching between the fundamental mode of the optical fiber and ENZ mode supported by the ultrathin AZO film as discussed in Section 2.2. In addition, the hybrid ENZ resonance in the AZO-ENZ optical fiber could be tuned by an external refractive index, nonlinear Kerr effect or gate-tunable structure in Section 2.3. Main results in this chapter were submitted by the author of this dissertation.

5.1 Background

In Chapter 2, we discussed that a thin layer of ENZ material can support the plasmon polariton mode with a highly confined and enhanced optical field (*i.e.,* ENZ mode) [*76-79*]. Heavily doped transparent conducting oxide (TCO) with a carrier concentration of 10^{19} to 10^{21} cm^{-3} in ultrathin films supports the ENZ mode in the near-infrared frequency [*50*]. Recent studies on utilizing ultrathin TCO-ENZ films have demonstrated various applications, for instance, broadband perfect absorbers [*152*], ultrafast switching [*153*], strong coupling between the nano-antenna and the ENZ mode [*71, 154, 155*], *etc*. In addition, the optical responses of ENZ mode could be further actively controlled by electrically gating the TCO-dielectric-metal heterostructure [*32, 52, 142, 148, 156*] or by a high-intensity ultrafast optical pulse via the enhanced Kerr ENZ nonlinearity [*70, 157-159*]. However, ENZ modes on planar substrates require prism or grating for coupling with a relatively short light-matter

interaction length.

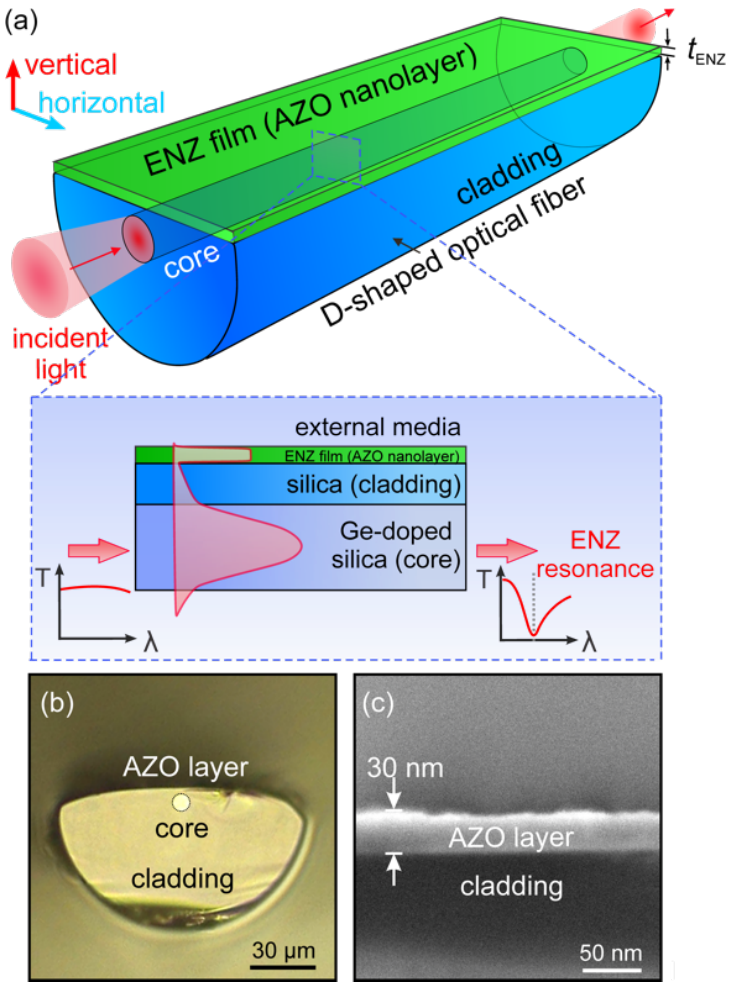

Figure 5-1 Excitation of epsilon-near-zero (ENZ) mode in the optical fiber. **(a)** Schematics of ENZ film-coated D-shaped optical fiber. The thickness of the ENZ layer is labelled as t_{ENZ}. Inset: Flat geometry of Ge-doped glass-pure silica-aluminum zinc oxide (AZO)-air four-layer structure for ENZ mode excitation. **(b)** Optical microscopic image of an AZO-coated D-shaped optical fiber sample cross section. **(c)** SEM image of the AZO layer cross section on the D-shaped fiber.

In this work, we demonstrate an efficient method of exciting the hybrid ENZ mode in an optical fiber uniformly coated with a thin AZO layer. The ultrathin AZO layers, grown by atomic layer deposition, possess the ENZ properties at near-infrared wavelengths. Highly polarization- and wavelength-dependent resonance in the transmission was experimentally

observed in the ENZ-optical fiber. We also show that the resonance wavelength and the transmission of ENZ resonance can be modulated by varying the surrounding refractive index of the ENZ-optical fiber or large nonlinearity of the ENZ film induced by a femtosecond laser pulse. The ENZ-optical fiber, with relatively long light-matter interaction length, propagation length, and controllable coupling strength, provides a novel platform for ENZ mode excitation and simplifies the optical configuration for development of zero-index photonic applications and compact in-fiber devices.

5.2 Design and fabrication

A conceptual representation of the ENZ mode excitation in a D-shaped optical fiber is shown in Figure 5-1a. The D-shaped fiber (Phoenix Photonics, SPF-S-SM-0) employed here is a modified version of the conventional step-index single-mode fiber (Corning, SM-28) with core and cladding diameters of 8.2 μm and 125 μm, respectively, as shown in Figure 5-2a. The length of the side-polished platform is ~17 millimeter and the cladding thickness between the polished side and the edge of the core is ~1 μm. The core and cladding materials of the D-shaped fiber used are Ge-doped silica with weight ratio of 4% and pure silica, respectively. The refractive indices of Ge-doped silica and pure silica are modeled with standard Sellmeier expansion [*40*]. The simulated mode profile (*i.e.,* electric field magnitude distribution) is shown in Figure 5-2b. The electric field distribution across the center of the D-shaped fiber along *y* direction is shown in Figure 5-2c. While light is propagating in the fiber core, the evanescent field extending to the polished cladding can interact with the ambient environment close to the flat platform. The optical microscope image of an AZO-coated D-shaped fiber cross-section is shown in Figure 5-1b.

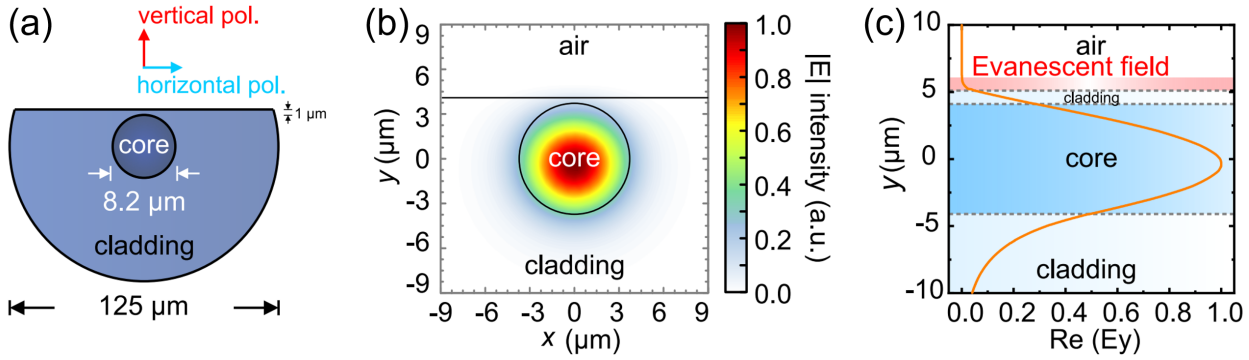

Figure 5-2 (a) Schematics of the cross-section of the D-shaped optical fiber. **(b)** Electric field profile of the fundamental mode of D-shaped fiber at operation wavelength of 1550 nm. **(c)** Line profile of the electric field distribution of the D-shaped fiber across the center along y direction.

The flat platform of the D-shaped fiber is uniformly coated with the ultrathin AZO-ENZ film by atomic layer deposition (ALD) technique. The AZO films were grown by atomic layer deposition (ALD, Arradiance GEMSTAR-8™ Bench-Top system) on silica substrates and D-shaped optical fiber. The samples were cleaned by ultrasonication in acetone and isopropanol. After cleaning, the samples were rinsed with de-ionized water and dried with nitrogen gas. The base pressure of the deposition was set to 200 mTorr. The precursors, diethylzinc and trimethylaluminum, are from Strem Chemical, Inc. The details of the ALD process were described in our recent publications [*53, 160*]. Due to the self-limiting surface chemical reaction in the ALD process, the conformal AZO film has a thickness of only a few to few tens of nanometers and uniform surface smoothness [*161*]. The SEM image of the 30-nm AZO-coated D-shaped fiber cross-section is shown in Figure 5-1c. The ALD-fabricated AZO thin films have good uniformity with the typical surface roughness (average deviation) of 2.54 nm for 30-nm-thick film measured via atomic force microscope. Moreover, the material composition and thickness of the AZO layer can be precisely controlled by the deposition parameters in the ALD process, such as growth temperature, doping ratio of the

aluminum, the number of deposition cycles, *etc.* [*151, 162*]. Therefore, the properties of thin AZO film (*i.e.,* the ENZ wavelength and film thickness) can be engineered during the ALD process, that is critical for the efficient excitation of ENZ resonance [*53, 160*]. The parameters of the deposition are optimized so that the AZO thin films exhibit ENZ properties in the telecommunication wavelengths. After deposition, the complex dielectric permittivity, and the thicknesses of two fabricated AZO layers were characterized via ellipsometry. The dielectric function of AZO layer ε_{AZO} can be described by the Drude model in Equation 2-11 [*151*]. The values of ε_∞, ω_p, and Γ were obtained by fitting the data from the ellipsometry measurement (see Table 5-1 for fitting parameters). The two fabricated fiber samples have the ENZ wavelengths (where the real part of permittivity crosses zero) of 1545 nm and 1578 nm with AZO thicknesses of 30±1 nm and 73±2 nm, respectively. For convenience, we denote these two fiber samples as AZO-30 and AZO-73. The measured complex permittivity dispersions of two AZO layers are shown in Figure 5-4a and 4b with the ENZ regimes highlighted in gray. Note that while these two samples have different thicknesses, we controlled the ENZ wavelength to be close to each other by two different deposition conditions.

Table 5-1 The Drude parameters and thickness obtained from ellipsometry measurement

Sample	AZO-30	AZO-73
Permittivity at high-frequency limit ε_∞	4.1504	3.7171
Plasma frequency ω_p (rad·s^{-1})	2.5247×10^{15}	2.3775×10^{15}
Electron collision rate Γ (rad·s^{-1})	2.1248×10^{14}	3.0440×10^{14}
Thickness (nm)	30 ± 1	73 ± 2

5.3 Measurement and discussion

Next, we performed optical measurements on these two AZO-coated D-shaped fibers. We first measured the transmission through the fabricated samples using a supercontinuum light source, a precise incident polarization control element and an optical signal analyzer Light from a supercontinuum light source (SC laser, wavelength range: 400-2000 nm, NKT Photonics, Fianium) is launched through a linear polarizer (Thorlabs, LPNIR100-MP2) and a half-wave plate (Thorlabs, AHWP05M-1600) to generate a linear polarized light beam as shown in Figure 5-3. The beam is then focused by an objective lens (40× magnification, numerical aperture, NA = 0.65) into the AZO-coated D-shaped fiber. At the output end, two other objective lenses (40× magnification, NA = 0.65 and 20× magnification, NA = 0.4, Newport), step-index multimode fiber patch cable (NA = 0.39, Thorlabs) and an optical signal analyzer (Yokogawa, AQ6370C, detection range: 600-1700 nm) are used to record the transmission spectra. The side polished platform of the AZO-coated fiber was carefully aligned to face to horizontal direction by observing it with a CCD camera. The incident polarization was varied by rotating the half wave plate in the setup to obtain the TM and TE transmission spectra of AZO-coated D-shaped fiber. Special attention was paid before the measurement so that the AZO film on the polished side of the fiber was aligned horizontally and the whole fiber sample was free from any bending or twisting. A linear polarizer along with a half-wave plate was employed to control the incident polarization. The horizontal or vertical polarization is defined as the incident polarization parallel or perpendicular to the surface of the AZO film on the flat platform in Figure 5-4a. Figure 5-4c and 4d (solid lines) show the measured transmission spectra of AZO-30 and AZO-73 in the air.

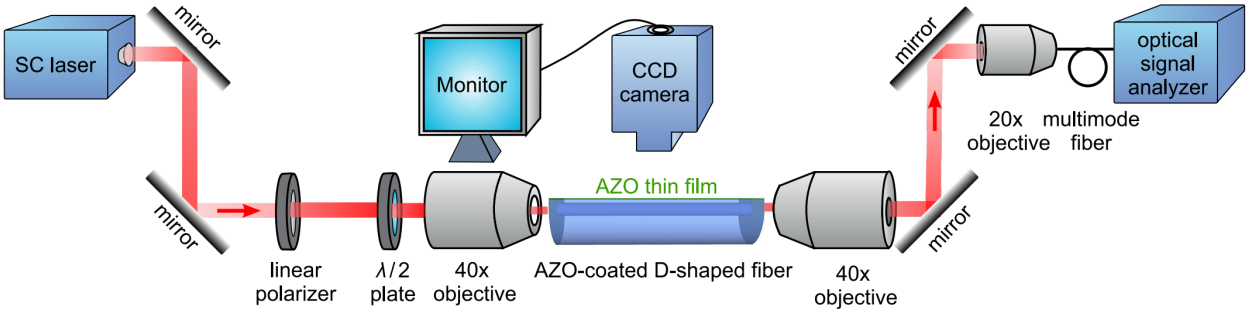

Figure 5-3 Schematic of experimental setup for characterizing the optical properties of AZO-coated D-shaped fibers.

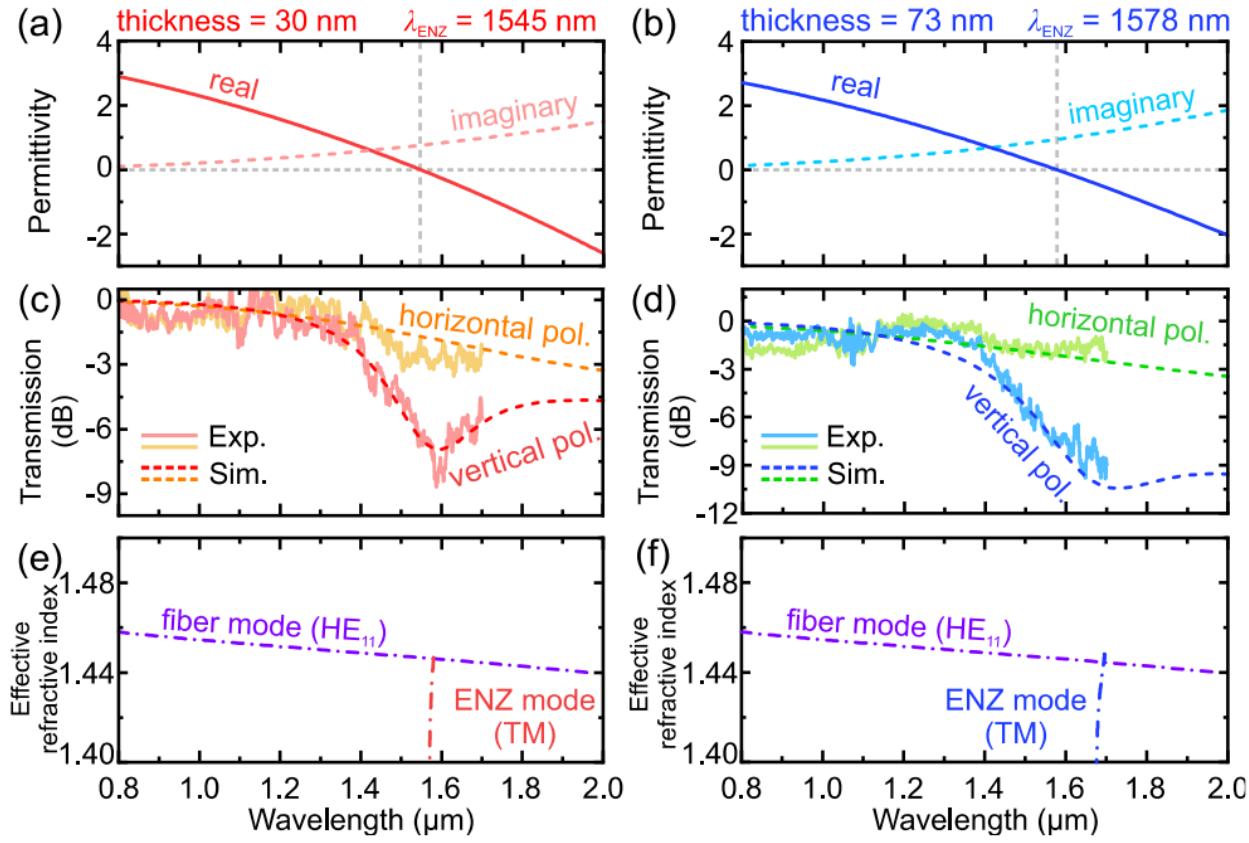

Figure 5-4 ENZ-AZO D-shaped fibers in the air. (a, b) Measured complex permittivity of the AZO-30 and AZO-73. The AZO films with thicknesses of 30 and 73 nm have ENZ wavelengths (with the real parts of permittivity crossing zero) at wavelengths of 1545 and 1578 nm. The ENZ regime is highlighted in gray. **(c, d)** Measured transmission and simulated modal loss spectra with vertical and horizontal polarization at 600-1700 nm. **(e, f)** Phase matching conditions between the fundamental mode (HE_{11}) of the D-shaped fiber and the thin-film ENZ mode supported by the four-layer geometry (Ge-doped glass-silica-AZO film-air).

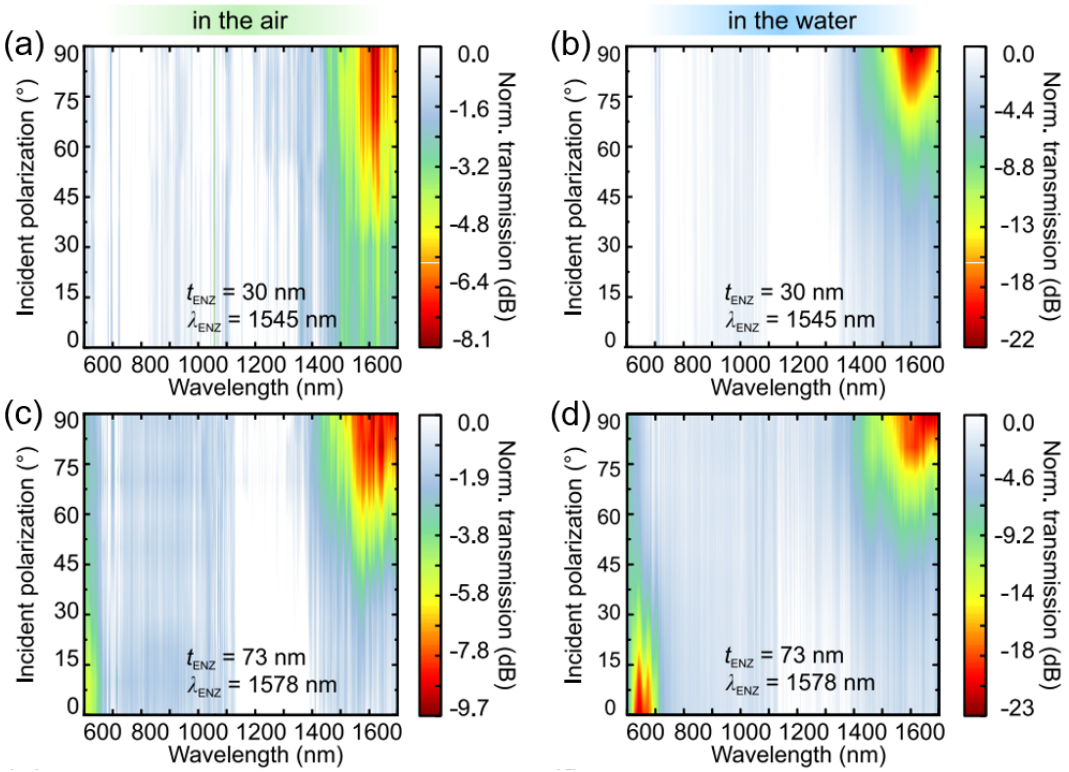

Figure 5-5 Measured transmission of AZO-coated D-shaped fibers with different incident polarizations. Measured and normalized transmission of **(a, b)** AZO-30, **(c, d)** AZO-73 ENZ D-shaped fiber with the incident polarization direction varying from parallel (0°) to perpendicular (90°) to the side-polished platform of D-shaped fiber in the air **(left)** and in the water **(right)**, respectively.

The resonance dips in the transmission with vertical incident polarization were observed at a wavelength of ~1590 nm (with a resonance depth of ~8 dB) and ~1700 nm (with a resonance depth of ~10 dB), respectively. These two resonances of AZO-30 and AZO-73 samples are in the ENZ regimes (real part of permittivity between ±1) highlighted with gray shaded area in Figure 5-4a and 4b, respectively. In addition, no resonances were observed with the horizontal polarization of incident light, indicating that vertically polarized light interacts strongly with the thin AZO films on the optical fiber as the ENZ mode could be excited efficiently with the transverse-magnetic (TM) polarization but not with

transverse-electric (TE) polarization [*76*] (see Figure 5-5 for measured transmission of AZO-coated D-shaped fibers with other incident polarizations).

We additionally measured the input and output light polarization for an uncoated D-shaped using a polarimeter (Thorlabs, PAX1000IR2). The total polarization angle rotation due to in-coupling from free space to the fiber, propagation along the fiber and out-coupling back to free space is less than 1.3° and the degree of polarization difference is less than 2% (Table 5-2). Thus, the undesired rotation of polarization here is negligible along the propagation of the D-shaped fiber.

Table 5-2 Comparison of the input and output polarization of the uncoated D-shaped fiber

Polarization	**0°**		**90°**	
Position	**input**	**output**	**input**	**output**
Azimuth	-0.98°	-0.72°	89.78°	89.05
Degree of polarization	100.0%	98.73%	100.0%	98.93%
Ellipticity	-2.09°	-2.64°	-0.35°	2.70

To elucidate the origin of the resonance dips in measured transmissions, the electromagnetic behavior was modeled using the full-wave electromagnetic simulations. Full-wave simulations (modal loss spectra) of the AZO-coated D-shaped fiber, fundamental mode dispersions of D-shaped fiber and the field-profiles of the ENZ modes in the AZO-coated D-shaped fiber were performed using MODE Solution from Lumerical, Inc. The complex frequency-dependent dielectric permittivity of the AZO layer is described by Drude model with damping constant and plasma frequency obtained by ellipsometry measurements (see Table 5-1 for the fitting parameters of the AZO films). For AZO-30 and AZO-73 samples, the modal loss curves of the fundamental mode (HE_{11}) of the D-shaped fiber are depicted in Figure 5-4c and 4d (dashed curves). The

resonance loss dip of 7.5 dB (with loss of 4.4 dB/cm) at 1590 nm (AZO-30) and 10.7 dB (with loss of 6.3 dB/cm) at 1714 nm (AZO-73) were observed in the vertical polarization state while no lossy resonance was observed in the horizontal polarization state. These observations from simulations are in good agreement with the experimental results.

We further investigated the characteristics of the mode dispersion to understand the ENZ mode-coupling mechanism. The configuration of AZO-coated D-shaped fiber can be simplified as a four-layer geometry (Ge-doped glass-silica-AZO-air interfaces) as shown in the inset of Figure 5-1a. We calculated the effective index of the non-radiative thin-film ENZ mode supported by the four-layer geometry with TM incident polarization (corresponding to vertical incident polarization in the fiber) via the transfer matrix method [*148*]. The dispersion characteristic of the ENZ modes supported by a four-layer stack having the AZO film was obtained by locating the minima on the reflectivity spectra. The dispersion characteristic of the ENZ modes supported by a four-layer stack having the AZO film was obtained by locating the minima on the reflectivity spectra. The dispersion of the fundamental mode (HE_{11}) of the D-shaped fiber was calculated via the finite element method. The crossing point of the dispersion curves of the ENZ mode and the HE_{11} mode indicates the phase-matching condition where the coupling occurs. For the AZO-30 and AZO-73 samples, phase matching conditions are satisfied at wavelengths of 1587 nm and 1694 nm (Figure 5-4e and 4f), coinciding with the measured and simulated transmission dips (Figure 5-4c and 4d).

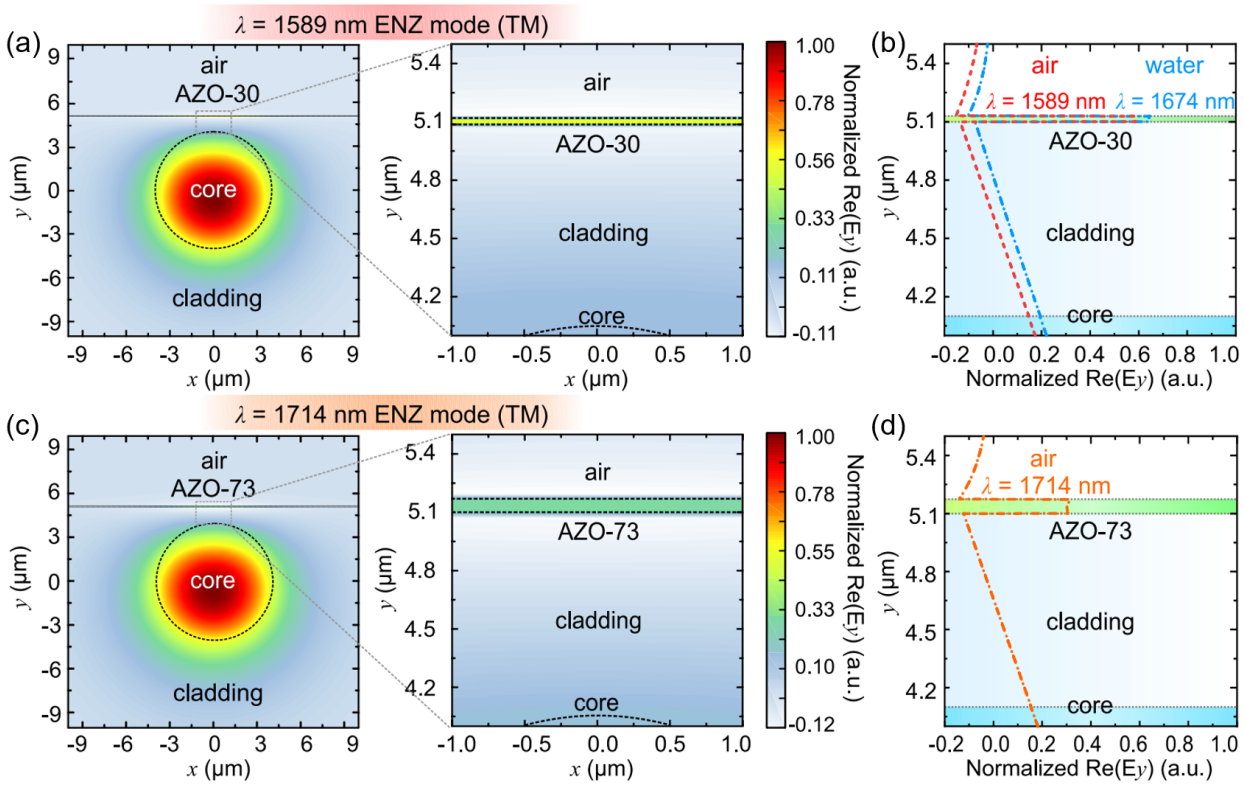

Figure 5-6 Mode profiles of ENZ modes in the AZO-coated D-shaped fibers. (a, c) Electric field distributions of hybrid ENZ modes on AZO-30 and AZO-73 in the air. **(b, d)** Y-components of electric field distributions (E_y) along the vertical line across the center of the AZO-coated D-shaped fibers.

Table 5-3 Comparison of propagation length of the ENZ modes on different substrates

Type	Propagation length	Reference
ENZ mode on planar substrates	0.14-0.3 μm	[*77*]
Hybrid ENZ-SPP mode on planar substrates	4.8-17.2 μm	[*163*]
Hybrid ENZ mode in the fiber	0.5-1.2 cm	this work

The simulated mode profiles of the hybrid ENZ modes in the AZO-30 and AZO-73 D-shaped fibers at corresponding resonance. wavelengths are shown in Figure 5-6a and 5c. The regions surrounding the ENZ layer are enlarged and shown in the insets. Note that the electric fields at resonance are confined and enhanced in the ENZ layers. The line profiles of

the electric field along the vertical line across the center of AZO-coated D-shaped fiber (Figure 5-6b and 5d) reveal that the electric field (*i.e.*, $E_{\perp}$) of the ENZ mode is much stronger in AZO-30 than in AZO-73. It is consistent with the conclusion that the ENZ mode in the thinner layer possesses stronger electric field intensity [*76*]. These hybrid modes at resonances possess not only the characteristics of the ENZ mode with a confined and enhanced electric field component in the nanolayer but also the properties of a well-guided HE_{11} mode in the fiber core. Compared to the excitation of an ENZ mode on the planar substrates, these hybrid ENZ modes on the optical fiber have much lower loss and exhibit longer propagation length (5-12 mm), which is four orders of magnitude longer than that of the ENZ mode (0.14-0.3 μm) and hybrid ENZ-surface plasmon-polariton (SPP) mode (4.8-17.2 μm) on the planar substrates (see Table 5-3 for the comparison of propagation lengths of hybrid ENZ mode in the fiber, ENZ photonics wires, ENZ mode and hybrid ENZ-SPP mode on the planar substrates) [*77, 163, 164*]. Note that there is a tradeoff between propagation length and field confinement of the hybrid ENZ mode. In our previous numerical work, the excitation of hybrid ENZ mode in a 5-nm ITO shell embedded in the core of the nanostructured optical fiber exhibits much higher confinement and enhancement of electric field but with a much higher loss of 41 dB/cm and lower propagation length [*39*]. However, the propagation length and field confinement of the AZO-coated D-shaped fiber can be engineered by judiciously choosing the structural parameters, such as the thickness of the ENZ layer, the separation distance between the fiber core and ENZ layer, and the length of the side-polished region (see Figure 5-9 for the simulated details of the ENZ resonance with structural parameters of the AZO-coated D-shaped fiber). In addition, the coupling mechanism of the ENZ in-fiber platform relies on the phase matching condition between the

fundamental mode of the fiber and the ENZ mode supported by the AZO film, which is convenient for the ENZ mode excitation compared to the Kretschmann configuration on planar substrates assisted by the complex setting of a prism or grating coupling.

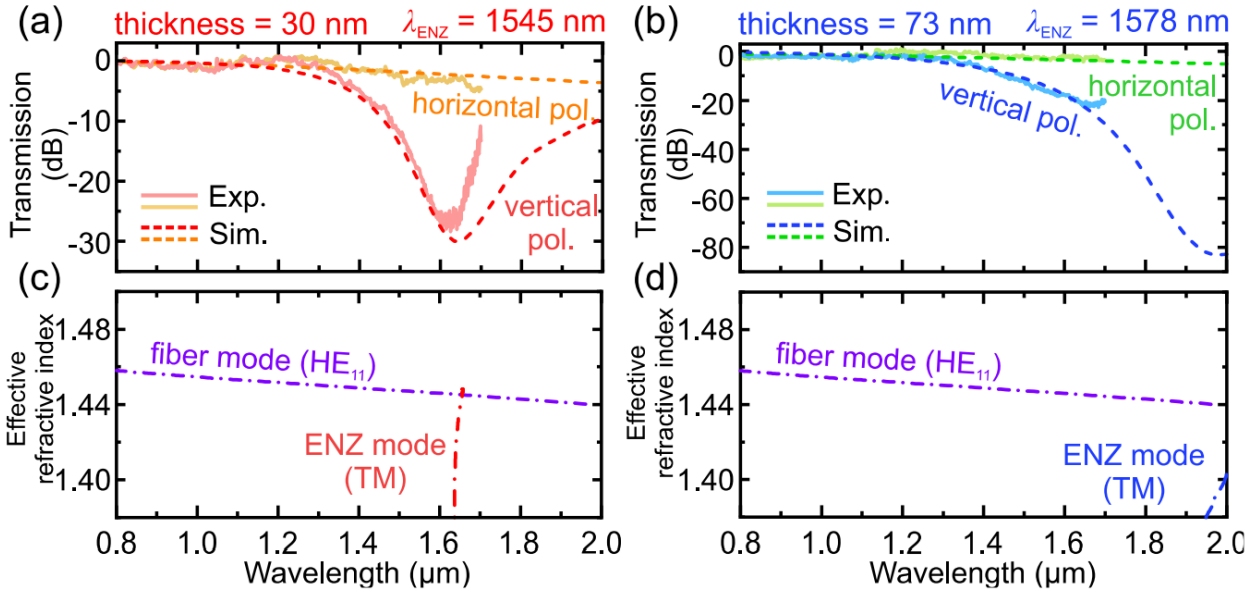

Figure 5-7 ENZ-AZO D-shaped fibers in the water. **(a, b)** Measured transmission and simulated fundamental modal loss spectra of AZO-30 and AZO-73 fiber samples with vertical and horizontal polarization. The measured wavelength range is 600-1700 nm. **(c, d)** Phase matching conditions between fundamental mode of D-shaped fiber and thin-film ENZ mode supported by four-layer geometry (Ge-doped glass-silica-AZO film-water) for AZO-30 and AZO-73.

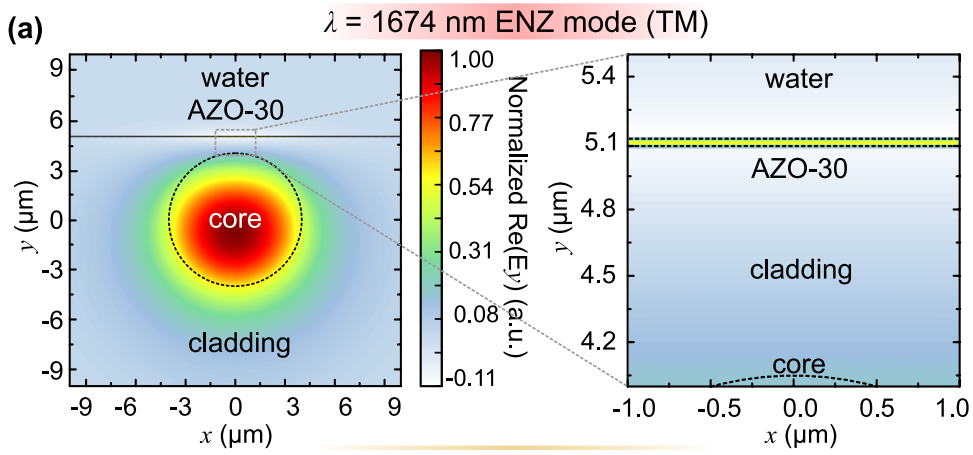

Figure 5-8 Mode profiles of the ENZ mode on AZO-coated D-shaped fiber immersed in water. **(a)** ENZ mode profile (real part of *y*-component of electric field) of AZO-30 sample.

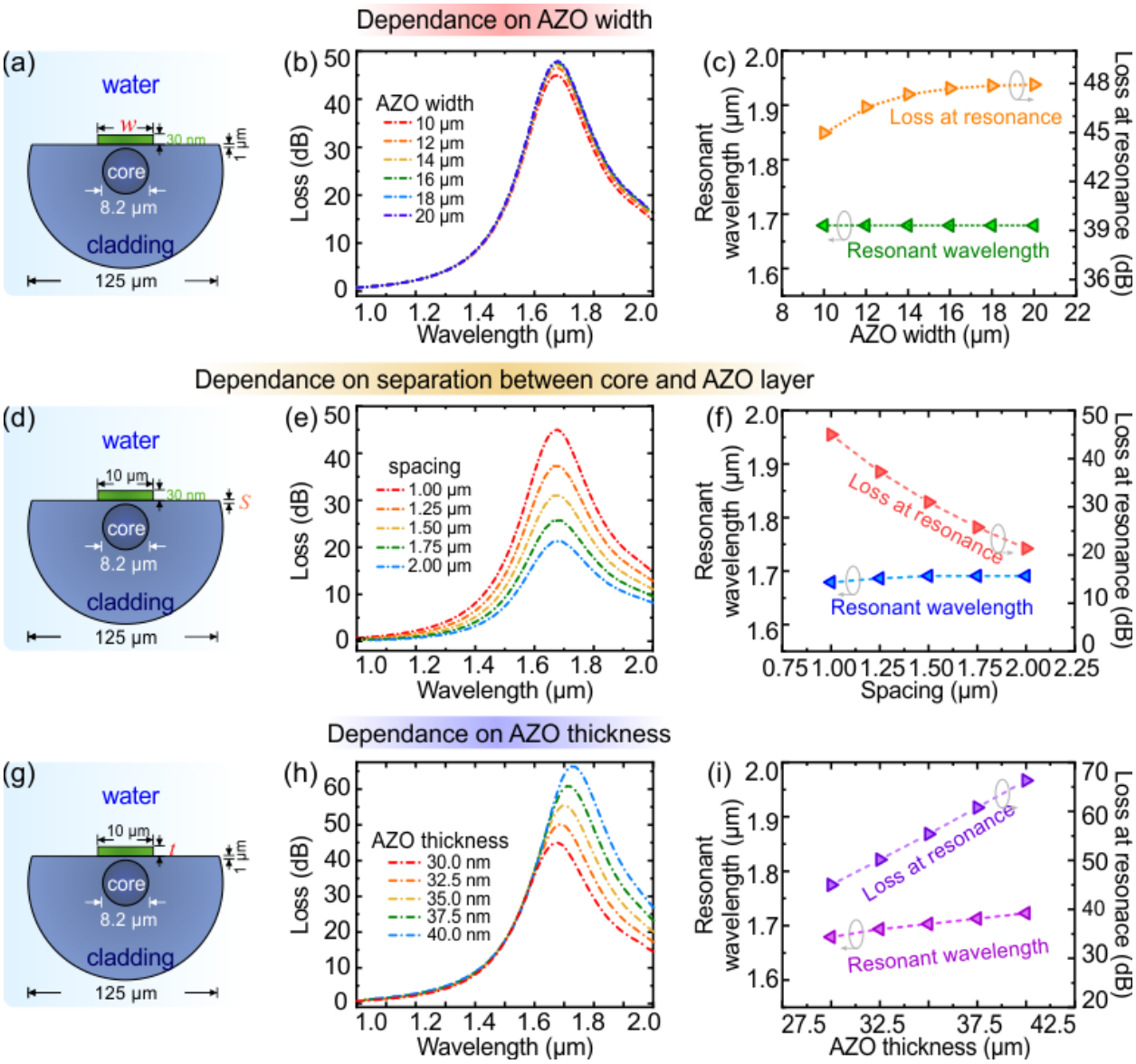

Figure 5-9 Full-wave simulation for AZO-coated D-shaped fiber. **(a)** Schematics and **(b)** simulated fundamental modal loss spectra of AZO-coated fiber with varying widths (10-20 μm) of the AZO layer. **(d)** Schematics and **(e)** simulated fundamental modal loss spectra of AZO-coated fiber with varying separation (1-2 μm in a step of 0.25 μm). The separation is the thickness of cladding between the edge of the fiber core and the AZO layer. **(g)** Schematics and **(h)** simulated fundamental modal loss spectra of the AZO-coated fiber with varying thickness of the AZO layer (30-40 nm). Variation of the resonance wavelength and loss at resonance dependent on **(c)** the width of AZO layer, **(f)** the separation, and **(i)** the AZO thickness, respectively.

To study the responses of ENZ mode to the refractive index of the ambient environment, we immersed the flat portions of the fiber sample in the de-ionized (DI) water. The ENZ resonance on the AZO-30 sample redshifts from ~1590 nm in the air (Figure 5-4c) to ~1645 nm in the water and the resonance strength of the transmission dip is enhanced to ~20 dB in the water (Figure 5-7a). The corresponding simulated loss spectrum in Figure 5-7a shows a good agreement on the resonant wavelength at 1674 nm and the transmission dip of 41 dB (with a loss of 24 dB/cm) at 1674 nm. The slight mismatch on the magnitude of resonance dip between the simulated and experimental results may be attributed to slightly different polishing conditions and non-uniformity during the fiber manufacturing process leading to variation in the cladding thickness between the AZO layer and the edge of the core (see Figure 5-9 for the study on the impact of structural parameters on the ENZ resonance). The calculated intensity of the electric field inside the AZO layer is greater with the DI water than the air as the ambient environment (Figure 5-6b) (see Figure 5-8 for the ENZ mode profile of the AZO-30 in the water). The phase matching point between dispersions of HE_{11} and ENZ mode shifts from 1587 nm in the air (Figure 5-4e) to 1673 nm in the water (Figure 5-7c), which agrees with the measured resonance and the simulated loss spectra (Figure 5-7a). For the AZO-73 sample, the transmission loss in the ENZ regime is enhanced but the ENZ resonance redshifts beyond 2000 nm (Figure 5-7b) (*i.e.,* no phase matching condition between HE_{11} mode and ENZ mode below 2000 nm as shown in Figure 5-7d).

To further study the ENZ resonance on optical fiber, we performed numerical simulations for different parameters of the AZO thin films (*e.g.,* width, spacing between the core, and thickness) on the D-shaped fiber. In these simulations, we used AZO-30 fiber as example (included the complex dispersion of AZO layer) and an external environment of DI

water. The minimum mesh size of the simulation in the AZO layer is 0.5 nm. Firstly, we investigate the dependence of the ENZ resonance with the width of the AZO nanolayer (Figure 5-9a). We set the thickness of AZO layer at 30 nm, the separation between the side-polished platform and the edge of the core at 1 μm, and varied the width (*W*) of the AZO-layer from 10 μm to 20 μm. The simulated modal loss spectra of the fundamental mode of the fiber are shown in Figure 5-9b. The ENZ resonance wavelength remains constant at 1674 nm, and the magnitude of the loss vary slightly between 45-48 dB (Figure 5-9c). Therefore, the optical property of the ENZ-optical fiber is almost independent of the width of the AZO layer beyond 10 μm. Next, we swept the cladding thickness or separation between the edge of the core to the AZO film from 1 μm to 2 μm in 0.25 μm steps and fixed the other parameters (with the AZO-layer width of 10 μm) (Figure 5-9d). The simulated loss spectra (Figure 5-9e) shows that the ENZ resonances are located at similar wavelength for different separations. But the resonance loss depth changes significantly with different separation distances (21-45 dB) (Figure 5-9f). Therefore, the ENZ coupling is highly sensitive to this separation, and slightly different polishing conditions and non-uniformity could cause the variation on the magnitude of resonance strength. Finally, we changed the thickness of the AZO layer from 30 nm to 40 nm in 2.5 nm steps, and the results are shown in Figure 5-9g and 9h. The ENZ resonance redshifts from a wavelength of 1674 nm to 1722 nm, and the resonance strength increases from 45 dB to 66 dB with the increase of the ENZ layer thickness (Figure 5-9i). Thus, the thickness of the ENZ layer is also one of the key parameters which we controlled precisely with the ALD for efficient excitation of the ENZ mode.

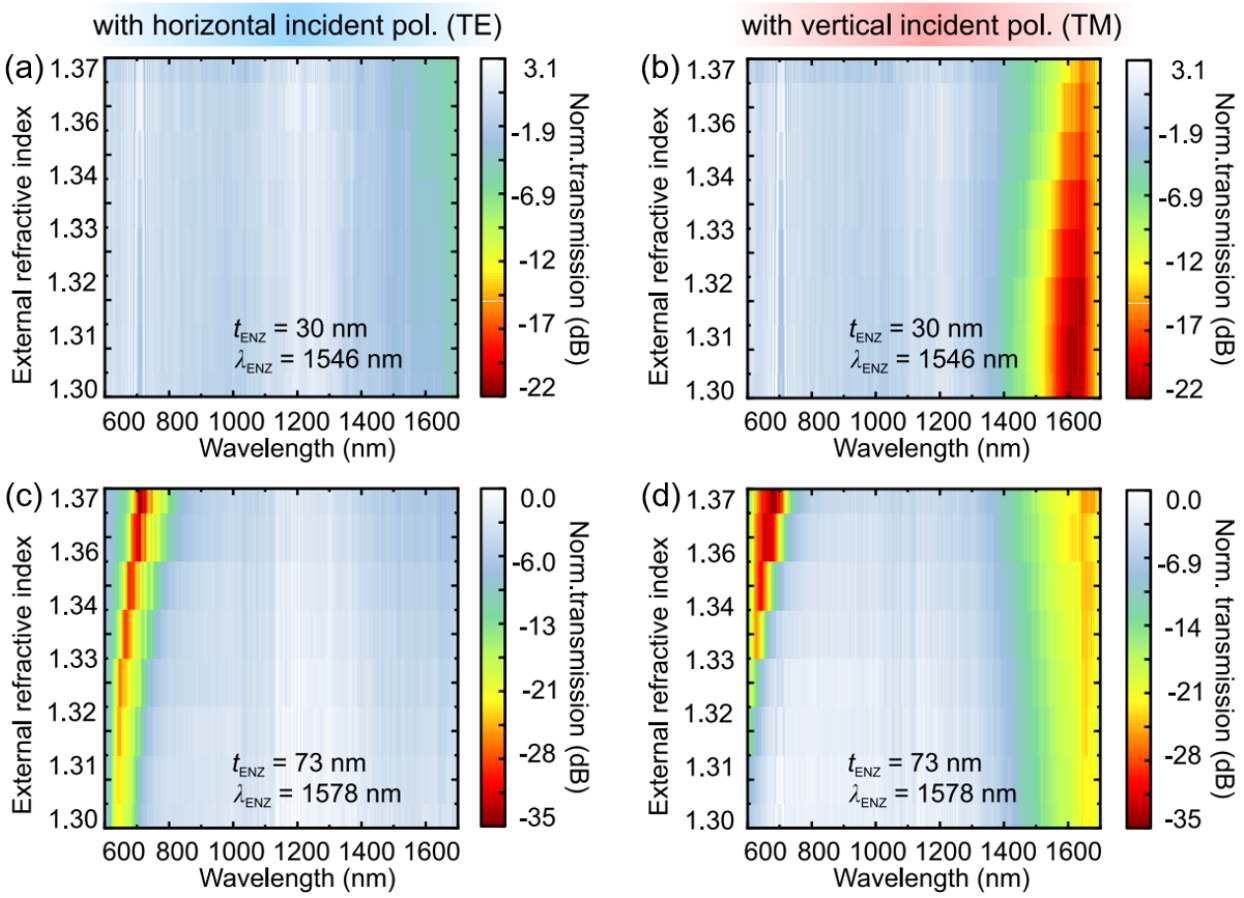

Figure 5-10 Measured transmission of the AZO-coated D-shaped fibers with external refractive index. Measured transmission of **(a, b)** AZO-30, **(c, d)** AZO-73 ENZ D-shaped fiber immersed in different refractive index liquid (1.30-1.37) with **(a, c)** horizontal and **(b, d)** vertical incident polarizations.

Next, we explore the tunability of ENZ resonance by ambient refractive index (see Figure 5-10 for measured transmission of the AZO-coated D-shaped fiber with n = 1.30-1.37 in 400-1700 nm). We simulated the transmission of the AZO-73 sample up to the wavelength of 2500 nm to study the response of the sample to external refractive indices (RI, *n*). With the ambient RI of a water-glycerin solution increases from *n* = 1.30 to 1.37, the ENZ mode resonance redshifts by 326 nm (2001 to 2327 nm, Figure 5-13a). Maximum wavelength tunability of 8069 nm/R.I.U. and strength tunability of -6986 dB/R.I.U. were achieved with

ENZ resonance of the AZO-73 sample (Figure 5-13b). The sensitive response of the ENZ-AZO-coated D-shaped fiber is comparable to or even better than the most current in-fiber interferometer sensors (with a sensitivity of up to 6000 nm/R.I.U.) and the grating-based sensors (with a sensitivity of up to 2000 nm/R.I.U.) [*165-169*].

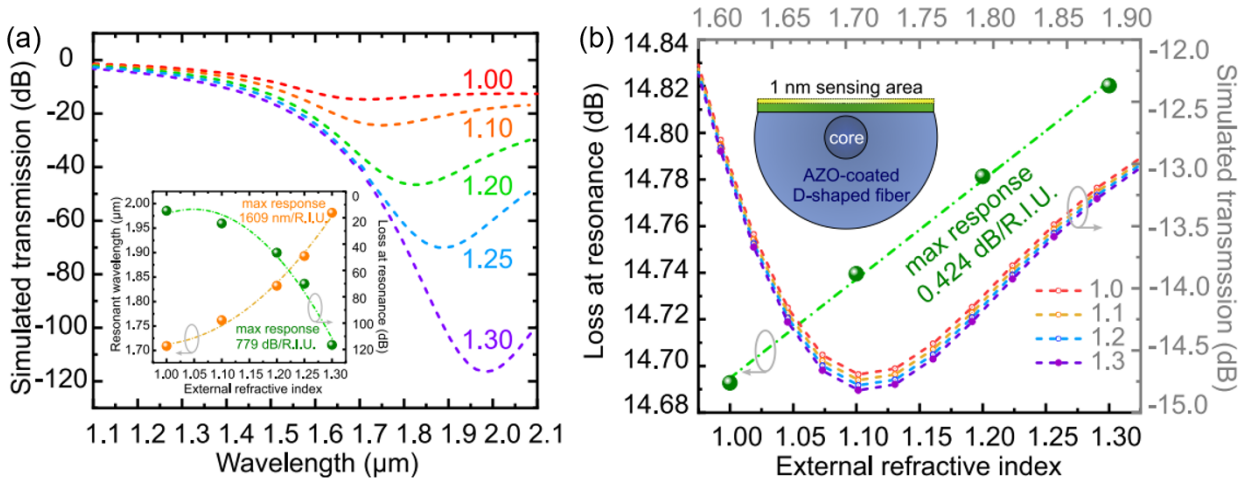

Figure 5-11 (a) Simulated transmission of ENZ mode on AZO-73 D-shaped fiber immersed in various refractive index liquids (n = 1.0-1.3). Inset: simulated resonant wavelength and transmission of ENZ mode versus external refractive index. **(b)** Left: Loss at ENZ resonance versus external refractive index (n = 1.0-1.3) with 1-nm-thick sensing area. Right: Simulated transmission of ENZ mode on AZO-73 D-shaped fiber with 1-nm-thick sensing area.

Besides, owing to the excitation condition of the hybrid ENZ mode, the external refractive index sensing range of the proposed device can be extended to *n* = 1.0-1.3 which is not accessible to most optical fiber sensors based on surface plasmon resonance without fiber grating and fiber post-processing because the surface plasmon mode could not be excited in those conditions. We also performed simulations to calculate the sensitivity in the low external refractive index regimes (n = 1.0-1.3) with fixed complex permittivity of the AZO film and structural parameters of 73-nm AZO-coated D-shaped fiber (Figure 5-11a). The resonant wavelength of the ENZ mode redshifts and loss is increased with increasing

external refractive index. The maximum responses with external refractive index (n = 1.0-1.3) are 1609 nm/R.I.U. and 779 dB/R.I.U., respectively, as shown in the inset of Figure 5-11a. Compared to sensors based on surface plasmon resonance, the hybrid ENZ mode in the fiber has extended index sensing range from 1.0 to 1.3, which is unique for applications such as gas-sensing. Moreover, we push the sensing area with the thickness of 1 nm with changing refractive index from 1.0 to 1.3, simulated transmission is shown in Figure 5-11b. The refractive index response is linear with sensitivity of 0.424 dB/R.I.U. in the refractive index range of 1.0-1.3 (Figure 5-11b). The low refractive index detection range (n = 1.0-1.3) is naturally applicable to gas sensing without the membrane used for concentrating the gas molecules. Moreover, due to the confined ENZ mode, the AZO-coated fiber can detect ultrathin layers (1 nm) of analytes, showing the promise for bio-sensing and single biomolecule sensing. Note that the RI response of the hybrid resonance is dependent on the thickness of the AZO layer on the fiber. The fiber samples with the thicker ENZ layers exhibit a larger refractive index response with higher sensitivity. Therefore, the reported refractive index response of the hybrid ENZ resonance for potential sensing applications can be further optimized by choosing the geometric parameters and material properties of the configuration. Rigorous optimization of the ENZ layer thickness, the separation between the core and the ENZ layer, the length of the side-polished part, and the dispersion of the AZO thin layer could further enhance the sensing performance.

To study the dependence of the external refractive index response of the ENZ mode on the thickness of the AZO layer, we performed simulations by varying the thickness of the AZO layer in the air (Figure 5-12a) and in the water (Figure 5-12b), respectively.

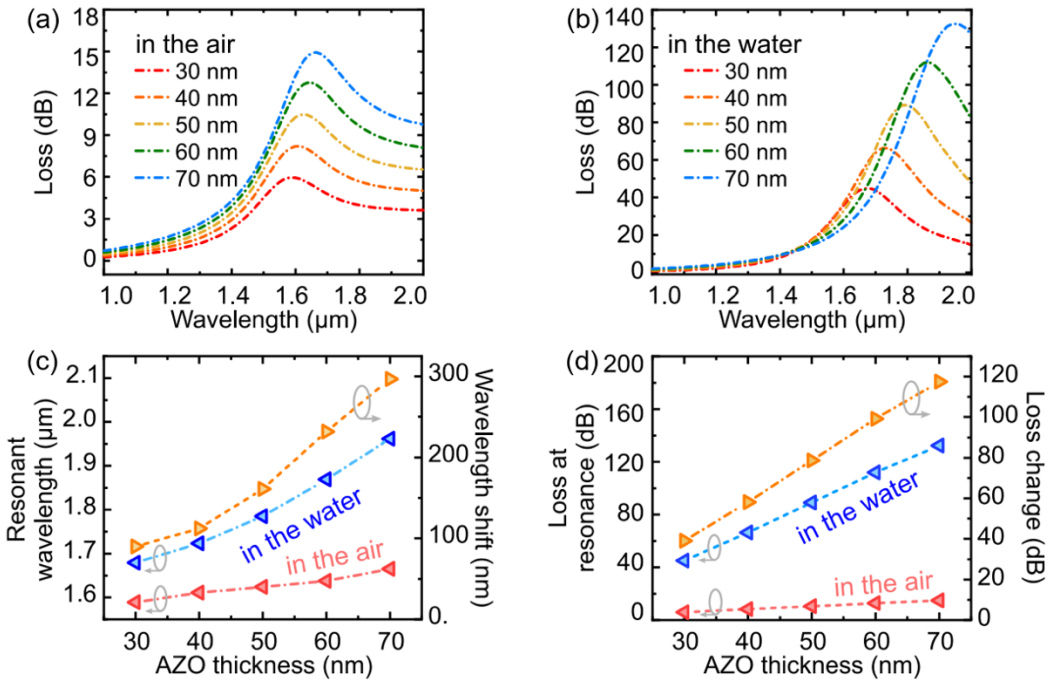

Figure 5-12 Simulated fundamental modal loss spectra of ENZ D-shaped fiber with the thickness of AZO layer varying from 30 nm to 70 nm **(a)** in the air and **(b)** in the water. **(c)** Dependence of resonance wavelength and resonance loss for air (n = 1.0) (red triangles) and DI water (n = 1.3) (blue triangles) with the AZO thickness of the ENZ D-shaped fiber and their corresponding total shift of the resonance wavelength and change of resonance loss magnitude (orange triangles).

The complex permittivity of the AZO thin film for all thicknesses is assumed to be the same as the permittivity of AZO-30. The resonance wavelength of the ENZ mode redshifts from 1589 nm to 1665 nm with thickness of AZO layer varying from 30 nm to 70 nm in the air (red triangles in Figure 5-12c). The loss at ENZ resonance changes from 6 dB to 15 dB (red triangles in Figure 5-12d). For the case in water, the resonance wavelength shifts from 1679 nm to 1961 nm (blue triangles in Figure 5-12c). The loss at ENZ resonance increases from 45 dB to 117 dB (blue triangles in Figure 5-12d). The shift of resonance wavelength and resonance strength loss from air to water for different AZO thicknesses are plotted in the orange data in Figure 5-12c and 12d, respectively. With thicker ENZ layers, the AZO-

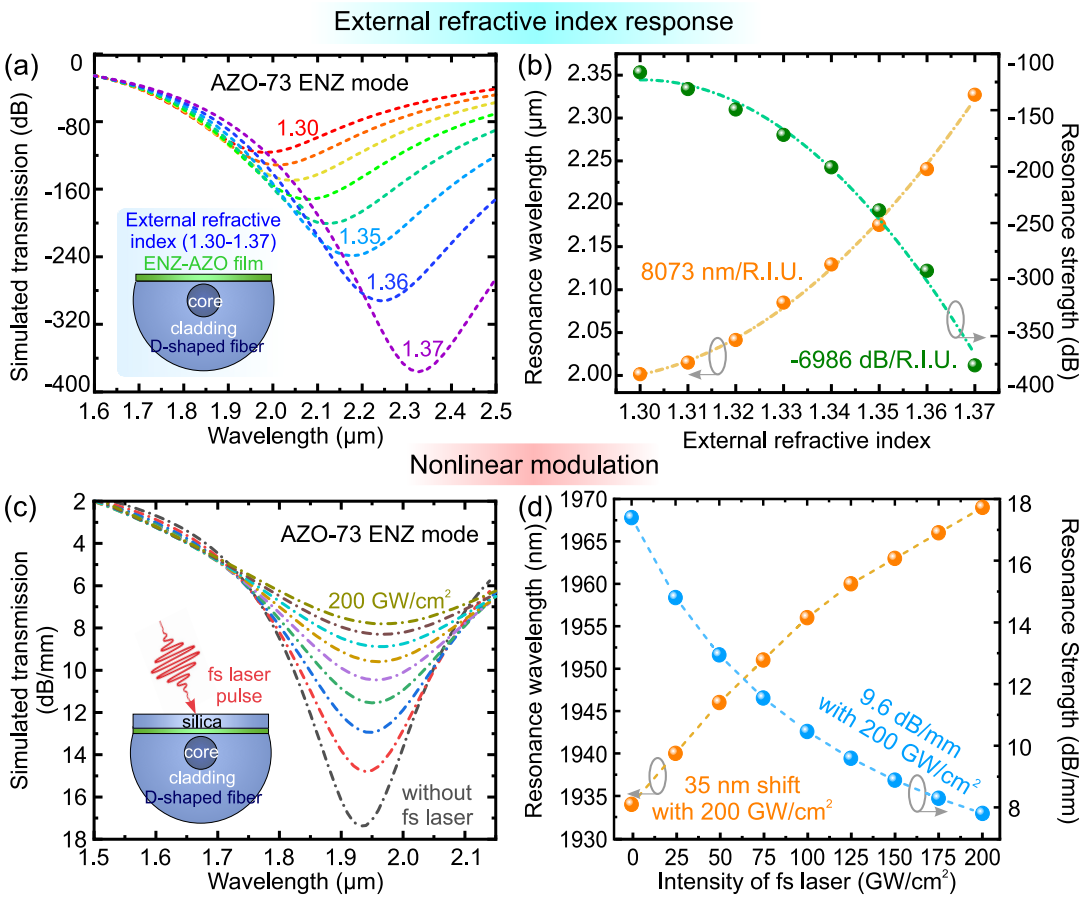

Figure 5-13 External refractive index response and nonlinear modulation of the ENZ mode in the D-shaped fiber. **(a)** Simulated transmission of the ENZ mode on the AZO-73 immersed in various refractive index liquids (length = 1.7 cm). **(b)** Resonance wavelength and resonance strength of the ENZ mode versus external refractive index. **(c)** Simulated transmission, **(d)** resonance wavelength and resonance strength of the ENZ mode on glass-covered AZO-73 versus the intensity of femtosecond laser pulse.

coated D-shaped fiber exhibits larger response on external refractive index in both resonance wavelength and the magnitude of the resonance strength.

We further investigated the nonlinear modulation of the hybrid ENZ resonance for potential ultrafast in-fiber optical switching. To enhance the electric field confinement, a 300-nm silica glass layer was introduced onto the AZO-73 sample as shown in the inset of Figure 5-13c. Using the experimentally obtained nonlinear refractive index n_2 of 2.9×10^{-16}

m^2/W and nonlinear absorption β_2 of -1.3×10^{-9} m/W of the fabricated AZO layer [*170*], we numerically simulated the nonlinear optical response of the hybrid ENZ resonance. Figure 5-13c shows the ENZ resonance evolution with various intensities of a femtosecond laser pulse. Due to the large nonlinearity [*70, 153*] and strong field confinement [*76*] of the ENZ layer, the resonance wavelength of the ENZ mode redshifts by 35 nm and a large modulation of the resonance strength by ~9.6 dB/mm were obtained under the femtosecond laser excitation with intensity of 200 GW/cm^2 (Figure 5-13d), showing the unique potential on developing an in-fiber optical switch with low energy consumption and ultrafast response.

5.4 Summary

We demonstrate the excitation of the hybrid ENZ mode in a D-shaped optical fiber coated with an ultrathin AZO layer, which has a real part of permittivity crossing zero in the near-infrared wavelength regime. The experimental ENZ resonance has a strong resonance strength of ~25 dB, which agrees with the full-wave electromagnetic simulation. The ENZ resonance resulted from the phase matching between the fundamental fiber mode and the ENZ mode supported by the thin AZO layer. The hybrid ENZ mode excited on the optical fiber platform exhibits a relatively large light-matter interaction length (*i.e.,* propagation length), controllable coupling strength, and simplified ENZ excitation method that can be envisioned for next-generation in-fiber devices for novel zero-index photonics applications. We also show the proof-of-concept tunability of the hybrid resonance by the external refractive index or the large nonlinearity of the ENZ thin-film. In particular, the hybrid ENZ resonance in the optical fiber could also be potentially tuned by fabricating a metal-oxide-semiconductor (TCO) gate structure due to the electrically tunable permittivity of the AZO

films as discussed in Chapters 2 and 4[*52, 69, 148*]. The gate-tunable ENZ-fiber will allow for compact in-fiber electrically tunable filters and modulators. This property may open a new pathway toward compact in-fiber devices, which could find potential applications, such as nonlinear optics, in-fiber lasing, and gas or biomolecule sensing.

Chapter 6 Conclusion and Outlook

In recent years, the emergence of metasurfaces and zero-index photonics has attracted a lot of attention and has been extensively studied. The initial incentive is to replace the bulky optical components with thinner and lighter alternatives and to achieve novel optical properties that could not be realized in conventional components. The integration of metasurfaces and zero-index photonics on the optical fiber platform provides access to compact in-fiber photonic devices with unique properties. The opportunities of metasurfaces and zero-index photonics are pronounced particularly in optical fiber platforms, which is the objective of this dissertation.

Chapter 2 begins with a theoretical discussion on the basic properties of optical fiber and the fundamental analysis of metasurfaces followed by a flow chat of conventional metasurfaces design. By leveraging the gate-tunable heterostructure, metasurfaces have been evolved from passive structures toward integrated active devices. We also discuss the dynamic mechanism of field effect for gate-tunable metasurfaces and the coupling mechanism of epsilon-near-zero mode in optical fibers.

Chapter 3 reports on an ultrathin optical metalens directly patterned on the facet of a photonic crystal fiber that enables light convergence in telecommunication wavelengths. In-fiber metalens with designed focal length at a wavelength of 1550 nm is demonstrated with an operating efficiency of 16%. The ultrathin optical fiber metalens may find novel applications in optical imaging, sensing, and fiber lasers.

Chapter 4 presents a gate-tunable plasmonic optical filter incorporating a patterned metal-insulator-metal heterostructure as a proof-of-concept of the active metasurface. An

additional thin transparent conducting oxide layer is embedded in the insulator layer to form a double metal–oxide-semiconductor configuration, which can be electrically tuned by the formation of two thin accumulation layers at the interfaces of the indium tin oxides and insulator. The modulation strength and transmission peak shift increase dramatically compared to single gate structure. This study reveals an essential step toward the realization of active photonic integrated devices with large tunability.

Chapter 5 demonstrates the experimental excitation of a highly confined epsilon-near-zero (ENZ) mode in a side-polished optical fiber coated with a deep subwavelength thick layer of aluminum-doped zinc oxide (AZO). The uniform AZO layer on the fiber was fabricated by the atomic layer deposition technique and optimized to exhibit close-to-zero permittivity at the near-infrared wavelength. Polarization- and wavelength-dependent transmission with strong resonance strength is observed. The hybrid ENZ mode in optical fiber can be excited simply by direct phase matching between the fundamental mode of the fiber and the thin film ENZ mode. The hybrid ENZ mode in the fiber exhibits a relatively long propagation length in the range of centimeter, which is a few orders of magnitude longer than those on the planar ENZ substrates. The hybrid resonance in the ENZ fiber can also be actively tuned through the external refractive index and the large nonlinearity of the ENZ film. These ENZ-optical fibers have the potential to serve as emerging optical platforms for developing compact in-fiber devices, such as advanced in-fiber ultrafast optical switches, modulators, optical filters, mode-locked fiber lasers, and in-fiber optical gas or biomolecule sensors.

The results of this dissertation indicate the accessibility of active in-fiber devices with compactness and unique optical properties. While developing these optical fiber

components, we are learning about their strengths and limitations for practical applications. The motivation behind the integration of metasurfaces and zero-index photonics with optical fiber is not only to replace the conventional bulky optical components with these compact structures, but also to explore extraordinary properties and large tunability for emerging in-fiber applications. The following outlook highlights several potential avenues for future explorations, including in-fiber metalens or metasurfaces with high efficiency, the nanofabrication techniques of metasurfaces on optical fibers, active metasurfaces with large tunability, efficient vortex generation and mode-lock laser based on ENZ optical fibers.

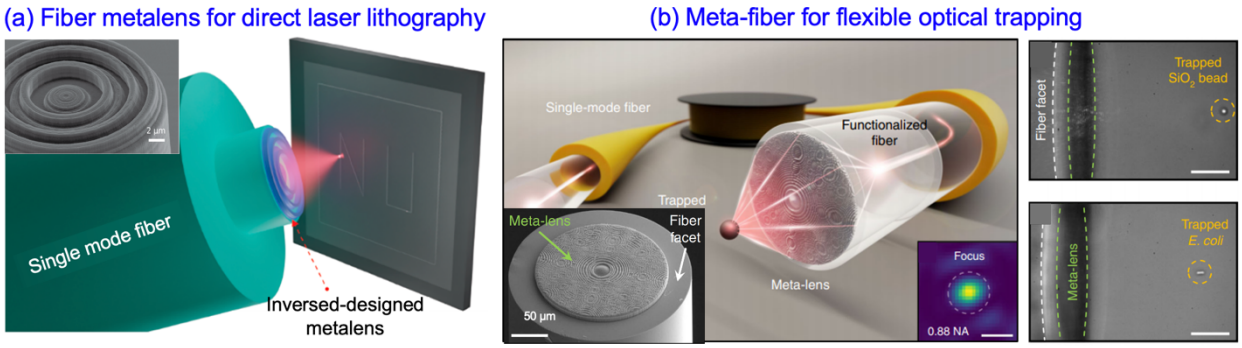

Figure 6-1 (a) Inverse design and 3D printing of a fiber metalens for direct laser lithography [*171*]. **(b)** Ultrahigh numerical aperture meta-fiber for optical trapping [*172*].

(1) Efficient in-fiber metalens and metasurfaces: The measured efficiency of photonic crystal fiber metalens is 16% due to the intrinsic loss of plasmonic metasurface (Chapter 3). The performance of fiber metalens can be further improved with low-loss materials. Recently, Hadibrata *et al*. optimized the performance of fiber metalens by inverse design method (Figure 6-1a) [*171*]. The transmission efficiency of the single polymer metalens fabricated by two photon direct laser writing is as high as 73% with numerical aperture of 0.85 at a wavelength of 980 nm in the air. Particularly, the proposed fiber metalens could be

fabricated precisely with direct laser lithography with fine resolution of 200 nm. Further, Plidschun *et al*. reported a meta-fiber with higher numerical aperture of 0.88 at a wavelength of 660 nm in water environment (Figure 6-1b) [*172*]. The nanorods, with a varying height of up to 3 μm implemented by femtosecond direct laser writing, enable a directly patterned metalens onto a fiber end facet with transmission efficiency of larger than 50%. By witnessing the progress in the efficiency of fiber metalens with polymer, we expect the improvement of performance for fiber metalens. For instance, we simulated that the efficiency of fiber metalens can increase dramatically to about 91% at a wavelength of 1550 nm by utilizing optimized silicon nanoblocks. We envision that the performance of in-fiber metasurfaces can be further improved by using low-loss materials and powerful design approaches, such as inverse design and machine learning.

(2) Nanofabrication of metasurfaces on optical fibers: The focused ion beam milling nanofabrication technique used to develop plasmonic metasurfaces (Chapter 3) is not sufficient and precise enough to integrate metasurfaces with dielectric materials because of the high aspect ratio of the nanostructures. It is necessary to explore advanced nanofabrication methods on optical fiber platform to achieve precise element features. Recent studies show that laser direct writing technique can be employed to fabricate polymer nano blocks on optical fibers, which has been utilized to demonstrate fiber metalens with higher efficiency. However, the polymer for laser printing has a smaller refractive index compared to dielectric materials (*e.g.,* silicon and titanium dioxide), which leads to taller unit elements to achieve similar amplitude and phase changes. Besides, laser writing has difficulties in reaching high resolution less than 300-400nm, which is critical for metasurfaces. Recent studies demonstrated that modified electron beam lithography with

resolution in nanometer can be used to realize plasmonic fiber metalens for remote focusing (Figure 6-2) [*88, 173*]. Therefore, e-beam lithography shows the promise to fabricate high quality metasurfaces on optical fiber platforms with the potential of large-scale manufacturing. The further exploration of novel materials and nanofabrication techniques will extend the application of in-fiber metasurface devices, such as generation of sophisticated beam profiles such as high order vortex generation and flexible optical trapping, *etc*.

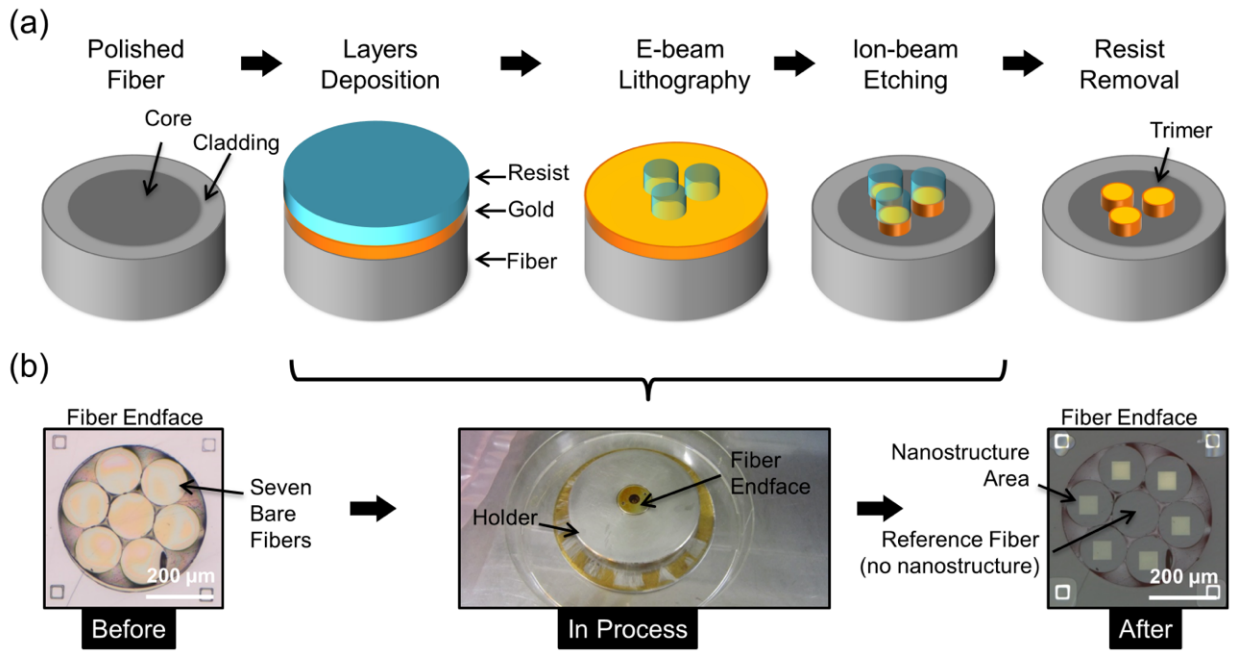

Figure 6-2 Electron beam lithography on the planarized sample that contains a bundle of seven standard single mode fibers [*88*]. (a) Workflow of the nanostructure fabrication process. **(b)** Corresponding status of the sample for different steps.

(3) Active metasurfaces with large tunability: Electrically tunable conducting oxide metasurfaces (Chapter 4) exhibits the advantage of a large gate-tunable refractive index modulation within the Debye length of the accumulation or depletion layer, which can lead to large optical phase modulation (less than 300°) in reflection [*156*]. In addition, they could

provide high operation speed (more than 10 GHz) and low power consumption (about 2.5 fJ/bit). Since the conducting oxide materials are CMOS technology compatible, they have a great potential for developing compact and integrable flat in-fiber devices. The disadvantages of this tunable mechanism are that they exhibit low efficiency (less than 40%), large phase modulation only in reflection, and they are not accessible in the visible wavelengths. In the past ten years, many other attempts have been made to develop active optical metasurfaces based on a variety of tunable mechanisms. These proposed active metasurfaces show promise for tunability, but significant challenges remain. Most of the reported active metasurfaces are "proof-of-concept" demonstrations lack of significant integration into device-level applications. We expect significant progress in application development with a wealth of unique physical properties from novel materials, such as two-dimensional materials, perovskite, and lithium niobate, *etc*.

There are a variety of possible advanced developments of novel and active in-fiber devices based on the integration of metasurfaces and zero-index photonics with fiber optics. These integrations aim not only to simply replace the bulky optical components with flat-optics alternatives, but also to explore the physics behind and extend the novel functionalities and practical applications. The outlook of novel in-fiber photonic devices is only limited by our creativity and imagination and "there is plenty of room at the bottom" so says Dr. Richard Feynman.

Bibliography

[1] K. C. Kao, G. A. Hockham, in *Proceedings of the Institution of Electrical Engineers*. (IET, 1966), vol. 113, pp. 1151-1158.

[2] A. Chong, J. Buckley, W. Renninger, F. Wise, All-normal-dispersion femtosecond fiber laser. *Optics Express* **14**, 10095-10100 (2006).

[3] Y. e. Jeong, J. Sahu, D. Payne, J. Nilsson, Ytterbium-doped large-core fiber laser with 1.36 kW continuous-wave output power. *Optics Express* **12**, 6088-6092 (2004).

[4] J. Andrade, R. Vanwagenen, D. Gregonis, K. Newby, J.-N. Lin, Remote fiber-optic biosensors based on evanescent-excited fluoro-immunoassay: concept and progress. *IEEE Transactions on Electron Devices* **32**, 1175-1179 (1985).

[5] M. W. Katoot. (Google Patents, 2000).

[6] I. N. Papadopoulos, S. Farahi, C. Moser, D. Psaltis, High-resolution, lensless endoscope based on digital scanning through a multimode optical fiber. *Biomedical Optics Express* **4**, 260-270 (2013).

[7] N. M. Fried, K. E. Murray, High-power thulium fiber laser ablation of urinary tissues at 1.94 μm. *Journal of Endourology* **19**, 25-31 (2005).

[8] T. S. Alster, E. L. Tanzi, M. Lazarus, The use of fractional laser photothermolysis for the treatment of atrophic scars. *Dermatologic Surgery* **33**, 295-299 (2007).

[9] N. Yu, P. Genevet, M. A. Kats, F. Aieta, J.-P. Tetienne, F. Capasso, Z. Gaburro, Light propagation with phase discontinuities: generalized laws of reflection and refraction. *Science* **334**, 333-337 (2011).

[10] N. Yu, F. Capasso, Flat optics with designer metasurfaces. *Nature Materials* **13**, 139-150 (2014).

[11] A. V. Kildishev, A. Boltasseva, V. M. Shalaev, Planar photonics with metasurfaces. *Science* **339**, 1232009 (2013).

[12] N. Meinzer, W. L. Barnes, I. R. Hooper, Plasmonic meta-atoms and metasurfaces. *Nature Photonics* **8**, 889-898 (2014).

[13] F. Aieta, P. Genevet, M. A. Kats, N. Yu, R. Blanchard, Z. Gaburro, F. Capasso, Aberration-free ultrathin flat lenses and axicons at telecom wavelengths based on plasmonic metasurfaces. *Nano Letters* **12**, 4932-4936 (2012).

[14] M. Kang, T. Feng, H.-T. Wang, J. Li, Wave front engineering from an array of thin aperture antennas. *Optics Express* **20**, 15882-15890 (2012).

[15] M. Khorasaninejad, W. T. Chen, R. C. Devlin, J. Oh, A. Y. Zhu, F. Capasso, Metalenses at visible wavelengths: Diffraction-limited focusing and subwavelength resolution imaging. *Science* **352**, 1190-1194 (2016).

[16] P. Genevet, N. Yu, F. Aieta, J. Lin, M. A. Kats, R. Blanchard, M. O. Scully, Z. Gaburro, F. Capasso, Ultra-thin plasmonic optical vortex plate based on phase discontinuities. *Applied Physics Letters* **100**, 013101 (2012).

[17] K.-Y. Yang, C.-M. Wang, Y.-W. Huang, G. Sun, I.-D. Chiang, C. Y. Liao, W.-L. Hsu, H. T. Lin, S. Sun, L. Zhou, A. Q. Liu, D. P. Tsai, High-efficiency broadband meta-hologram with polarization-controlled dual images. *Nano Letters* **14**, 225-230 (2014).

[18] X. Ni, A. V. Kildishev, V. M. Shalaev, Metasurface holograms for visible light. *Nature Communications* **4**, 1-6 (2013).

[19] G. Zheng, H. Muhlenbernd, M. Kenney, G. Li, T. Zentgraf, S. Zhang, Metasurface holograms reaching 80% efficiency. *Nature Nanotechnology* **10**, 308-312 (2015).

[20] P. Genevet, F. Capasso, Holographic optical metasurfaces: a review of current progress. *Reports on Progress in Physics* **78**, 024401 (2015).

[21] Y.-W. Huang, W. T. Chen, W.-Y. Tsai, P. C. Wu, C.-M. Wang, G. Sun, D. P. Tsai, Aluminum plasmonic multicolor meta-hologram. *Nano Letters* **15**, 3122-3127 (2015).

[22] Y. Hu, X. Luo, Y. Chen, Q. Liu, X. Li, Y. Wang, N. Liu, H. Duan, 3D-integrated metasurfaces for full-colour holography. *Light: Science & Applications* **8**, 86 (2019).

[23] J. Lin, J. P. B. Mueller, Q. Wang, G. Yuan, N. Antoniou, X.-C. Yuan, F. Capasso, Polarization-controlled tunable directional coupling of surface plasmon polaritons. *Science* **340**, 331-334 (2013).

[24] J. Jin, J. Luo, X. Zhang, H. Gao, X. Li, M. Pu, P. Gao, Z. Zhao, X. Luo, Generation and detection of orbital angular momentum via metasurface. *Scientific Reports* **6**, 24286 (2016).

[25] G. Li, M. Kang, S. Chen, S. Zhang, E. Y.-B. Pun, K. W. Cheah, J. Li, Spin-enabled plasmonic metasurfaces for manipulating orbital angular momentum of light. *Nano Letters* **13**, 4148-4151 (2013).

[26] E. Karimi, S. A. Schulz, I. De Leon, H. Qassim, J. Upham, R. W. Boyd, Generating optical orbital angular momentum at visible wavelengths using a plasmonic metasurface. *Light: Science & Applications* **3**, e167 (2014).

[27] R. C. Devlin, A. Ambrosio, N. A. Rubin, J. B. Mueller, F. Capasso, Arbitrary spin-to–orbital angular momentum conversion of light. *Science* **358**, 896-901 (2017).

[28] I. Liberal, N. Engheta, Near-zero refractive index photonics. *Nature Photonics* **11**, 149 (2017).

[29] N. Kinsey, C. Devault, A. Boltasseva, V. M. Shalaev, Near-zero-index materials for photonics. *Nature Reviews Materials* **4**, 1-19 (2019).

[30] M. Silveirinha, N. Engheta, Tunneling of electromagnetic energy through subwavelength channels and bends using ε-near-zero materials. *Physical Review Letters* **97**, 157403 (2006).

[31] I. Liberal, N. Engheta, Nonradiating and radiating modes excited by quantum emitters in open epsilon-near-zero cavities. *Science Advances* **2**, e1600987 (2016).

[32] X. Liu, K. Zang, J.-H. Kang, J. Park, J. S. Harris, P. G. Kik, M. L. Brongersma, Epsilon-near-zero Si slot-waveguide modulator. *ACS Photonics* **5**, 4484-4490 (2018).

[33] A. R. Davoyan, A. M. Mahmoud, N. Engheta, Optical isolation with epsilon-near-zero metamaterials. *Optics Express* **21**, 3279-3286 (2013).

[34] P. Moitra, Y. Yang, Z. Anderson, I. I. Kravchenko, D. P. Briggs, J. Valentine, Realization of an all-dielectric zero-index optical metamaterial. *Nature Photonics* **7**, 791 (2013).

[35] Y.-J. Lu, R. Sokhoyan, W.-H. Cheng, G. K. Shirmanesh, A. R. Davoyan, R. A. Pala, K. Thyagarajan, H. A. Atwater, Dynamically controlled Purcell enhancement of visible spontaneous emission in a gated plasmonic heterostructure. *Nature Communications* **8**, 1631 (2017).

[36] A. D. Neira, G. A. Wurtz, A. V. Zayats, All-optical switching in silicon photonic waveguides with an epsilon-near-zero resonant cavity. *Photonics Research* **6**, B1-B5 (2018).

[37] O. Reshef, I. De Leon, M. Z. Alam, R. W. Boyd, Nonlinear optical effects in epsilon-near-zero media. *Nature Reviews Materials* **4**, 535-551 (2019).

[38] Y. Yang, J. Lu, A. Manjavacas, T. S. Luk, H. Liu, K. Kelley, J.-P. Maria, E. L. Runnerstrom, M. B. Sinclair, S. Ghimire, High-harmonic generation from an epsilon-near-zero material. *Nature Physics* **15**, 1022-1026 (2019).

[39] K. Minn, A. Anopchenko, J. Yang, H. W. H. Lee, Excitation of epsilon-near-zero resonance in ultra-thin indium tin oxide shell embedded nanostructured optical fiber. *Scientific Reports* **8**, 2342 (2018).

[40] G. P. Agrawal, in *Nonlinear Science at the Dawn of the 21st Century*. (Springer, 2000), pp. 195-211.

[41] J. Wilde, C. Schulze, R. Brüning, M. Duparré, S. Schröter, in *Laser Resonators, Microresonators, and Beam Control XVII*. (International Society for Optics and Photonics, 2015), vol. 9343, pp. 93431P.

[42] X. Ni, N. K. Emani, A. V. Kildishev, A. Boltasseva, V. M. Shalaev, Broadband light bending with plasmonic nanoantennas. *Science* **335**, 427-427 (2012).

[43] S. Sun, K.-Y. Yang, C.-M. Wang, T.-K. Juan, W. T. Chen, C. Y. Liao, Q. He, S. Xiao, W.-T. Kung, G.-Y. Guo, High-efficiency broadband anomalous reflection by gradient meta-surfaces. *Nano Letters* **12**, 6223-6229 (2012).

[44] H. H. Hsiao, C. H. Chu, D. P. Tsai, Fundamentals and applications of metasurfaces. *Small Methods* **1**, 1600064 (2017).

[45] K. E. Chong, I. Staude, A. James, J. Dominguez, S. Liu, S. Campione, G. S. Subramania, T. S. Luk, M. Decker, D. N. Neshev, I. Brener, Y. S. Kivshar, Polarization-independent silicon metadevices for efficient optical wavefront control. *Nano Letters* **15**, 5369-5374 (2015).

[46] S. M. Kamali, A. Arbabi, E. Arbabi, Y. Horie, A. Faraon, Decoupling optical function and geometrical form using conformal flexible dielectric metasurfaces. *Nature Communications* **7**, 11618 (2016).

[47] M. Khorasaninejad, A. Y. Zhu, C. Roques-Carmes, W. T. Chen, J. Oh, I. Mishra, R. C. Devlin, F. Capasso, Polarization-insensitive metalenses at visible wavelengths. *Nano Letters* **16**, 7229-7234 (2016).

[48] P. C. Wu, W.-Y. Tsai, W. T. Chen, Y.-W. Huang, T.-Y. Chen, J.-W. Chen, C. Y. Liao, C. H. Chu, G. Sun, D. P. Tsai, Versatile polarization generation with an aluminum plasmonic metasurface. *Nano Letters* **17**, 445-452 (2017).

[49] G. V. Naik, V. M. Shalaev, A. Boltasseva, Alternative plasmonic materials: beyond gold and silver. *Advanced Materials* **25**, 3264-3294 (2013).

[50] A. Boltasseva, H. A. Atwater, Low-loss plasmonic metamaterials. *Science* **331**, 290-291 (2011).

[51] G. V. Naik, J. Kim, A. Boltasseva, Oxides and nitrides as alternative plasmonic materials in the optical range. *Optical Materials Express* **1**, 1090-1099 (2011).

[52] H. W. Lee, G. Papadakis, S. P. Burgos, K. Chander, A. Kriesch, R. Pala, U. Peschel, H. A. Atwater, Nanoscale conducting oxide PlasMOStor. *Nano Letters* **14**, 6463-6468 (2014).

[53] A. Anopchenko, S. Gurung, L. Tao, C. Arndt, H. W. H. Lee, Atomic layer deposition of ultra-thin and smooth Al-doped ZnO for zero-index photonics. *Materials Research Express* **5**, 014012 (2018).

[54] S. Q. Li, P. Guo, L. Zhang, W. Zhou, T. W. Odom, T. Seideman, J. B. Ketterson, R. P. H. Chang, Infrared plasmonics with indium-tin-oxide nanorod arrays. *ACS Nano* **5**, 9161-9170 (2011).

[55] U. Guler, G. V. Naik, A. Boltasseva, V. M. Shalaev, A. V. Kildishev, Performance analysis of nitride alternative plasmonic materials for localized surface plasmon applications. *Applied Physics B* **107**, 285-291 (2012).

[56] L. Dominici, F. Michelotti, T. M. Brown, A. Reale, A. Di Carlo, Plasmon polaritons in the near infrared on fluorine doped tin oxide films. *Optics Express* **17**, 10155-10167 (2009).

[57] S. Franzen, C. Rhodes, M. Cerruti, R. W. Gerber, M. Losego, J.-P. Maria, D. E. Aspnes, Plasmonic phenomena in indium tin oxide and ITO-Au hybrid films. *Optics Letters* **34**, 2867-2869 (2009).

[58] K. Jongbum, G. V. Naik, N. K. Emani, U. Guler, A. Boltasseva, Plasmonic resonances in nanostructured transparent conducting oxide films. *IEEE Journal of Selected Topics in Quantum Electronics* **19**, 4601907 (2013).

[59] X. Liu, J. Park, J.-H. Kang, H. Yuan, Y. Cui, H. Y. Hwang, M. L. Brongersma, Quantification and impact of nonparabolicity of the conduction band of indium tin oxide on its plasmonic properties. *Applied Physics Letters* **105**, 181117 (2014).

[60] P. R. West, S. Ishii, G. V. Naik, N. K. Emani, V. M. Shalaev, A. Boltasseva, Searching for better plasmonic materials. *Laser & Photonics Reviews* **4**, 795-808 (2010).

[61] R. K. Verma, B. D. Gupta, Surface plasmon resonance based fiber optic sensor for the IR region using a conducting metal oxide film. *Journal of the Optical Society of America A* **27**, 846-851 (2010).

[62] C. Rhodes, S. Franzen, J.-P. Maria, M. Losego, D. N. Leonard, B. Laughlin, G. Duscher, S. Weibel, Surface plasmon resonance in conducting metal oxides. *Journal of Applied Physics* **100**, 054905 (2006).

[63] F. Michelotti, L. Dominici, E. Descrovi, N. Danz, F. Menchini, Thickness dependence of surface plasmon polariton dispersion in transparent conducting oxide films at 1.55 microm. *Optics Letters* **34**, 839-841 (2009).

[64] M. Abb, B. Sepúlveda, H. M. H. Chong, O. L. Muskens, Transparent conducting oxides for active hybrid metamaterial devices. *Journal of Optics* **14**, 114007 (2012).

[65] M. A. Noginov, L. Gu, J. Livenere, G. Zhu, A. K. Pradhan, R. Mundle, M. Bahoura, Y. A. Barnakov, V. A. Podolskiy, Transparent conductive oxides: Plasmonic materials for telecom wavelengths. *Applied Physics Letters* **99**, 021101 (2011).

[66] R. Buonsanti, A. Llordes, S. Aloni, B. A. Helms, D. J. Milliron, Tunable infrared absorption and visible transparency of colloidal aluminum-doped zinc oxide nanocrystals. *Nano Letters* **11**, 4706-4710 (2011).

[67] D. Traviss, R. Bruck, B. Mills, M. Abb, O. L. Muskens, Ultrafast plasmonics using transparent conductive oxide hybrids in the epsilon-near-zero regime. *Applied Physics Letters* **102**, 121112 (2013).

[68] A. Calzolari, A. Ruini, A. Catellani, Transparent conductive oxides as near-IR plasmonic materials: The case of Al-doped ZnO derivatives. *ACS Photonics* **1**, 703-709 (2014).

[69] Y.-W. Huang, H. W. H. Lee, R. Sokhoyan, R. A. Pala, K. Thyagarajan, S. Han, D. P. Tsai, H. A. Atwater, Gate-tunable conducting oxide metasurfaces. *Nano Letters* **16**, 5319-5325 (2016).

[70] M. Z. Alam, I. De Leon, R. W. Boyd, Large optical nonlinearity of indium tin oxide in its epsilon-near-zero region. *Science* **352**, 795-797 (2016).

[71] J. Kim, A. Dutta, G. V. Naik, A. J. Giles, F. J. Bezares, C. T. Ellis, J. G. Tischler, A. M. Mahmoud, H. Caglayan, O. J. Glembocki, Role of epsilon-near-zero substrates in the optical response of plasmonic antennas. *Optica* **3**, 339-346 (2016).

[72] A. Alù, M. G. Silveirinha, A. Salandrino, N. Engheta, Epsilon-near-zero metamaterials and electromagnetic sources: Tailoring the radiation phase pattern. *Physical Review B* **75**, 155410 (2007).

[73] A. P. Vasudev, J.-H. Kang, J. Park, X. Liu, M. L. Brongersma, Electro-optical modulation of a silicon waveguide with an "epsilon-near-zero" material. *Optics Express* **21**, 26387-26397 (2013).

[74] L. Zhaolin, Z. Wangshi, S. Kaifeng, Ultracompact electroabsorption modulators based on tunable epsilon-near-zero-slot waveguides. *IEEE Photonics Journal* **4**, 735-740 (2012).

[75] M. G. Wood, S. Campione, S. Parameswaran, T. S. Luk, J. R. Wendt, D. K. Serkland, G. A. Keeler, Gigahertz speed operation of epsilon-near-zero silicon photonic modulators. *Optica* **5**, 233-236 (2018).

[76] S. Campione, I. Brener, F. Marquier, Theory of epsilon-near-zero modes in ultrathin films. *Physical Review B* **91**, 121408 (2015).

[77] M. H. Javani, M. I. Stockman, Real and imaginary properties of epsilon-near-zero materials. *Physical Review Letters* **117**, 107404 (2016).

[78] B. Edwards, A. Alù, M. E. Young, M. Silveirinha, N. Engheta, Experimental verification of epsilon-near-zero metamaterial coupling and energy squeezing using a microwave waveguide. *Physical Review Letters* **100**, 033903 (2008).

[79] I. Liberal, N. Engheta, The rise of near-zero-index technologies. *Science* **358**, 1540-1541 (2017).

[80] A. Ciattoni, A. Marini, C. Rizza, Efficient vortex generation in subwavelength epsilon-near-zero slabs. *Physical Review Letters* **118**, 104301 (2017).

[81] S. Saha, B. T. Diroll, J. Shank, Z. Kudyshev, A. Dutta, S. N. Chowdhury, T. S. Luk, S. Campione, R. D. Schaller, V. M. Shalaev, Broadband, high-speed, and large-amplitude dynamic optical switching with yttrium-doped cadmium oxide. *Advanced Functional Materials*, 1908377 (2019).

[82] H. Raether, Surface-Plasmons on Smooth and Rough Surfaces and on Gratings. *Springer Tracts in Modern Physics* **111**, 1-133 (1988).

[83] S. Campione, I. Kim, D. d. Ceglia, G. A. Keeler, a. T. S. Luk, Experimental verification of epsilon-near-zero plasmon polariton modes in degenerately doped semiconductor nanolayers. *Optics Express* **24**, 18782-18789 (2016).

[84] J. Yang, I. Ghimire, P. C. Wu, S. Gurung, C. Arndt, D. P. Tsai, H. W. H. Lee, Photonic crystal fiber metalens. *Nanophotonics* **8**, 443-449 (2019).

[85] H. Kim, H. An, J. Kim, S. Lee, K. Park, S. Lee, S. Hong, L. A. Vazquez-Zuniga, S.-Y. Lee, B. Lee, Corrugation-assisted metal-coated angled fiber facet for wavelength-dependent off-axis directional beaming. *Optics Express* **25**, 8366-8385 (2017).

[86] V. Savinov, N. I. Zheludev, High-quality metamaterial dispersive grating on the facet of an optical fiber. *Applied Physics Letters* **111**, 091106 (2017).

[87] H. E. Arabi, H.-E. Joe, T. Nazari, B.-K. Min, K. Oh, A high throughput supra-wavelength plasmonic bull's eye photon sorter spatially and spectrally multiplexed on silica optical fiber facet. *Optics Express* **21**, 28083-28094 (2013).

[88] N. Wang, M. Zeisberger, U. Hubner, M. A. Schmidt, Nanotrimer enhanced optical fiber tips implemented by electron beam lithography. *Optical Materials Express* **8**, 2246-2255 (2018).

[89] A. A. Saleh, S. Sheikhoelislami, S. Gastelum, J. A. Dionne, Grating-flanked plasmonic coaxial apertures for efficient fiber optical tweezers. *Optics Express* **24**, 20593-20603 (2016).

[90] P. Jia, J. Yang, A plasmonic optical fiber patterned by template transfer as a high-performance flexible nanoprobe for real-time biosensing. *Nanoscale* **6**, 8836-8843 (2014).

[91] P. Jia, J. Yang, Integration of large-area metallic nanohole arrays with multimode optical fibers for surface plasmon resonance sensing. *Applied Physics Letters* **102**, 243107 (2013).

[92] Z. Zhang, Y. Chen, H. Liu, H. Bae, D. A. Olson, A. K. Gupta, M. Yu, On-fiber plasmonic interferometer for multi-parameter sensing. *Optics Express* **23**, 10732-10740 (2015).

[93] P. Reader-Harris, A. Di Falco, Nanoplasmonic filters for hollow core photonic crystal fibers. *ACS Photonics* **1**, 985-989 (2014).

[94] Y. Liu, H. Xu, F. Stief, N. Zhitenev, M. Yu, Far-field superfocusing with an optical fiber based surface plasmonic lens made of nanoscale concentric annular slits. *Optics Express* **19**, 20233-20243 (2011).

[95] A. Koshelev, G. Calafiore, C. Piña-Hernandez, F. I. Allen, S. Dhuey, S. Sassolini, E. Wong, P. Lum, K. Munechika, S. Cabrini, High refractive index Fresnel lens on a fiber fabricated by nanoimprint lithography for immersion applications. *Optics Letters* **41**, 3423-3426 (2016).

[96] G. H. Yuan, E. T. Rogers, N. I. Zheludev, Achromatic super-oscillatory lenses with sub-wavelength focusing. *Light: Science & Applications* **6**, e17036 (2017).

[97] D. Lin, P. Fan, E. Hasman, M. L. Brongersma, Dielectric gradient metasurface optical elements. *Science* **345**, 298-302 (2014).

[98] S. Wang, P. C. Wu, V.-C. Su, Y.-C. Lai, M.-K. Chen, H. Y. Kuo, B. H. Chen, Y. H. Chen, T.-T. Huang, J.-H. Wang, A broadband achromatic metalens in the visible. *Nature Nanotechnology* **13**, 227-232 (2018).

[99] S. Wang, P. C. Wu, V.-C. Su, Y.-C. Lai, C. H. Chu, J.-W. Chen, S.-H. Lu, J. Chen, B. Xu, C.-H. Kuan, Broadband achromatic optical metasurface devices. *Nature Communications* **8**, 187 (2017).

[100] W. T. Chen, A. Y. Zhu, V. Sanjeev, M. Khorasaninejad, Z. Shi, E. Lee, F. Capasso, A broadband achromatic metalens for focusing and imaging in the visible. *Nature Nanotechnology* **13**, 220 (2018).

[101] H. Pahlevaninezhad, M. Khorasaninejad, Y.-W. Huang, Z. Shi, L. P. Hariri, D. C. Adams, V. Ding, A. Zhu, C.-W. Qiu, F. Capasso, M. J. Suter, Nano-optic endoscope for high-resolution optical coherence tomography in vivo. *Nature Photonics*, (2018).

[102] N. Yu, F. Capasso, Optical metasurfaces and prospect of their applications including fiber optics. *Journal of Lightwave Technology* **33**, 2344-2358 (2015).

[103] M. Principe, M. Consales, A. Micco, A. Crescitelli, G. Castaldi, E. Esposito, V. La Ferrara, A. Cutolo, V. Galdi, A. Cusano, Optical fiber meta-tips. *Light: Science & Applications* **6**, e16226 (2017).

[104] P. C. Wu, W.-Y. Tsai, W. T. Chen, Y.-W. Huang, T.-Y. Chen, J.-W. Chen, C. Y. Liao, C. H. Chu, G. Sun, D. P. Tsai, Versatile polarization generation with an aluminum plasmonic metasurface. *Nano Letters* **17**, 445-452 (2016).

[105] T. A. Birks, J. C. Knight, P. S. J. Russell, Endlessly single-mode photonic crystal fiber. *Optics Letters* **22**, 961-963 (1997).

[106] P. Russell, Photonic crystal fibers. *Science* **299**, 358-362 (2003).

[107] S. Wang, P. C. Wu, V.-C. Su, Y.-C. Lai, M.-K. Chen, H. Y. Kuo, B. H. Chen, Y. H. Chen, T.-T. Huang, J.-H. Wang, A broadband achromatic metalens in the visible. *Nature Nanotechnology* **13**, 227 (2018).

[108] X. Chen, L. Huang, H. Mühlenbernd, G. Li, B. Bai, Q. Tan, G. Jin, C.-W. Qiu, S. Zhang, T. Zentgraf, Dual-polarity plasmonic metalens for visible light. *Nature Communications* **3**, 1198 (2012).

[109] T. Shibanuma, S. A. Maier, P. Albella, Polarization control of high transmission/reflection switching by all-dielectric metasurfaces. *Applied Physics Letters* **112**, 063103 (2018).

[110] S. Thiele, K. Arzenbacher, T. Gissibl, H. Giessen, A. M. Herkommer, 3D-printed eagle eye: Compound microlens system for foveated imaging. *Science Advances* **3**, e1602655 (2017).

[111] T. Gissibl, S. Thiele, A. Herkommer, H. Giessen, Two-photon direct laser writing of ultracompact multi-lens objectives. *Nature Photonics* **10**, 554 (2016).

[112] G. Kafaie Shirmanesh, R. Sokhoyan, R. A. Pala, H. A. Atwater, Dual-Gated Active Metasurface at 1550 nm with Wide (> 300°) Phase Tunability. *Nano Letters* **18**, 2957-2963 (2018).

[113] J. Zhang, J. Yang, M. Schell, A. Anopchenko, L. Tao, Z. Yu, H. W. H. Lee, Gate-tunable optical filter based on conducting oxide metasurface heterostructure. *Optics Letters* **44**, 3653-3656 (2019).

[114] M. Khorasaninejad, F. Aieta, P. Kanhaiya, M. A. Kats, P. Genevet, D. Rousso, F. Capasso, Achromatic Metasurface Lens at Telecommunication Wavelengths. *Nano Letters* **15**, 5358-5362 (2015).

[115] Q. Wang, X. Zhang, Y. Xu, Z. Tian, J. Gu, W. Yue, S. Zhang, J. Han, W. Zhang, A Broadband Metasurface-Based Terahertz Flat-Lens Array. *Advanced Optical Materials* **3**, 779-785 (2015).

[116] L. Cong, S. Tan, R. Yahiaoui, F. Yan, W. Zhang, R. Singh, Experimental demonstration of ultrasensitive sensing with terahertz metamaterial absorbers: A comparison with the metasurfaces. *Applied Physics Letters* **106**, 031107 (2015).

[117] L. Xie, W. Gao, J. Shu, Y. Ying, J. Kono, Extraordinary sensitivity enhancement by metasurfaces in terahertz detection of antibiotics. *Scientific Reports* **5**, 8671 (2015).

[118] N. Yu, F. Aieta, P. Genevet, M. A. Kats, Z. Gaburro, F. Capasso, A broadband, background-free quarter-wave plate based on plasmonic metasurfaces. *Nano Letters* **12**, 6328-6333 (2012).

[119] F. Ding, Z. Wang, S. He, V. M. Shalaev, A. V. Kildishev, Broadband High-Efficiency Half-Wave Plate: A Supercell-Based Plasmonic Metasurface Approach. *ACS Nano* **9**, 4111-4119 (2015).

[120] G. Li, M. Kang, S. Chen, S. Zhang, E. Y. Pun, K. W. Cheah, J. Li, Spin-enabled plasmonic metasurfaces for manipulating orbital angular momentum of light. *Nano Letters* **13**, 4148-4151 (2013).

[121] W. Yue, S. Gao, S.-S. Lee, E.-S. Kim, D.-Y. Choi, Highly reflective subtractive color filters capitalizing on a silicon metasurface integrated with nanostructured aluminum mirrors. *Laser & Photonics Reviews* **11**, 1600285 (2017).

[122] O. Wolf, S. Campione, J. Kim, I. Brener, Spectral filtering using active metasurfaces compatible with narrow bandgap III-V infrared detectors. *Optics Express* **24**, 21512-21520 (2016).

[123] Y. Horie, A. Arbabi, E. Arbabi, S. M. Kamali, A. Faraon, Wide bandwidth and high resolution planar filter array based on DBR-metasurface-DBR structures. *Optics Express* **24**, 11677-11682 (2016).

[124] D. Fleischman, L. A. Sweatlock, H. Murakami, H. Atwater, Hyper-selective plasmonic color filters. *Optics Express* **25**, 27386-27395 (2017).

[125] S. Yokogawa, S. P. Burgos, H. A. Atwater, Plasmonic color filters for CMOS image sensor applications. *Nano Letters* **12**, 4349-4354 (2012).

[126] S. P. Burgos, S. Yokogawa, H. A. Atwater, Color imaging via nearest neighbor hole coupling in plasmonic color filters integrated onto a complementary metal-oxide semiconductor image sensor. *ACS Nano* **7**, 10038-10047 (2013).

[127] P. Gutruf, C. Zou, W. Withayachumnankul, M. Bhaskaran, S. Sriram, C. Fumeaux, Mechanically Tunable Dielectric Resonator Metasurfaces at Visible Frequencies. *ACS Nano* **10**, 133-141 (2016).

[128] J. Sautter, I. Staude, M. Decker, E. Rusak, D. N. Neshev, I. Brener, Y. S. Kivshar, Active Tuning of All-Dielectric Metasurfaces. *ACS Nano* **9**, 4308-4315 (2015).

[129] M. Rahmani, L. Xu, A. E. Miroshnichenko, A. Komar, R. Camacho-Morales, H. Chen, Y. Zárate, S. Kruk, G. Zhang, D. N. Neshev, Y. S. Kivshar, Reversible Thermal Tuning of All-Dielectric Metasurfaces. *Advanced Functional Materials* **27**, 1700580 (2017).

[130] M.-X. Ren, W. Wu, W. Cai, B. Pi, X.-Z. Zhang, J.-J. Xu, Reconfigurable metasurfaces that enable light polarization control by light. *Light: Science & Applications* **6**, e16254 (2017).

[131] T. Kan, A. Isozaki, N. Kanda, N. Nemoto, K. Konishi, M. Kuwata-Gonokami, K. Matsumoto, I. Shimoyama, Spiral metamaterial for active tuning of optical activity. *Applied Physics Letters* **102**, 221906 (2013).

[132] J. Guo, Y. Tu, L. Yang, Y. Zhang, L. Wang, B. Wang, Design and Simulation of Active Frequency-selective Metasurface for Full-colour Plasmonic Display. *Scientific Reports* **8**, 11778 (2018).

[133] Y. Yao, R. Shankar, M. A. Kats, Y. Song, J. Kong, M. Loncar, F. Capasso, Electrically Tunable Metasurface Perfect Absorbers for Ultrathin Mid-Infrared Optical Modulators. *Nano Letters* **14**, 6526-6532 (2014).

[134] J. Zhang, Y. Kosugi, A. Otomo, Y. Nakano, T. Tanemura, Active metasurface modulator with electro-optic polymer using bimodal plasmonic resonance. *Optics Express* **25**, 30304-30311 (2017).

[135] V. E. Babicheva, A. Boltasseva, A. V. Lavrinenko, Transparent conducting oxides for electro-optical plasmonic modulators. *Nanophotonics* **4**, (2015).

[136] X. Liu, J. H. Kang, H. Yuan, J. Park, S. J. Kim, Y. Cui, H. Y. Hwang, M. L. Brongersma, Electrical tuning of a quantum plasmonic resonance. *Nature Nanotechnology* **12**, 866-870 (2017).

[137] M. Abb, B. Sepulveda, H. M. H. Chong, O. L. Muskens, Transparent conducting oxides for active hybrid metamaterial devices. *Journal of Optics* **14**, 114007 (2012).

[138] K. F. Shi, R. R. Haque, B. Y. Zhao, R. C. Zhao, Z. L. Lu, Broadband electro-optical modulator based on transparent conducting oxide. *Optics Letters* **39**, 4978-4981 (2014).

[139] K. F. Shi, Z. L. Lu, Field-effect optical modulation based on epsilon-near-zero conductive oxide. *Optics Communications* **370**, 22-28 (2016).

[140] K. F. Shi, R. R. Haque, W. S. Zhao, R. C. Zhao, Z. L. Lu, Tunable plasmonic metamaterial based on transparent conducting oxide. *Physics and Simulation of Optoelectronic Devices xxii* **8980**, 898012 (2014).

[141] Z. Lu, K. Shi, P. Yin, Photonic MOS Based on "Optical Property Inversion". *MRS Advances* **1**, 1657-1669 (2016).

[142] Y. W. Huang, H. W. Lee, R. Sokhoyan, R. A. Pala, K. Thyagarajan, S. Han, D. P. Tsai, H. A. Atwater, Gate-Tunable Conducting Oxide Metasurfaces. *Nano Letters* **16**, 5319-5325 (2016).

[143] A. Forouzmand, H. Mosallaei, Real-time controllable and multifunctional metasurfaces utilizing indium tin oxide materials: A phased array perspective. *IEEE Transactions on Nanotechnology* **16**, 296-306 (2017).

[144] J. Park, J.-H. Kang, S. J. Kim, X. Liu, M. L. Brongersma, Dynamic Reflection Phase and Polarization Control in Metasurfaces. *Nano Letters* **17**, 407-413 (2016).

[145] F. Yi, E. Shim, A. Y. Zhu, H. Zhu, J. C. Reed, E. Cubukcu, Voltage tuning of plasmonic absorbers by indium tin oxide. *Applied Physics Letters* **102**, 221102 (2013).

[146] J. Park, J. H. Kang, X. Liu, M. L. Brongersma, Electrically Tunable Epsilon-Near-Zero (ENZ) Metafilm Absorbers. *Scientific Reports* **5**, 15754 (2015).

[147] K. Liu, C. R. Ye, S. Khan, V. J. Sorger, Review and perspective on ultrafast wavelength-size electro-optic modulators. *Laser & Photonics Reviews* **9**, 172-194 (2015).

[148] A. Anopchenko, L. Tao, C. Arndt, H. W. H. Lee, Field-effect tunable and broadband epsilon-near-zero perfect absorbers with deep subwavelength thickness. *ACS Photonics* **5**, 2631-2637 (2018).

[149] E. D. Palik, *Handbook of optical constants of solids*. (Academic press, 1998), vol. 3.

[150] H. W. Gao, W. Zhou, T. W. Odom, Plasmonic Crystals: A Platform to Catalog Resonances from Ultraviolet to Near-Infrared Wavelengths in a Plasmonic Library. *Advanced Functional Materials* **20**, 529-539 (2010).

[151] C.-H. Zhai, R.-J. Zhang, X. Chen, Y.-X. Zheng, S.-Y. Wang, J. Liu, N. Dai, L.-Y. Chen, Effects of Al doping on the properties of ZnO thin films deposited by atomic layer deposition. *Nanoscale Research Letters* **11**, 407 (2016).

[152] J. Yoon, M. Zhou, M. A. Badsha, T. Y. Kim, Y. C. Jun, C. K. Hwangbo, Broadband epsilon-near-zero perfect absorption in the near-infrared. *Scientific Reports* **5**, 12788 (2015).

[153] N. Kinsey, C. DeVault, J. Kim, M. Ferrera, V. Shalaev, A. Boltasseva, Epsilon-near-zero Al-doped ZnO for ultrafast switching at telecom wavelengths. *Optica* **2**, 616-622 (2015).

[154] S. Campione, J. R. Wendt, G. A. Keeler, T. S. Luk, Near-infrared strong coupling between metamaterials and epsilon-near-zero modes in degenerately doped semiconductor nanolayers. *ACS Photonics* **3**, 293-297 (2016).

[155] M. Z. Alam, S. A. Schulz, J. Upham, I. De Leon, R. W. Boyd, Large optical nonlinearity of nanoantennas coupled to an epsilon-near-zero material. *Nature Photonics* **12**, 79 (2018).

[156] G. Kafaie Shirmanesh, R. Sokhoyan, R. A. Pala, H. A. Atwater, Dual-gated active metasurface at 1550 nm with wide (>300°) phase tunability. *Nano Letters* **18**, 2957-2963 (2018).

[157] A. Capretti, Y. Wang, N. Engheta, L. Dal Negro, Comparative study of second-harmonic generation from epsilon-near-zero indium tin oxide and titanium nitride nanolayers excited in the near-infrared spectral range. *ACS Photonics* **2**, 1584-1591 (2015).

[158] L. Caspani, R. Kaipurath, M. Clerici, M. Ferrera, T. Roger, J. Kim, N. Kinsey, M. Pietrzyk, A. Di Falco, V. M. Shalaev, Enhanced nonlinear refractive index in ε-near-zero materials. *Physical Review Letters* **116**, 233901 (2016).

[159] E. G. Carnemolla, L. Caspani, C. DeVault, M. Clerici, S. Vezzoli, V. Bruno, V. M. Shalaev, D. Faccio, A. Boltasseva, M. Ferrera, Degenerate optical nonlinear enhancement in epsilon-near-zero transparent conducting oxides. *Optical Materials Express* **8**, 3392-3400 (2018).

[160] S. Gurung, A. Anopchenko, S. Bej, J. Joyner, J. D. Myers, J. Frantz, H. W. H. Lee, Atomic layer engineering of epsilon-near-zero ultrathin films with controllable field enhancement. *Advanced Materials Interfaces* **7**, 2000844 (2020).

[161] S. M. George, Atomic layer deposition: an overview. *Chemical Reviews* **110**, 111-131 (2009).

[162] N. P. Dasgupta, S. Neubert, W. Lee, O. Trejo, J.-R. Lee, F. B. Prinz, Atomic layer deposition of Al-doped ZnO films: effect of grain orientation on conductivity. *Chemistry of Materials* **22**, 4769-4775 (2010).

[163] E. L. Runnerstrom, K. P. Kelley, T. G. Folland, J. R. Nolen, N. Engheta, J. D. Caldwell, J.-P. Maria, Polaritonic hybrid-epsilon-near-zero modes: Beating the plasmonic confinement vs propagation-length trade-off with doped cadmium oxide bilayers. *Nano Letters* **19**, 948-957 (2019).

[164] R. Liu, C. M. Roberts, Y. Zhong, V. A. Podolskiy, D. Wasserman, Epsilon-near-zero photonics wires. *ACS Photonics* **3**, 1045-1052 (2016).

[165] N. M. Y. Zhang, K. Li, P. P. Shum, X. Yu, S. Zeng, Z. Wu, Q. J. Wang, K. T. Yong, L. Wei, Hybrid graphene/gold plasmonic fiber-optic biosensor. *Advanced Materials Technologies* **2**, 1600185 (2017).

[166] W. Zhou, D. J. Mandia, S. T. Barry, J. Albert, Absolute near-infrared refractometry with a calibrated tilted fiber Bragg grating. *Optics Letters* **40**, 1713-1716 (2015).

[167] M. Piliarik, J. Homola, Z. Manıková, J. Čtyroký, Surface plasmon resonance sensor based on a single-mode polarization-maintaining optical fiber. *Sensors and Actuators B: Chemical* **90**, 236-242 (2003).

[168] A. Sinibaldi, N. Danz, E. Descrovi, P. Munzert, U. Schulz, F. Sonntag, L. Dominici, F. Michelotti, Direct comparison of the performance of Bloch surface wave and surface plasmon polariton sensors. *Sensors and Actuators B: Chemical* **174**, 292-298 (2012).

[169] Y. Xu, P. Bai, X. Zhou, Y. Akimov, C. E. Png, L. K. Ang, W. Knoll, L. Wu, Optical refractive index sensors with plasmonic and photonic structures: promising and inconvenient truth. *Advanced Optical Materials* **7**, 1801433 (2019).

[170] S. Gurung, B. Subhajit, F. Tonelli, A. Anopchenko, Z. Yi, M. O. Scully, A. Marni, H. W. H. Lee, Higher-order optical Kerr effect in epsolon-near-zero conducting oxide thin films. *in preparation*, (2021).

[171] W. Hadibrata, H. Wei, S. Krishnaswamy, K. Aydin, Inverse design and 3D printing of a metalens on an optical fiber tip for direct laser lithography. *Nano Letters* **21**, 2422-2428 (2021).

[172] M. Plidschun, H. Ren, J. Kim, R. Förster, S. A. Maier, M. A. Schmidt, Ultrahigh numerical aperture meta-fibre for flexible optical trapping. *Light: Science & Applications* **10**, 1-11 (2021).

[173] M. Zeisberger, H. Schneidewind, U. Hübner, T. Wieduwilt, M. Plidschun, M. A. Schmidt, Plasmonic Metalens ‐ Enhanced Single ‐ Mode Fibers: A Pathway Toward Remote Light Focusing. *Advanced Photonics Research*, 2100100 (2021).